Distribution Agreement

In presenting this thesis or dissertation as a partial fulfillment of the requirements for an advanced degree from Emory University, I hereby grant to Emory University and its agents the non-exclusive license to archive, make accessible, and display my thesis or dissertation in whole or in part in all forms of media, now or hereafter known, including display on the world wide web. I understand that I may select some access restrictions as part of the online submission of this thesis or dissertation. I retain all ownership rights to the copyright of the thesis or dissertation. I also retain the right to use in future works (such as articles or books) all or part of this thesis or dissertation.

Signature:

_____ _____

Emrah Simsek Date

Single-cell-level Studies of Phenotypic Diversity in Bacteria

By

Emrah Simsek
Doctor of Philosophy

Physics

_____

Minsu Kim, Ph.D.
Advisor

_____

Connie Roth, Ph.D.
Committee Member

_____

Fereydoon Family, Ph. D.
Committee Member

_____

Ilya Nemenman, Ph. D.
Committee Member

_____

Philip Rather, Ph. D.
Committee Member

Accepted:

_____

Lisa A. Tedesco, Ph.D.
Dean of the James T. Laney School of Graduate Studies

_____

Date

Single-cell-level Studies of Phenotypic Diversity in Bacteria

By

Emrah Simsek
M.Sc., Istanbul Technical University, Turkey, 2012

Advisor: Minsu Kim, Ph.D.

An abstract of
A dissertation submitted to the Faculty of the
James T. Laney School of Graduate Studies of Emory University
in partial fulfillment of the requirements for the degree of
Doctor of Philosophy
in Physics
2019

Abstract

Single-cell-level Studies of Phenotypic Diversity in Bacteria
By Emrah Simsek

Bacteria have an amazing ability to adapt to unfavorable conditions, which is why they are all over the Earth. Population diversification is a well-known mechanism for adaptation. Importantly, an isogenic population can exhibit phenotypic diversity without changing their genotypes. My dissertation aims at elucidating the origins and implications of phenotypic diversity under three prevalent environmental conditions; nutrient fluctuations, antibiotic exposure, and restricted motility due to surface association.

We first characterized at the single-cell resolution the metabolic activities and growth kinetics of starved *Escherichia coli* cells subject to nutrient upshift. We observed a subpopulation of cells which resumed the growth long after the upshift. By characterizing their metabolic states, we showed that they exhibit active substrate uptake and catabolism but inactive anabolism. We showed that oxidative stress is an innate factor leading to these partial metabolic activities. We observed that cells with partial metabolic activities spontaneously restored their anabolism and grew. This growth resumption indicates that these cells were not dead but dormant.

We next quantified the temporal dynamics of the growth recovery of dormant cells in the face of bactericidal antibiotics. When a genetically-identical population faces a bactericidal antibiotic, a majority of cells dies quickly but a small fraction called persisters survives. Dormancy is the generally accepted mechanism for emergence of these persisters. When we characterized the time points at which these persister cells exit from dormancy, we found their temporal probability distribution exhibits a power-law decay. We explained this power-law decay by using heterogeneous Poisson processes. We showed how this explanation is consistent with a myriad of biomolecular pathways previously identified for entering and exiting dormancy.

Finally, we developed two visualization tools for studying the origins and implications of non-genetic population diversification in the context of surface associated-life of bacteria. These tools enabled characterization of surface-associated *Proteus mirabilis* bacteria at a wide range of scales from the single cell (μm) to the colony level (cm). Applying these tools to a few examples, we demonstrated how these tools could be useful.

Single-cell-level Studies of Phenotypic Diversity in Bacteria

By

Emrah Simsek
M.Sc., Istanbul Technical University, Turkey, 2012

Advisor: Minsu Kim, Ph.D.

A dissertation submitted to the Faculty of the
James T. Laney School of Graduate Studies of Emory University
in partial fulfillment of the requirements for the degree of
Doctor of Philosophy
in Physics
2019

Acknowledgements

I am grateful to my advisor Dr. Minsu Kim for his mentorship and support over the past five years. Owing to Dr. Kim' s mentoring, I feel that I have sharpened my research skills in many aspects. Dr. Kim never gave up on giving me excellent feedback for improving my skills on how to convey the most essential message in the most concise way possible. Dr. Kim' s mentoring provided me a structure along with some level of independence so that I could ponder over and even fail at times. I feel those failures have now made me a much stronger scientist.

I also thank Dr. Philip Rather, Dr. Fereydoon Family, Dr. Connie Roth, and Dr. Ilya Nemenman for serving on my committee and their priceless advice all along the way. I would like to acknowledge Dr. Nemenman for often providing mentorship in terms of my career development as well.

I thank all the current and former members of Minsu Kim Lab for all our interactions. They have played a significant role in my development as not only a scientist but also a human being. In particular, I thank Dr. Sukanya Iyer for providing me advice on multiple aspects of doing science including many molecular genetic techniques even long after she left.

Thanks to all staff members of Emory Department of Physics. I especially thank Barbara Conner for keeping me on track, Lowell Ramsey for tirelessly taking care of our incubators that kept my research running, and Jason Boss and Art Kleyman for keeping my computers running as well as for their friendship and smile.

I thank all the past and current members that I have interacted with at Emory Department of Physics for making me feel like home. I have been a part of an awesome, supportive, and open-minded community. I also thank the people of Atlanta who have shared even just a smile with me.

For Chapter 2, I am grateful to Dr. Ilya Nemenman and Dr. Hyun Youk for helpful discussions.

For Chapter 4, I am grateful to Dr. Philip Rather for introducing me the *P. mirabilis* swarming phenomenon, sharing strains, plasmids and reagents with me, patiently supervising me in learning all of the molecular cloning techniques I performed, and his priceless feedback. I thank Dr. Kristen Howery for teaching me molecular cloning techniques and participating in the early stages of our efforts for a strain construction (AMK79). I thank Matty Specht for his technical assistance under my supervision in the final steps of the construction of the AMK79 strain as a part of his training. Finally, I thank Daniel Uribe for collecting the data that yielded Fig. 4.1b under my supervision.

I thank my parents Fazilet and Emin Emre and my sister Bilgen for their love and support. I thank my sister and her husband Mustafa especially for providing our mom company during my absence for so many years; I could not have come this far without their generosity, endurance and support.

Last but not least, I thank my wife Arzu for her invaluable support and unconditional love. Thank you for standing by me no matter how hard the life could get. Thank you for tackling with me all the ups and downs of doing a Ph.D. abroad.

My work at Emory has been supported by Emory Start-up Funds and Research Corporation for Science Advancement (24097), both to Minsu Kim. Additionally, I am thankful to Laney Graduate School for all the financial and professional development support I have received during the course of my Ph.D. studies.

Table of Contents

Abbreviations

AcrAB: The multidrug efflux pump consisting of proteins AcrA and AcrB

Amp^r: Ampicillin resistance gene

ART: Antiretroviral therapy

aTc: Anhydrotetracycline hydrochloride (A derivative of tetracycline with no antibiotic activity. It is used for controlling tetracycline-dependent gene expression)

bp: Base pair

C: Carbon

CFU: Colony forming unit

cm: Centimeter

DNA: Deoxyribonucleic acid (The self-replicating carrier of genetic information)

***E. coli*:** *Escherichia coli* (A bacterial species name)

FITC: Fluorescein isothiocyanate

***flhDC* operon:** The unit of transcriptionally-coupled genes encoding DNA-binding transcriptional dual regulator proteins FlhD and FlhC

GASP: Growth advantageous in stationary phase

***gfp*:** The gene encoding green fluorescent protein

GFP: Green fluorescent protein

GFP-ON: Positive for green fluorescent protein signals

GFP-OFF: Negative for green fluorescent protein signals

Gt: Giga ($x10^9$) tons

h: Hour

HIV: Human immunodeficiency virus

H_2O_2: Hydrogen peroxide

ISME: International Society for Microbial Ecology

Km^r: Kanamycin resistance gene

LB: Luria-Bertani (A nutrient rich microbial growth medium)

MCS: Multiple cloning site

min: Minute

ml: Milliliter

mm: Millimeter

mM: Millimolar

MSD: Mean square displacement

ng: Nanogram

N/A: Not available

N-C-: An acronym used for indicating the lack of nitrogen and carbon

N_2: Nitrogen

OxyR: Oxidative stress regulator

OD_{600}: Optical density measured at 600 nanometers of wavelength

pCon: A continuously active promoter

PCR: Polymerase chain reaction

PI: Propidium iodide

PI+: Positive for propidium iodide staining

pTet: Tetracycline regulated promoter

***P. mirabilis*:** *Proteus mirabilis* (A bacterial species name)

***P_{tet}*:** Tetracycline regulated promoter

RNA: Ribonucleic acid

rpm: Revolution(s) per minute

s: Second

***sod*A:** The gene encoding superoxide dismutase A protein

***sod*B:** The gene encoding superoxide dismutase B protein

TetR: Tetracycline promoter' s repressor protein

***tet*R:** Tetracycline promoter' s repressor protein encoding gene

TRITC: Tetramethylrhodamine

UTR: Untranslated region

WT: Wild type

X-Gal: 5-bromo-4-chloro-3-indolyl-β-D-galactopyranoside

μg: Microgram

μl: Microliter

μm: Micrometer

μM: Micromolar

Δ: The Greek letter indicating the deletion of a gene in molecular genetics nomenclature

2NBDG: 2-N-7-nitrobenz-2-oxa-1,3-diazol-4-yl amino-2-deoxyglucose (A fluorescently-labeled derivative of glucose)

List of Figures

List of Tables

Chapter 1: Introduction

1.1. Motivation.

The ability to adapt to unfavorable conditions is essential to survival of all living organisms. Bacterial populations have adapted to virtually every niche on Earth from soil and sea to the surfaces deep under the ocean, and from the gut of animals to the extremely cold Arctic and hot water springs near volcanos, making them the second largest taxon (after plants) in terms of biomass on Earth; a ~13 % of the total biomass on Earth is bacteria (~70 Gt C bacteria and ~550 Gt C total biomass) [1]. Many of these niches are thought to have unfavorable features such as limited or fluctuating nutrient levels [2] and antibiotic agents [3, 4]. In order to escape from antibiotic agents or move toward nutrients, bacteria can utilize a form of motility known as chemotaxis [5-7]. However, in natural ecosystems, planktonic bacteria are often substantially outnumbered by their surface-associated counterparts [7-9]. Mainly due to restricted hydration, surface attachment is expected to impede bacterial motility on surfaces like soil [10-12] and hydrogels [13]. This may exacerbate the challenge imposed by growth inhibitory factors when motility is the only option to escape from them. Notwithstanding, the ubiquity and abundancy of bacteria on Earth indicate that bacteria can overcome this challenge. This makes bacterial populations an attractive model system for studying how populations adapt to unfavorable environmental conditions.

Bacteria are thought to have significant environmental roles such as nutrient cycling [14]. Although the free-living form is dominant [15], many bacterial species adopt a symbiotic life with other multicellular organisms, such as bacteria in human body performing indispensable functions

in the human gut [16]. Indeed, a human body contains nearly as many bacterial cells as its own human cells [17]. The recently postulated hologenome concept considers every such multicellular host and the microbes it harbors as a single and unique biological entity in the light of the accumulating evidence that symbiotic microbes contribute to the physiology, behavior, origin and evolution of species [18]. On the other hand, some bacteria may also pose risks for human health causing chronic infections [19] which may in certain cases even lead to cancer development [20]. Collectively, a better understanding of how bacterial populations adapt to and survive unfavorable conditions is a necessity.

Population diversification is a widespread phenomenon that allows bacterial populations to adapt to unfavorable environments [21, 22]; with diversity, there will likely be some individuals that are well suited for a given environment. Such population diversifications have also been demonstrated in laboratory environments where different subpopulations specialize on different tasks rendering a more efficient utilization of the resources available in the environment [23-28]. Additionally, in order to cope with environmental challenges such as nutrient scarcity, antibiotic agents, and restricted mobility due to surface association, diversification of bacterial populations through changing their genetic composition has been well documented [29-46].

One important mechanism of population diversification is phenotypic heterogeneity, i.e., an isogenic population of bacteria can exhibit very different phenotypes [25, 47-50]. This phenotypic heterogeneity can have significant effects on ecological dynamics of populations and species [51]. For example, non-genetic phenotypic diversification plays a critical role in population survival through catastrophic environmental changes [52, 53] and promotes sustenance of microbial species

[54, 55]. In clonal populations, phenotypic heterogeneity can be exogenously triggered due to heterogeneities in the microenvironments of their constituent cells [56-59]. On the other hand, a generic endogenous source of non-genetic phenotypic heterogeneity is the inherent stochasticity of a bacterial cell as a system of biochemical reactions. The molecules participating in key regulatory reactions inside of a cell are usually present in low (< 100) copy numbers [60] which can cause large fluctuations in the reaction rates [61]. A result of this and possible additional factors such as the chromosomal position of a gene [62] is the phenotypic variation in gene expression [63-66]. Such phenotypic variation can allow clonal cells to exhibit different responses to the same environmental stimulus [67]. This can increase the net fitness of a population in fluctuating environments [68]. When complemented by an appropriate genetic wiring (i.e., effectively a positive feedback) the stochasticity in gene expression can yield multiple stable phenotypes within a genetically-identical population [69-71]. In some cases, cellular stochasticity also allows cells to abruptly switch between alternative phenotypes [72, 73], and this can serve as a survival strategy in fluctuating environments [74]. Random partitioning of cellular components at cell division is another well-recognized stochastic mechanism for the emergence of cell-to-cell variation [75-77], which was also shown to contribute to cell survival under fluctuating environments [78]. In summary, the noisy nature of the way a bacterial cell operates intrinsically yields chances for the emergence of a non-genetic population diversification even in constant and uniform environments, and the diversity generated in this way can allow survival of a population in the case of an environmental shift.

Quantitative analyses of non-genetic phenotypic heterogeneity are highly important because they can reveal dynamic features of the mechanisms that generates the heterogeneity and enable *a priori*

prediction of dynamics of a population as it adapts to unfavorable environmental conditions. This can also help elucidating microbial survival strategies. Although non-genetic phenotypic heterogeneity as an adaptation mechanism has been suspected since long time ago, its direct characterization has only become possible by the advances in single-cell-level microscopy and fluorescent reporters for cellular events and cell physiology in the last nearly two decades [79, 80]. Hence, our quantitative understanding about the temporal dynamics of non-genetic population diversification near unfavorable environments is limited. Likewise, little is known about the underlying cellular and environmental factors and implications of non-genetic population diversification in bacterial populations. Therefore, this dissertation focuses on a quantitative characterization of phenotypic heterogeneity and its implications as genetically identical bacterial populations adapt to three prevalent environmental challenges; nutrient fluctuations, transient antibiotic exposure, and surface-associated growth. We identify and discuss key environmental and cellular factors underlying the observed phenotypic variations.

1.2. Methodology.

In this dissertation, origins of phenotypic diversity and its implications on the adaptation dynamics of bacterial populations to unfavorable environments are quantitatively studied. This extensively involved optical microscopy, image analysis and mathematical modeling as well as both modern and conventional microbiology and molecular genetics techniques. Since the scope of this dissertation and the work it entails are highly interdisciplinary, in this section a brief introduction to the most essential techniques is provided for the general reader.

1.2.1. The plate count method.

The most commonly employed conventional technique for probing bacterial population dynamics is called the "plate count method" or the "colony forming unit (CFU) assay" (Fig. 1. 1). This method relies on growing single cells into visible colonies. It was originally devised by Robert Koch more than a century ago for isolating single clones of bacteria [81] and has been widely used in microbial research and public health sectors since then [82-85].

In this method, a fixed volume of cells from a culture growing in a medium of interest is collected and spread on a nutrient rich semi-solid (agar) medium in a Petri dish. Importantly, the cells are spread after appropriate dilutions so that single bacteria would be sparsely distributed on the surface of the semi-solid medium. Then, the dish is incubated overnight with the idea is that each live cell seeded on the plate will grow into a visible colony. The next day, the number of visible colonies on the plate is counted. Technically, these colonies are called colony forming units, CFUs. Finally, the number of CFUs per unit volume is determined. In order to obtain the dynamics of the bacterial population, this procedure is repeated at various time points, and the resultant number of CFUs per unit volume is plotted as a function of time.

In this method the intrinsic assumption is that life equals reproductive ability; every live cell in the culture will grow into a visible colony when incubated on the nutrient rich semi-solid medium. In order to study the bacterial population dynamics in the presence of a certain unfavorable environmental feature such as antibiotics, in this method the unfavorable feature is included in only the cell culture and not in the nutrient rich semi-solid medium. Resultantly, a plot of CFU/ml

versus time reports on the survival kinetics of the bacterial population in the presence of that particular type of unfavorable environmental feature.

The plate count method is of very high throughput as it requires the investment of only about 30 min of time per each time point enquired, and the next day hundreds of colonies can be counted within several minutes. However, it has fundamental limitations for studying phenotypic heterogeneity within populations. First of all, this method does not allow visualization of either the dynamics within colonies or the physiological states of single cells. More importantly, while it is true that every cell that grows into a visible colony must be alive, the reciprocal of this is not necessarily true: not every non-colony-forming cell is dead. Indeed, it has been known for long that bacterial cells can lie dormant for extended periods of time without growing and then exit from dormancy and grow at future times [86].

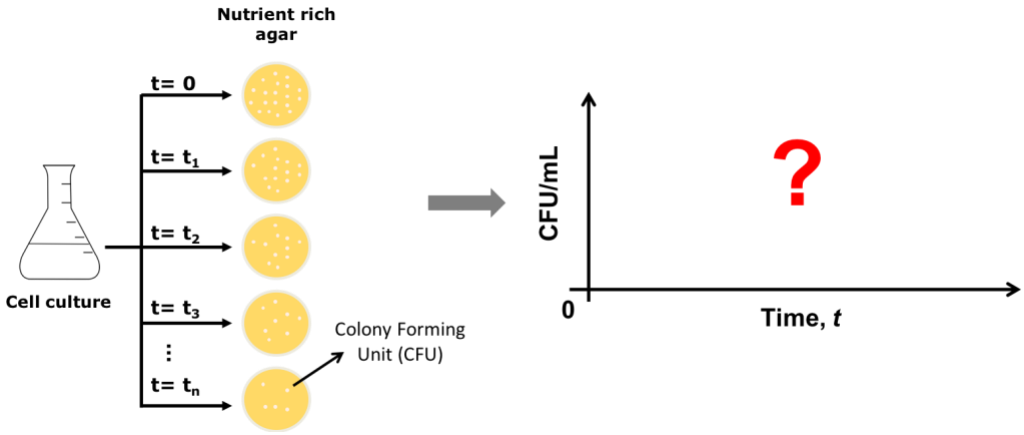

Figure 1. 1. A schematic illustration of the plate count method.

A fixed volume of cells from a culture growing in the medium of interest is collected and spread on a nutrient rich agar plate after appropriate dilutions so that single bacteria would be sparsely distributed on the plate. Then, the plate is incubated overnight with the idea is that each live cell seeded on the plate will grow into a visible colony. The next day the number of visible colonies on the plate is counted. Technically, these colonies are called colony forming units, CFUs). Finally, the number of CFUs per unit volume is determined. In order to obtain the dynamics of the bacterial population, this procedure is repeated at various time points, and the resultant number of CFUs per unit volume is plotted as a function of time. Not drawn to scale.

1.2.2. Optical microscopy and fluorescent reporters for studying living single cells.

Bacterial cells are of the sizes on the order of a micrometer. Hence, employment of optical microscopy is generally sufficient for single-cell-level investigation of bacteria unless some intricate sub-cellular features are studied in particular.

Bright field microscopy is the simplest version of light microscopy where differential transmission of light through an object compared to its surrounding medium is used in order to visualize it. However, all bacterial growth media are water-based, and bacterial cells have nearly the same density as water [87]. This requires often a deadly staining of bacterial cells in order to be visualized by bright field microscopy.

On the other hand, bacterial cells have refractive indices that are significantly greater than that of water [88]. Hence, phase contrast microscopy, which visualizes an object basically by just relying on the difference in the refractive indices of the object versus its surrounding medium [89], can be used for imaging single live bacterial cells without the requirement of any staining. Phase contrast microscopy uses a whitish light source; hence it is not expected to significantly influence the physiology of bacterial cells.

For a basic single-cell-level investigation with phase contrast microscopy, a small aliquot from a bacterial culture is sandwiched between two cover glasses and then imaged. In order to image the same living single bacteria for long periods of time (hours to days), a variant of this method is employed where one of the cover glasses is replaced with a semi-solid (agar or agarose gel) pad. As a result, single bacteria are physically confined and can be visualized with a phase contrast

microscope through the cover glass (Fig. 1. 2). For an even longer term of observation or when the medium surrounding the cells need to be constantly replenished, more sophisticated devices called microfluidic chips can be employed [80].

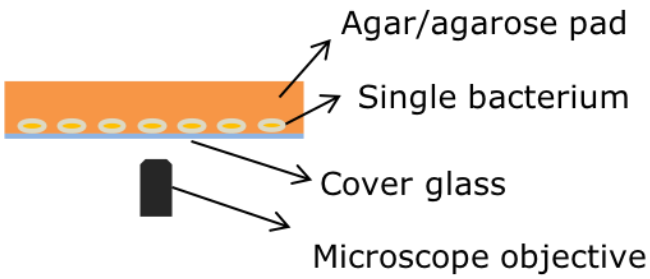

Figure 1. 2. A schematic illustration of a basic method for live cell imaging.

An aliquot from a culture of bacteria is sandwiched between a cover glass and a semi-solid (agar or agarose gel) pad. Single bacteria are then visualized through the cover glass using phase contrast microscopy. Not drawn to scale.

Often this method is combined with fluorescence microscopy for the use of certain fluorescent reporters for assaying cellular processes such as respiration [90], substrate uptake [91], and gene expression [92], etc. A fluorescent reporter molecule of interest gets excited by light at a certain range of wavelengths, and responds in turn by emitting light at wavelengths in a range shifted towards the red. A fluorescence microscope is equipped with an appropriate light source and a filter set in order to achieve a specific excitation of the fluorescent molecule of interest and collect the spectrum of light it emits in turn. Typically, the fluorescence signal detected is linearly proportional to the concentration of the fluorescent molecules within a specimen [93].

Cells are primarily made of proteins, and proteins dominantly control the processes inside the cells [94]. Genes are designated DNA units that carry the genetic code for all the proteins that a cell is

capable of synthesizing. A typical bacterial cell contains more than a thousand genes which means being capable of synthesizing a roughly equal numbers of proteins [94]. However, a cell does not need those proteins all at the same time. Hence, they have mechanisms to control when and to what extent a gene will be expressed. Timing and magnitude of the expression of genes are primarily controlled by a designated DNA sequence in their upstream called promoter. According to the central dogma of protein synthesis, the enzyme called RNA polymerase binds to the promoter and then transcribes the information pertaining the gene into an intermediary structure called the messenger RNA. The messenger RNA is then translated into proteins by the virtue of an enzyme complex called ribosome. This process is called "gene expression".

Most bacteria can be genetically manipulated for fusing a gene encoding a fluorescent protein (such as a green fluorescent protein gene) next to a gene of interest such that the expression of the gene will be coupled to the expression of the fluorescent protein [95]. This coupling can be at the mRNA transcription level as well as the translation (protein production) level depending on the details of the genetic manipulation employed [95]. It is important to note that such fluorescent protein gene fusions need to be carefully tailored based on the specific purpose. In the least sophisticated cases, increasing intracellular fluorescent protein signals will reflect an active transcription state for the expression of the gene of interest. By employing externally controllable synthetic promoters, a similar design can also be utilized for testing the ability of cells to synthesize proteins independently of any inherent control over the promoter activities [96]. With the multiplicity of the fluorescent proteins with distinct excitation/emission spectra [97], the expression of more than one genes simultaneously can be visualized in live cells. However, the limitation of employing fluorescence microscopy in live cell imaging is that often the light used to

excite the fluorophore of choice excites some sub-cellular components as well. This in turn may cause a significant alteration of cell physiology [80]. A cell's physiological state is in general tightly linked to how fast it grows. Therefore, at a minimum, one needs to confirm that the growth rate of cells does not significantly change when fluorescence microscopy is involved. Generally, minimizing the power of excitation light, light exposure time, and frequency of imaging are sufficient solutions.

Once phase contrast and fluorescence images of the samples are obtained, the images are processed for identification of the cells, and then the intracellular fluorescence intensities are measured. Although specific circumstances may require an *ad hoc* customization of the image analysis, there are several freely-available software, such as the Image J developed by the National Institute of Health of the U.S. [98], for a generic identification and analysis of bacterial cells in microscopy images. Image analyses processes can often be at least semi- automatized.

1.2.3. Mathematically representing cellular processes using ordinary differential equations.

The physiological processes inside a living cell are indeed biochemical reactions. The most biochemical reactions are categorized into one of the three elementary types of reactions called a zeroth, first, or a second order chemical reaction (See Fig. 1. 3 for a graphic illustration).

In a zeroth order reaction, a chemical of interest (C) emerges from nothing at a constant rate defined as k_0. In this case, the time scale of the emergence of C is set by $1/k_0$. This means that, when a zeroth order reaction is assumed, over the timescales on the order of $1/k_0$ the cell of interest has no control over the intracellular production of C. Zeroth order reactions are typically used for

modeling a constant influx of a chemical from outside to the inside of a cell or the synthesis of *C* from another chemical whose concentration does not change much over time scales on the order of $1/k_0$.

In a first order reaction, another chemical (*B*) is converted to the chemical *C* at a constant rate k_1. A first order reaction is typically used for modeling the degradation or efflux of a chemical. Lastly, in a second order reaction two chemicals, say *A* and *D*, come together at a rate constant k_2 and jointly get converted to the chemical *C*.

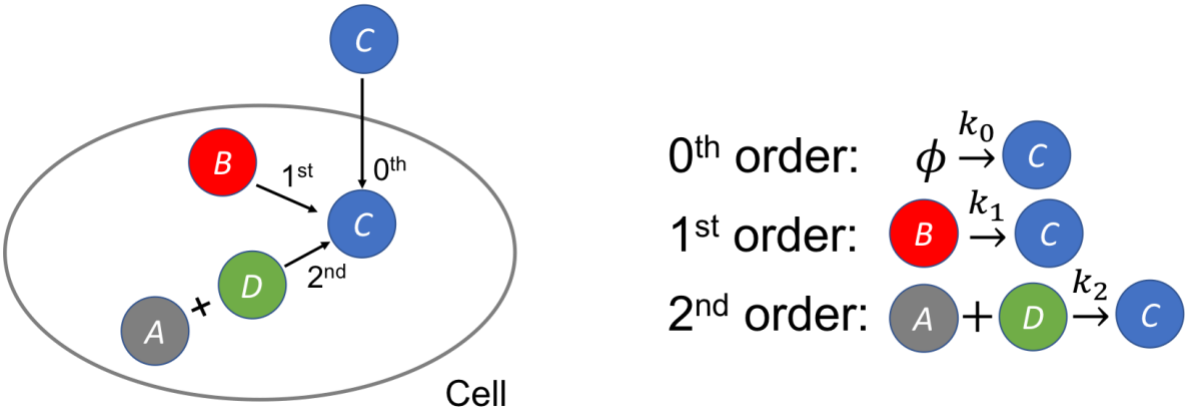

Figure 1. 3. A graphic illustration of the most typical types of biochemical reactions inside of a cell.

The physiological processes inside a living cell are indeed biochemical reactions. The most biochemical reactions can be modeled as a zeroth, first, or a second order chemical reaction occurring at a constant rate. Illustrated here is the production of a chemical *C* via its influx at a rate k_0, by the conversion of another chemical *B* at a rate k_1, and by the joint conversion of two other chemicals *A* and *D* at a rate k_2. Not drawn to scale.

The bottom line in all these types of reactions is the conversion of mass from one chemical form to another per unit time in a given volume, and this is defined by the *law of mass action*, whose foundations rely on the original work by two late Norwegian chemists Cato M. Guldberg and Peter

Waage and a Dutch physical chemist Jacobus Henricus van 't Hoff in the mid- to late 1800s. According to the law of mass action, for the examples given above, per unit time, in the zeroth order reaction the concentration of *C* increases by k_0. For the first order reaction, per unit time, the concentration of *C* increases by k_1 times the concentration of *B*, while the concentration of *B* decreases by the same amount. Finally, in the second order reaction, per unit time, the concentration of *C* increases by k_2 times the concentration of *A* times the concentration of *D*, while the concentration of both *A* and *D* decreases by the same amount. As exemplified below, these changes are mathematically defined in terms of a set of coupled ordinary differential equations where brackets ([]) are used to denote the concentration of the chemicals.

$$\frac{d[C]}{dt} = k_0 + k_1[B] + k_2[A][D]$$

$$\frac{d[B]}{dt} = -k_1[B]$$

$$\frac{d[A]}{dt} = -k_2[A][D]$$

$$\frac{d[D]}{dt} = -k_2[A][D]$$

For the reasons described earlier in this chapter, inside of a cell chemical processes are inherently stochastic mainly due to thermal fluctuations. Hence, the changes in the concentration of a chemical for a single cell may deviate from the prediction based on the law of mass action. Notwithstanding, an averaging over a large population of cells (typically, more than 100 cells) yields results highly comparable with those predicted by the law of mass action [99].

Lastly, in order to consolidate our understanding with regards to this subsection, let us consider a model situation where the production of a fluorescent protein *P* is externally induced by addition of a substance that can specifically activate the (synthetic) promoter that controls the expression of the gene encoding *P*. Here, the concentration of the protein and its associated messenger RNA are denoted by [*P*] and [*R*], respectively. We assume that the copy number of the gene encoding the fluorescent protein *P* does not change over the timescales for which we model how [*P*] and [*R*] change. Therefore, the elementary reactions governing the production of this protein are listed as below.

$$\phi \xrightarrow{\alpha_R} R$$

$$R \xrightarrow{\alpha_P} P$$

$$R \xrightarrow{\beta_R} \phi$$

$$P \xrightarrow{\beta_P} \phi$$

Here, α_R and α_P are the rate constants for production of *R* and *P*, respectively. β_R and β_P are the first order rate constants that overall represent biochemical events such as degradation and dilution by cell growth that negatively affect [*R*] and [*P*] levels, respectively. Hence, the set of coupled ordinary differential equations below describes how the average [*P*] and [*R*] change over time following the induction.

$$\frac{d[R]}{dt} = \alpha_R - \beta_R[R]$$

$$\frac{d[P]}{dt} = \alpha_P[R] - \beta_P[P]$$

For example, under the conditions where $\beta_R = \beta_p \approx 0$ this set of equations predicts $[R] \propto t$ and $[P] \propto t^2$. Remembering that the concentration of a fluorescent protein is generally proportional to the intensity of fluorescence it emits [93], single-cell-level measurements of fluorescent protein levels can easily be achieved and compared with the prediction of models such as the one given as the example one considered here.

1.3. Outline of Dissertation.

This dissertation is comprised of five chapters in total. This first chapter is dedicated for a motivation of the research, a brief introduction to the research methodology employed for the general reader, and an outline of the dissertation.

In the second chapter, we focused on nutrient fluctuations. We quantified the phenotypic composition of an isogenic population of starved *Escherichia coli* cells subject to nutrient upshift. Specifically, using optical microscopy and fluorescent reporters we characterized the metabolic activities (i.e., substrate uptake, catabolism, and anabolism) and growth responses of single cells during the nutrient upshift. Our results revealed a dynamically changing heterogeneity in the growth response of the population and indicated metabolic heterogeneity as a cellular variation driving such dynamic changes. Through genetic and chemical manipulations, we identified oxidative stress as an innate factor triggering the cellular variations observed in metabolic activities.

The third chapter highlights a clinically important example of non-genetic phenotypic heterogeneity in bacterial populations called persisters, which confers a clonal population a chance

for evading antibiotic treatments. Previous studies have found that persisters survive antibiotic treatment by virtue of not growing during long periods of time (i.e., lag phase) under favorable conditions [100-104]. Here, using phase contrast microscopy we quantitatively analyzed the lag phase of an *E. coli* population at the single cell level. Our analyses suggested some dynamic features for the stochastic mechanisms that may yield persistence and enabled *a priori* prediction of population dynamics via a simple mathematical framework. Specifically, the distribution of the duration of lag phase (i.e., lag time) was well captured by an exponential decay for the majority of (i.e., normal) cells suggesting that the lag phase of normal cells is a Poisson process governed by a single rate constant kinetics. The lag time distribution of the remaining minor fraction (i.e., persisters) exhibited a long tail captured by a power-law decay with an exponent of nearly two. Using a simple quantitative argument, we demonstrated that this power-law decay can be explained by a wide variation of the rate constant for the Poisson process. This notion agrees well with the multiplicity of biomolecular pathways that have been identified for achieving persistence through dormancy. Developing a mathematical model based on the empirically obtained biphasic lag time distribution, we were able to quantitatively predict complex population dynamics under exposure to a widely used bactericidal antibiotic (ampicillin) without invoking any *ad hoc* parameters.

In the fourth chapter, we developed tools that allow studying the origins and implications of non-genetic population diversification across multiple spatial and time scales in surface associated-bacterial populations using *Proteus mirabilis* bacterium as a model organism. As an isogenic population of *P. mirabilis* bacteria colonizes an agar surface, it adopts a strategy of periodic cycles between range expansions and cell growth/multiplication at the colony edge. Before each round of

range expansions, a striking example of non-genetic population diversification is observed; the cells in the outermost region of a colony make a decision whether to remain normal (immotile) and exploit the available territory or differentiate and activate a flagella-dependent-motility program known as "swarming" for exploring new territories. Here, we constructed a transcriptional fluorescent reporter gene fusion to the master regulator of motility in bacteria (*flhDC* operon) and demonstrated how this strain can be used to study the spatiotemporal pattern of the population diversification within a growing cell population. This can help identifying key cellular and environmental factors and their functional roles in swarming. Furthermore, we developed a Petri dish-based device compatible with dry-objective-optical microscopy. We demonstrated how this device can be used in order to visualize and link dynamic properties of swarming across a broad range of scales from the single-cell (μm/s) to the colony level (cm/h).

Finally, the fifth chapter of this dissertation discusses our novel findings presented in the chapters from two to four and their contributions to the understanding of origins and implications of non-genetic phenotypic diversification as a way to adapt to unfavorable environments. Furthermore, a discussion of the broader implications of our findings is provided, and some relevant future research is recommended.

Chapter 2: The emergence of metabolic heterogeneity and diverse growth responses in isogenic bacterial cells

Emrah Şimşek[1] and Minsu Kim[1,2]

[1]Department of Physics, Emory University, Atlanta, GA, 30322. U.S.A.

[2]Graduate Division of Biological and Biomedical Sciences, Emory University, Atlanta, GA, 30322. U.S.A.

Published in:

The ISME Journal (2018) 12: 1199-1209

https://doi.org/10.1038/s41396-017-0036-2

2.1. Abstract.

Microorganisms adapt to frequent environmental changes through population diversification. Previous studies demonstrated phenotypic diversity in a clonal population and its important effects on microbial ecology. However, the dynamic changes of phenotypic composition have rarely been characterized. Also, cellular variations and environmental factors responsible for phenotypic diversity remain poorly understood. Here, we studied phenotypic diversity driven by metabolic heterogeneity. We characterized metabolic activities and growth kinetics of starved *Escherichia coli* cells subject to nutrient upshift at single-cell resolution. We observed three subpopulations with distinct metabolic activities and mapped them to three different growth phenotypes. One

subpopulation was metabolically active and immediately grew upon nutrient upshift. One subpopulation was metabolically inactive and non-viable. The other subpopulation was metabolically partially active and did not grow upon nutrient upshift. The ratio of these subpopulations changed dynamically during starvation. A long-term observation of cells with partial metabolic activities indicated that their metabolism was later spontaneously restored, leading to growth recovery. Further investigations showed that oxidative stress can induce the emergence of a subpopulation with partial metabolic activities. Our findings reveal the emergence of metabolic heterogeneity and associated dynamic changes in phenotypic composition. In addition, the results shed new light on microbial dormancy, which has important implications in microbial ecology and biomedicine.

2.2. Introduction.

Microorganisms occupy virtually every niche on earth, most of which is scarce in nutrients. The lifestyle of microorganisms can be well characterized by long periods of nutrient deprivation intercepted by short periods of nutrient excess [2]. Population diversification is an important mechanism for populations to adapt to fluctuating environments [21, 22]; with diversity, there will likely be some individuals that are well suited for a given environment. Previous studies characterized how genetic composition in a population changes slowly through mutations and becomes diverse in environments where nutrients are limited and fluctuate [29-36]. In recent years, it became clear that a genetically-identical population can also diversify phenotypically [25, 40, 48, 69, 104-111]. Phenotypic diversity can have significant effects on ecological dynamics of populations and species [51]; for example, it plays a critical role in population survival through catastrophic environmental changes [52], promoting sustenance of microbial species [54, 55].

Because phenotypic diversity does not involve genetic mutation, it is expected to arise on short timescales, leading to dynamic changes in phenotypic composition in a population. However, these temporal dynamics have rarely been quantified. Furthermore, cellular variations responsible for phenotypic diversity and environmental factors triggering such cellular variations have not been well characterized.

Metabolism is a central process by which cells derive components essential for basic cellular functions. Cell-to-cell variation in metabolism, if it exists, could result in phenotypic diversity. Recent studies of stochastic gene expression are supportive of the intriguing possibility of metabolic heterogeneity. For example, studies found that genetically-identical cells in the same environment may produce different amounts of metabolically-relevant proteins [23, 112-114]. Recent computational work suggested that such different protein expression could give rise to metabolic heterogeneity in *E. coli* cells [115]. A network model based on stochastic expression of *lac* enzymes in *E. coli* cells showed how stochastic gene expression could affect carbon metabolism [116]. Similarly, the direct measurements of metabolites in carbon metabolism revealed the coupling between metabolite pools and gene expression [117, 118]. Furthermore, a recent experimental study showed isogenic *Klebsiella oxytoca* cells might exhibit different N_2 fixation rates, meaning different metabolic activities [119].

In this study, by examining starved *E. coli* cells subject to nutrient upshift, we characterized the emergence of metabolic heterogeneity and its effect on phenotypic composition in a population. Metabolism can be largely divided into three processes: i) bringing extracellular substrates into the cytoplasm (substrate uptake), ii) breaking down the substrates into smaller units (catabolism), and

iii) constructing macromolecules from the small units (anabolism). By visualizing accumulation/depletion of fluorescently-labeled substrates and production of fluorescent proteins in individual cells, we characterized these three metabolic processes at single-cell resolution. The results revealed that there exists significant cell-to-cell heterogeneity in these processes, and that this heterogeneity leads to diverse growth phenotypes, including dormancy. Also, we found that oxidative stress can induce metabolic heterogeneity and diverse growth phenotypes.

2.3. Results.

2.3.1. Cell-to-cell heterogeneity in metabolic activities and growth phenotypes.

In nature, microorganisms are often starved of carbon [2]. Numerous studies have reported that when environmental microbial samples were plated on agar plates containing rich nutrients (e.g., LB), many cells did not form colonies [120, 121]. Known as 'the great plate count anomaly', this observation is a long-standing enigma in microbial ecology, largely because cellular states (e.g., metabolic states) of those cells that failed to form colonies are unclear and under intense debate [122-124]. When we performed a similar plating assay using carbon-starved cultures under well-controlled laboratory conditions, we made the same observation. We grew *E. coli* cells in minimal medium with glucose and ammonium as the sole carbon and nitrogen sources and suspended them in medium without glucose (starvation medium) at the OD_{600} of ~0.4; upon suspension, cell growth stopped immediately (Fig. 2. 1).

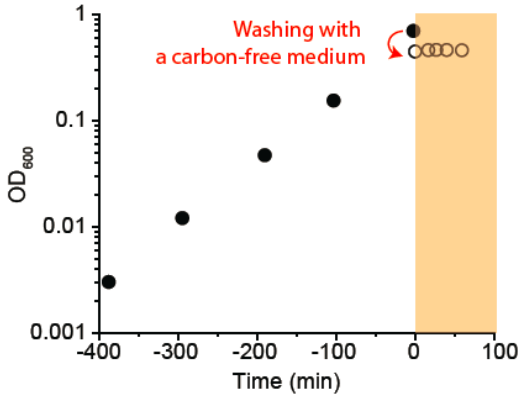

Figure 2. 1. Growth curve before and after the onset of starvation.

E. coli cells were grown to mid-exponential phase in N-C- minimal medium [125] supplemented with 20 mM of glucose (the sole carbon source) and 20 mM of ammonium chloride (the sole nitrogen source). At time zero, cells were spun down and re-suspended in the same minimal medium without glucose, i.e., the onset of starvation. Cell growth stopped immediately (orange region). Here, we showed an exemplary growth curve from one experiment. We observed such abrupt cessation of growth in all our experiments.

At different times during carbon starvation, we took a 100 μl aliquot of the culture, diluted it (by 10^3 - 10^6-fold) and plated it on LB agar plates; this exposure to LB represents nutrient upshift. Please see Methods for details and Fig. 2. 2 for a graphic illustration of our experimental procedure.

As quantified in Fig. 2. 3A, the number of colony-forming units decreased over time. This decrease indicates that with longer starvation, fewer cells resumed growth upon nutrient upshift.

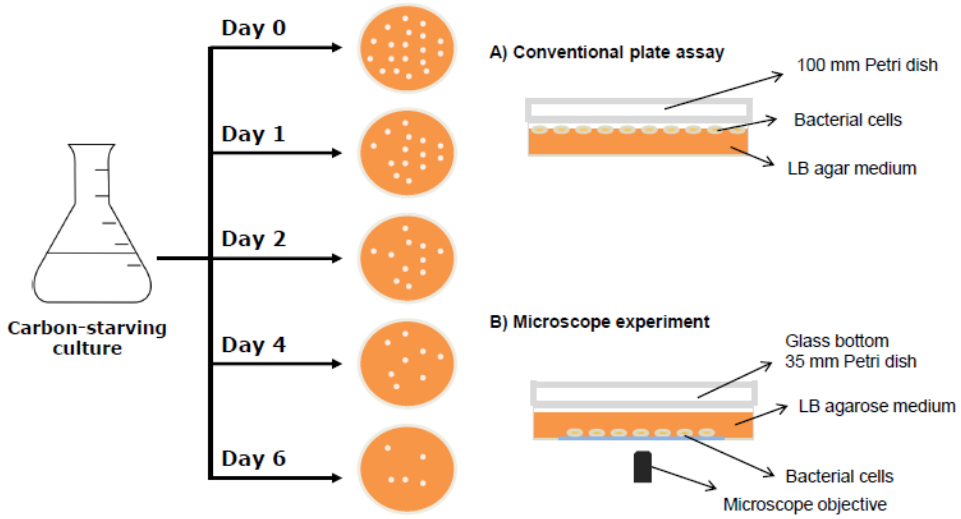

Figure 2. 2. A graphic representation of our experimental procedure.

This illustration shows the procedure of our experiment. For biological repeats, this procedure was repeated independently (using independent cultures). *E. coli* cells were starved of glucose. A fixed volume of the starved culture was taken at various time during starvation. **(A)** For a conventional plate assay, the sample was spread on LB agar plates; see Methods for details. We had two or three technical replicates, which always gave very similar results. We also performed biological repeats at least twice for all experiments. **(B)** For a single-cell-level observation, cells were spread under a LB agarose pad, and observed using a microscope. See Methods for details. We performed initial tests to estimate technical variations by measuring the number of metabolically-active cells and 2NBDG signals in them. We found technical variations to be small. For example, the variations in the number of metabolically-active cells from four or five technical replicates were within 2%. Variations in 2NBDG signals from four or five technical replicates were within 5%. Thus, we no longer performed technical repeats. We did perform at least two biological repeats for all our experiments. Please note that single-cell-level measurements are low-throughput and labor-intensive. Our "one" experiment includes multiple measurements for different durations of starvation. Therefore, performing technical repeats in addition to biological repeats is prohibitively time-consuming. Also, see a quote from a recent article regarding replicate measurements, "Typically, biological variability is substantially greater than technical variability, so it is to our advantage to commit resources to sampling biologically relevant variables unless measures of technical variability are themselves of interest" [126].

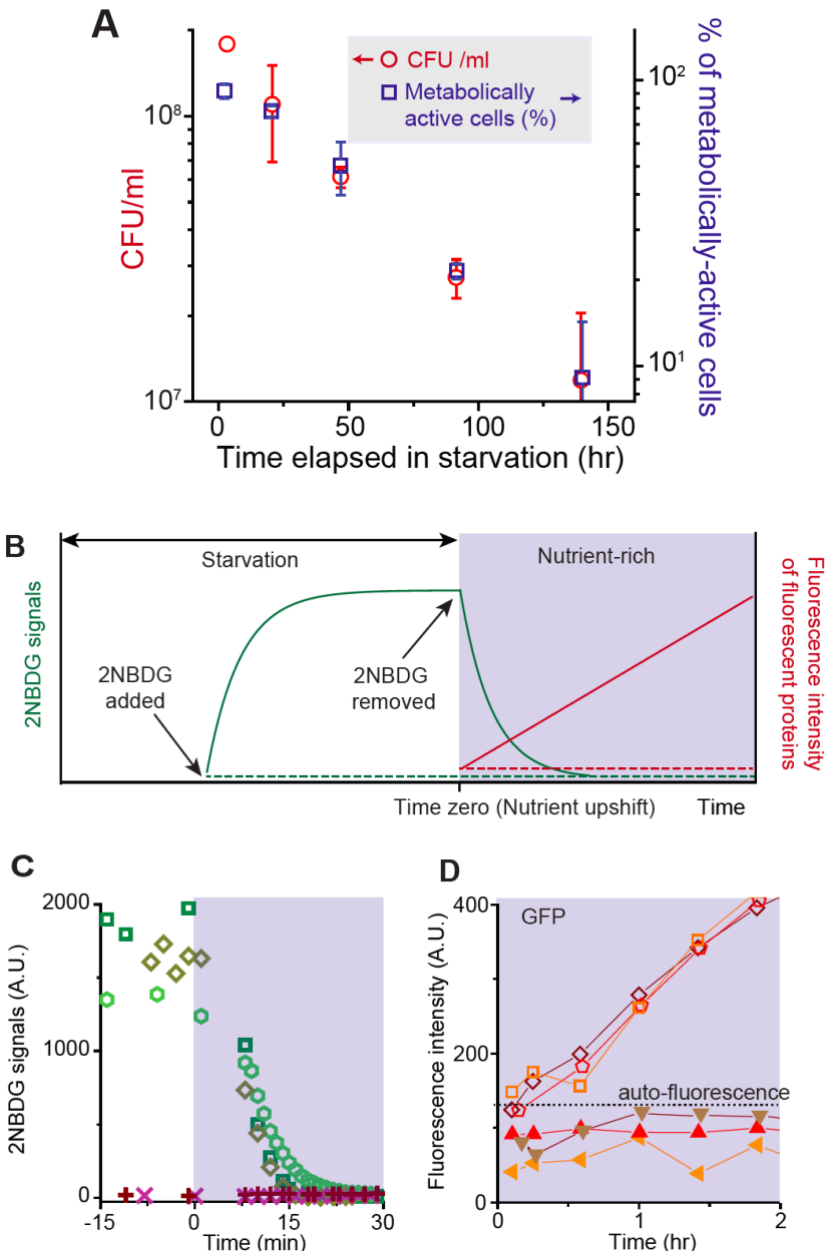

Figure 2. 3. Metabolic activities and growth of cells upon nutrient upshift.

(A) We performed a conventional plate assay. *E. coli* cells were deprived of carbon (glucose) at time zero. At various time points during starvation, a fixed volume of the starved culture was taken, diluted appropriately, and spread on LB agar plates; see Methods for details. The number of colonies was counted after 24 hours of incubation, and colony forming unit (CFU) per ml was then determined. CFU/ml decreased over time (red circles, left axis). We also plotted the percentage of metabolically-active cells in a population (blue squares, right axis); a detailed description of the metabolically-active cells is provided below, in the caption to (C, D). Note that the scales of the left and right axes have the same fold change. CFU/ml and the percentage of metabolically-active cells decreased similarly over time. The error bars indicate one standard

deviation, which was obtained from at least two biological replicates. **(B)** We determined 1) the substrate uptake activity by intracellular accumulation of fluorescently-labeled substrates, 2NBDG, 2) the catabolic activity by intracellular depletion of 2NBDG upon inhibition of its transport, and 3) the anabolic activity by *de novo* synthesis of green fluorescent proteins (GFP) or red fluorescent proteins (mCherry). When 2NBDG is available externally, metabolically-active cells would transport them, exhibiting strong intracellular 2NBDG signals (solid green curve in the white region). Active catabolism rapidly decomposes 2NBDG molecules into non-fluorescent metabolites [127, 128]. Therefore, intracellular 2NBDG concentration is determined by both transport and catabolic activities, as described by Eq. 1-3. When 2NBDG is removed from a culture, because 2NBDG uptake into cells would stop, intracellular 2NBDG signals are expected to decrease in metabolically-active cells (solid green curve in the shaded region); see Eq. 4. Also, these metabolically-active cells are expected to express fluorescent proteins, GFP or mCherry, when the expression is induced (solid red line). Conversely, metabolically-inactive cells are expected to exhibit neither 2NBDG uptake (dashed green line) nor production of fluorescent proteins (dashed red line). **(C, D)** We experimentally tested these expected patterns. We starved *E. coli* cells of carbon (glucose) for 2.3 hours and subjected them to nutrient upshift; see text or Methods for details. We then monitored ~2500 cells in four biological repeats. We observed subpopulations with different metabolic activities. 91.7 % (± 5.9 %, one standard deviation from four biological replicates) of cells exhibited the pattern of active metabolism. These cells exhibited strong 2NBDG signals before nutrient upshift, but the signals decreased rapidly upon the shift (Movie). Typical changes in 2NBDG signals were plotted in Fig. 2. 3C (open symbols). In all of these cells, GFP intensity increased, indicating *de novo* protein synthesis; see Fig. 2. 3D (open symbols) for typical changes in GFP intensity. GFP intensity typically reached its saturation levels 3-4 hours after nutrient upshift. We repeated this analysis by starving a culture for different periods of time and monitoring ~1500 cells in two independent experiments (i.e., biological repeats). We counted metabolically-active cells and plotted their percentage in panel A (blue squares). We also observed cells that exhibited the patterns of inactive metabolism: neither 2NBDG uptake (crosses in Fig. 2. 3C) nor production of fluorescent proteins (solid symbols in Fig. 2. 3D). The details of these metabolically-inactive cells were described in Fig. 2. 8. See Table 2.1 for the number of cells with different metabolic activities.

Time (h)	**Metabolically active**	**Metabolically partially active**	**PI+**	**Lysed**	**Moribund[a]**	**Unidentified[b]**	**Total**
2.3	1423	3	33	88	18	3	1568[c]
20.3	988	9	83	143	45	5	1273
47	713	53	184	413	48	10	1421
91.6	305	38	185	860	28	18	1483
140	103	13	118	959	17	6	1216

Table 2. 1. The number of cells in each subpopulation.

[a] Initially, these cells were metabolically active and exhibited clear boundaries. But soon after nutrient upshift, their boundaries became diffuse, meaning that they were lysed. We put such cells in the "Moribund" category.

[b] These were a very low number of cells (or objects) with odd morphologies, and we were not sure if they were *E. coli* cells or debris. We put such cells in the "Unidentified" category.

[c] For 2.3 hours starvation, we conducted two different sets of experiments. In one set, we tested our approach to measure metabolic activities (discussed in the early part of the Results section). In the other set, we utilized this approach to characterize population composition.

We sought to examine how metabolic activities of cells that grew were different from those that failed to grow. To measure metabolic activities of individual cells, we adopted the following approach, which was based on recent developments in single-cell-level fluorescence imaging [79, 80]. First, we determined which cells have positive substrate uptake activity by monitoring the accumulation of fluorescently-labeled substrates in the cytoplasm. Glucose is the preferred carbon source for many microbes, including *E. coli*. When glucose molecules become available extracellularly, starved cells with positive substrate uptake activity will transport and accumulate them in the cytoplasm. This accumulation can be visualized using the fluorescently-labeled glucose molecules, 2-N-7-nitrobenz-2-oxa-1,3-diazol-4-yl amino-2-deoxyglucose (2NBDG), which would result in strong fluorescence signals inside cells [91, 127-130]; see the solid green curve in the white region in Fig. 2. 3B. Below, we discuss the expected functional form of this accumulation.

Previous studies indicated that glucose analog 2NBDG is transported and degraded by glucose transporters and glycolytic enzymes, respectively [91, 127-130]. We denote the transport and intracellular degradation rates by α and β, respectively, and the intracellular 2NBDG concentration by N. Then, a change in N is given by

$$\frac{dN}{dt} = \alpha - \beta \cdot N . \qquad \text{(Eq. 1)}$$

The solution is

$$N = \frac{\alpha}{\beta} \cdot \left[1 - \exp(-\beta \cdot t)\right]. \qquad \text{(Eq. 2)}$$

At the steady state ($dN/dt = 0$), N is determined by the dynamic balance between transport and degradation,

$$N_s = \frac{\alpha}{\beta}, \qquad \text{(Eq. 3)}$$

where N_s is the steady state intracellular 2NBDG concentration.

When we incubated starved cells with 10 μM of 2NBDG for various durations, we were able to detect intracellular 2NBDG signals already with ~5 min incubation (Fig. 2. 4A); therefore, in our experiments below, to ensure the reliable detection of signals, we pre-incubated cells with 2NBDG for ~25 min (see Fig. 2. 4 caption for details). Conversely, cells with no transport activity are expected to exhibit no 2NBDG signals (Fig. 2. 3B, dashed green line in the white region).

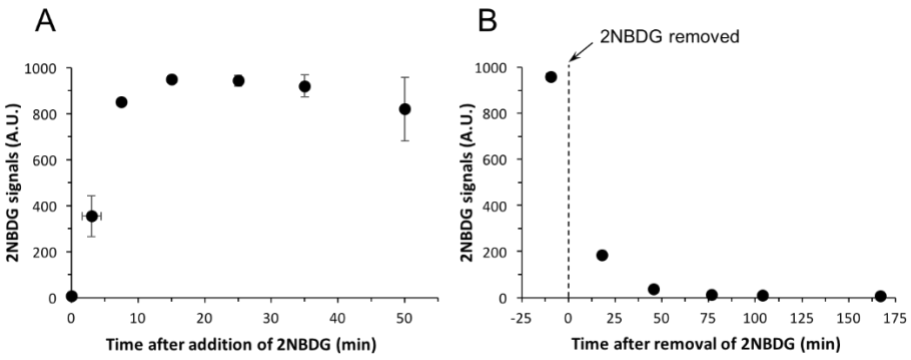

Figure 2. 4. 2NBDG transport and degradation.

(A) Previous studies indicated that the glucose analog 2NBDG is transported and degraded by glucose transporters and glycolytic enzymes, respectively [91, 127-130]. To experimentally demonstrate 2NBDG transport by starved cells, we suspended cells in starvation medium (minimal medium containing no glucose; see Methods) for ~2.3 hours and added 2NBDG to the medium at a final concentration of 10 μM. We then collected samples at various times and imaged them using a fluorescence microscope. For each time point, we analyzed and averaged intracellular 2NBDG signals of ~250 cells (we excluded cells with diffuse boundaries and cells stained by PI in the analysis; see the text and Fig. 2. 8 for the details of these cells). The temporal dynamics of intracellular 2NBDG signals are plotted in panel A (the addition of 2NBDG defined the time zero). The signals increase immediately after 2NBDG addition, indicating 2NBDG transport. The signals remain nearly constant after 15 min. (In the main text, to identify cells with active 2NBDG uptake, we pre-incubated cells with 2NBDG for 25 min. 25 min were chosen as the incubation time based on our data that the signals remain nearly constant after 15 min).

This immediate increase in the intracellular 2NBDG signal suggests the prior induction of glucose transporters. In our experiments, we initially cultured cells with glucose as the sole carbon source and abruptly starved cells of glucose. Growth on glucose leads to induction of glucose transporters [131], and glucose starvation results in further up-regulation of glucose transporters [132]. For example, Mlc (DgsA), a global regulator repressing the expression of glucose transporters is down-regulated during starvation, leading to up-regulation of transporters (e.g., see an increase in the amounts of Crr, glucose-specific phosphotransferase enzyme IIA component). Therefore, the production of glucose transporters during the prior growth on glucose and further upregulation of the production during glucose starvation can account for the immediate uptake of 2NBDG by starved cells.

On a related note, we determined intracellular 2NBDG accumulation after induction of transporters because we wanted to measure *the metabolic ability* of glucose transport. If cells have low expression of glucose transporters, even if they are metabolically capable of transport, 2NBDG may not accumulate in cells to detectable levels. We did not want our measurement of the metabolic ability to be limited by low expression of transporters, which was why we adopted the experimental procedure that leads to full induction of glucose transporters (as described in the paragraph above).

Whether intracellular 2NBDG represents carbohydrate storage is an interesting point. However, glycogen is the storage form of glucose (and carbohydrate in general) and is shown to accumulate only when growth is limited in the presence of an excess carbon source [133]. In our experimental condition, cells were starved of carbon. We added 2NBDG to the carbon-starved culture, but the concentration used (10 μM) was too low to support growth (Fig. 2. 5), meaning that cells still experienced severe carbon limitation. Therefore, it is unlikely that intracellular 2NBDG molecules get converted to glycogen as carbohydrate storage.

(B) Previous studies have observed the steady maintenance of 2NBDG signals at a constant level in cells and attributed it to the dynamic equilibrium between transport and degradation [127, 128]. In the text, we mathematically described how the dynamic equilibrium leads to the steady maintenance of 2NBDG signals. The panel A showed that the intracellular 2NBDG signal reached its steady state after 15 min, being maintained at a constant level afterwards. This steady maintenance suggests active 2NBDG degradation in glucose-starved cells. Note that starved cells do not grow (Fig. 2. 1): hence, no dilution of 2NBDG by cell growth. To experimentally demonstrate 2NBDG degradation in starved cells, we spun these cells down and re-suspended them in starvation medium containing no 2NBDG. We then collected samples at various times and imaged them using a fluorescence microscope. For each time point, we analyzed and averaged intracellular 2NBDG signals of ~300 cells (we again excluded cells with diffuse boundaries and cells stained by PI in the analysis). The signals decreased over time, supporting 2NBDG degradation; see panel B (the re-suspension defines time zero). The data points and error bars in these plots (panels A and B) represent the mean and one standard deviation from two biological replicates.

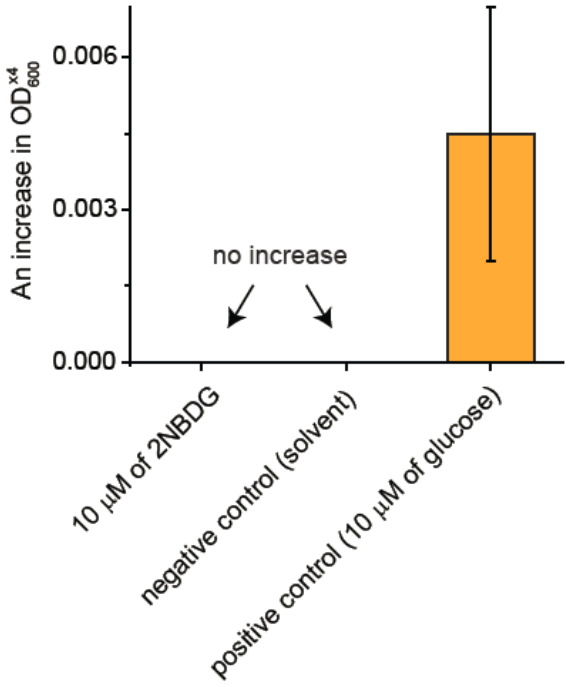

Figure 2. 5. 2NBDG does not support growth.

We suspended cells in glucose-free minimal medium (starvation medium), as described in the Methods. We added 10 μM of 2NBDG to the culture (10 μM is the concentration used in our experiments). As a positive control, we added 10 μM of glucose. As a negative control, we added neither 2NBDG nor glucose. We then measured cell growth by measuring after one hour; refers to OD_{600} measured using a sample holder with an optical path length four times longer than that of a typical holder (18B-SOG-40, Starna Cells Inc). We observed no increase in the negative control and also with 2NBDG, but a significant increase with glucose. Thus, 2NBDG does not support cell growth. We performed two biological repeats and the error bar represents one standard deviation from the biological repeats.

Active catabolism leads to the intracellular break-down of transported substrates into smaller units. Hence, we determined which cells are catabolically active by monitoring decomposition of 2NBDG molecules. Previous molecular-level studies have shown that after 2NBDG molecules are transported into bacterial cells, active catabolism rapidly decomposes these 2NBDG molecules into non-fluorescent metabolites [129], while inactivation of catabolism abolishes decomposition [130]. When 2NBDG molecules are present in the environment, the intracellular 2NBDG

concentration will depend on both transport and catabolic activities; this dependence is described by Eq. (1-3) in and further discussed in Fig. 2. 4.

Consider that after the steady state of intracellular 2NBDG concentration was established, 2NBDG molecules were abruptly removed from the environment. Then, 2NBDG transport would stop; $\alpha = 0$. With active degradation, the intracellular 2NBDG concentration would decrease. Eq. 1, together with $\alpha = 0$, predicts an exponential decrease in 2NBDG concentration,

$$N = N_s \cdot \exp(-\beta \cdot t) . \quad \text{(Eq. 4)}$$

Here, we are particularly interested in knowing whether starved cells could readily catabolize nutrients when these nutrients became available. Thus, if we incubate starved cells with 2NBDG for 25 min (which would result in strong intracellular 2NBDG signals as observed in Fig. 2. 4) and suspend them in 2NBDG-free nutrient-rich medium, active catabolism would lead to a rapid decrease in intracellular 2NBDG signals (Fig. 2. 3B, solid green curve in the shaded region).

Next, we determined protein anabolism by characterizing *de novo* synthesis of fluorescent proteins. We employed a strain in which the expression of green fluorescent protein (GFP) or red fluorescent proteins (mCherry) was driven by a synthetic promoter P_{tet} (the repressor of P_{tet}, TetR, is constitutively expressed in this strain) [96]. An inducer of the P_{tet} promoter, aTc, diffuses into cells rapidly [134], activating protein expression. Cells with active anabolism would synthesize fluorescent proteins, leading to an increase in fluorescence intensity (Fig. 2. 3B, solid red line in the shaded region). With inactive anabolism, fluorescence intensity would not increase (Fig. 2. 3B, dashed red line). We note that there exists a study that characterized protein anabolism during starvation using a similar approach [135]. Conversely, we are interested in anabolism in cells after

nutrients become available. Thus, our study focuses on protein anabolism after nutrient upshift (post-starvation).

Next, we show experimental data confirming these predicted patterns for metabolically active or inactive cells. Following the procedure described above, we starved cells of glucose for 2.3 hours (at OD_{600} of 0.4), spread ~5 µl aliquot on LB agarose plates (i.e., nutrient upshift), and monitored ~2500 cells using time-lapse microscopy in four independent experiments. 91.7 (± 5.9) % of cells showed the predicted pattern of active metabolism. First, when 2NBDG molecules became available extracellularly during starvation, these cells accumulated them intracellularly, exhibiting strong 2NBDG signals; compare the solid green curve in Fig. 2. 3B and Fig. 2. 4A. When we subjected the starved cells to nutrient upshift (i.e., LB medium containing no 2NBDG), their 2NBDG signals decreased rapidly and became undetectable within 20 min (Supplementary Movie). In Fig. 2. 3C, we quantified 2NBDG signals for a few cells (open symbols), which again showed strong signals before and an immediate decrease after nutrient upshift: ~100-fold decrease in 30 min. This rapid decrease cannot be accounted for by dilution due to cell growth; even for cells that are actively growing in LB medium (whose doubling time is ~20 min), the dilution would lead to a nearly three-fold decrease over 30 min. Rather, the rapid decrease in 2NBDG signals indicates active 2NBDG degradation. This decrease in 2NBDG signals upon nutrient upshift agreed with the predicted pattern; compare Fig. 2. 3C (open symbols) and Fig. 2. 3B (solid green curve in the shaded region), indicating active substrate uptake and catabolism. The re-plot of 2NBDG signals in a semi-log scale indicates that this decrease is exponential (Fig. 2. 6), as predicted by Eq. 4.

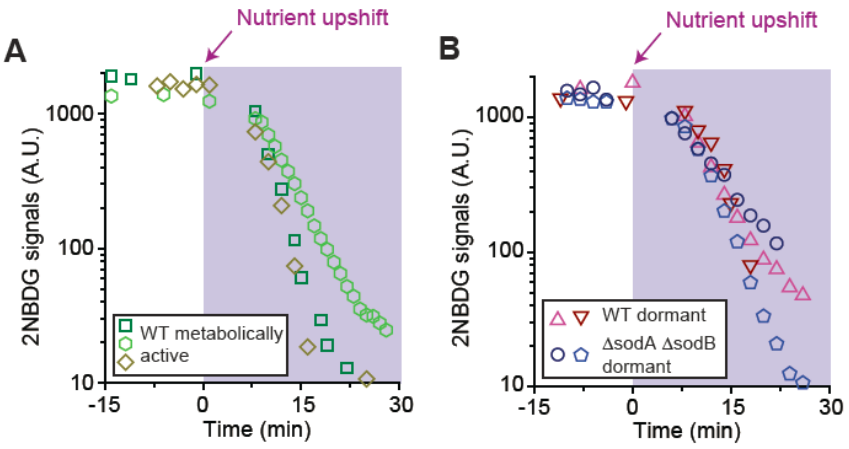

Figure 2. 6. Upon nutrient upshift, 2NBDG signals decay exponentially.

Eq. 4 predicts that after nutrient upshift, 2NBDG levels decrease exponentially. To test this prediction, we re-plotted data from Fig. 2. 3C (panel A) and Fig. 2. 10A (panel B) in a semi-log graph. A linear decrease in 2NBDG signals after nutrient upshift (shaded region) in these semi-log plots indicates an exponential decay.

Furthermore, the activation of protein production (using aTc as described above) led to an increase in fluorescence intensity (open symbols in Fig. 2. 3D), agreeing with the predicted pattern from active anabolism (solid red line in the shaded region in Fig. 2. 3B). All of these metabolically-active cells recovered their growth within 100 min after nutrient upshift (see Fig. 2. 3 for the distribution of growth recovery time), indicating that active metabolism is associated with active cell growth.

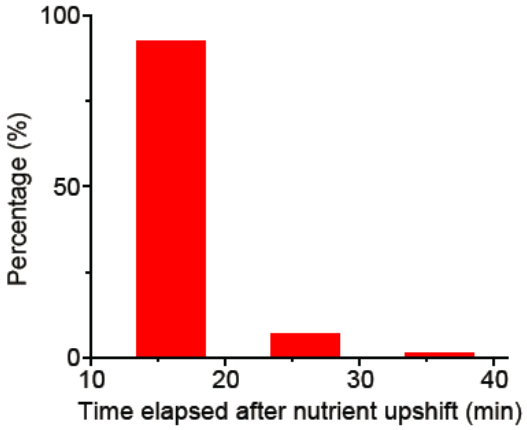

Figure 2. 7. Lag time distribution of metabolically-active cells.

In the main text, we described our experiments for cells starved for 2.3 hours; briefly, we subjected them to nutrient upshift, characterized their metabolic activities, and observed cells with active metabolism. We determined the time points at which these metabolically-active cells resumed growth (~1000 cells were analyzed) and plotted the lag time distribution here. They all initiated their growth within 40 min after nutrient upshift. Their growth was slow initially but accelerated over time, growing at fast rates after 100 min. We made a similar observation in two biological replicates.

We also observed cells showing the predicted patterns of metabolic inactivity. These cells exhibited neither 2NBDG uptake (compare dashed green line in Fig. 2. 3B and crosses in Fig. 2. 3C) nor production of fluorescent proteins (compare dashed red line in Fig. 2. 3B and solid symbols in Fig. 2. 3D). None of these cells resumed growth after nutrient upshift. These cells either had diffuse cell boundaries (i.e., loss of refractivity) or were stained by propidium iodide (PI), which are signs of the loss of viability. These cells were described in greater details in Fig. 2. 8.

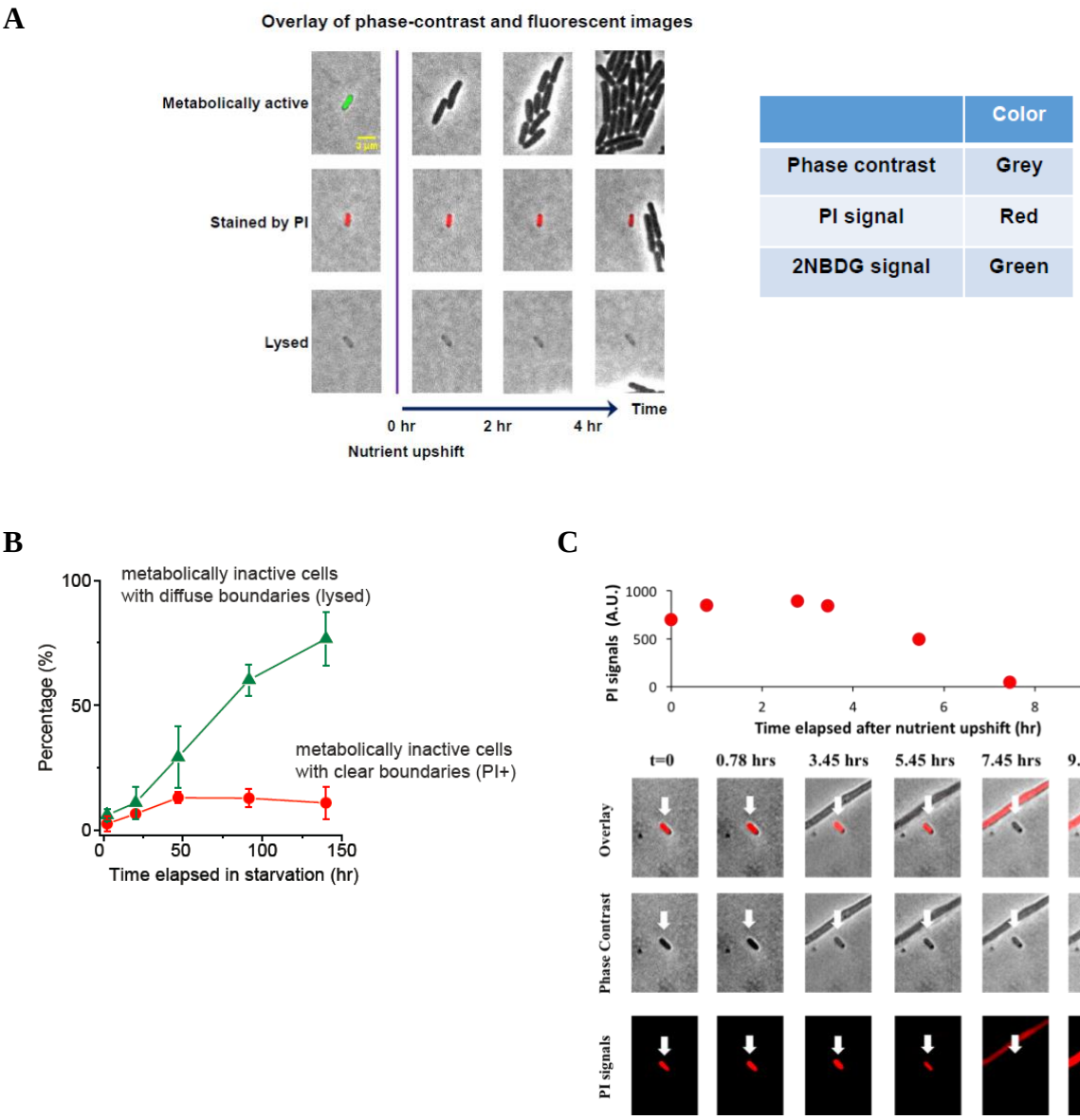

Figure 2. 8. Detailed description of metabolically-inactive cells.

In the main text, we described metabolically-active cells in a 2.3-hour-starved culture. Here, we focused our description on metabolically-inactive cells. For *E. coli*, propidium iodide (PI) was shown to be an excellent indicator of viability [136-139]; PI stains nucleic acids in non-viable cells [140-142]. We found that 2.6% of cells was stained by PI (PI+) (middle row in panel A). They showed neither 2NBDG uptake nor production of fluorescent proteins (thus, metabolically inactive). A long-term observation (~ three days) of these cells after nutrient upshift using a microscope revealed that none of these cells resumed growth. The percentage of these cells increased with longer starvation, peaking at ~13 % in the culture starved for 47 hours and then remaining nearly constant afterwards (see red circles in panel B); the error bars indicate one standard deviation from at least two biological replicates. Normally, when observed with phase-contrast microscopy, an *E. coli* cell is refractile (i.e., it exhibits a dark area with a sharp boundary); e.g., see metabolically-active cells in the upper row in panel A. Lysis results in the loss of refractivity; lysed cells

exhibit poor phase-contrast with a diffuse boundary (see the bottom row in panel A). The loss of refractivity indicates the loss of cytoplasmic contents. These cells were not stained by PI; given that PI stains DNA and RNA [140-142], the lack of staining indicates the loss of DNA and RNA. Also, they exhibited neither 2NBDG uptake nor production of fluorescent proteins (thus, metabolically-inactive). A long-term observation (~ three days) of these lysed cells after nutrient upshift confirmed that none of them resumed growth. We found 6.0% of cells in a population were lysed cells in a 2.3-hour-starved culture. Their percentage increased with longer starvation periods (panel B, green triangles); the error bars indicate one standard deviation from at least two biological replicates.

In some experiments, by accident, we observed the lysis of PI+ cells that resulted in the loss of PI signals. For example, in one experiment with a three-day-starved culture, we observed 48 cells exhibiting strong PI signals at the beginning. During an eight-hour-long observation, 22 of them lost refractivity and subsequently lost intracellular PI signals (please note that this observation is not related to major findings of this work, and therefore we believe that obtaining exact statistics is not necessary). The image sequence in panel C visualizes this process for a representative cell; for further clarification, we included a temporal plot of PI signals. Considering that PI stains nucleic acids [140-142], this observation indicates that DNA and RNA get lost during cell lysis. Our observation above was made using cells starved for 2.3 h. When we starved cells for different durations and counted the number of metabolically-active cells, we found that their percentage decreased monotonically (blue squares in Fig. 2. 3A). Interestingly, this decrease was very similar to the decrease in the number of colony-forming units obtained from conventional plate assays above (compare red circles and blue squares in Fig. 2. 3A), further supporting that active metabolism is a good indicator for a growth phenotype. The percentage of metabolically-inactive non-viable cells was plotted in Fig. 2. 8B, which showed a monotonic increase with longer starvation periods.

2.3.2. Emergence of dormant cells with partial metabolic activities.

In cultures starved longer, we observed the emergence of a subpopulation with a unique metabolic state. Cells in this subpopulation showed high 2NBDG intensity before nutrient upshift and a rapid

decrease in intensity after upshift (open triangles in Fig. 2. 10A), exhibiting the predicted pattern of active substrate uptake and catabolism. However, they did not produce fluorescent proteins. Thus, metabolically, they were partially active. Above, we described that metabolically-active cells resumed growth within 100 min after nutrient upshift. In contrast, these partially active cells did not resume growth in this time window; see Fig. 2. 9 for an exemplary image sequence. They exhibited clear cell boundaries and were not stained by PI, suggesting that they were viable. Their percentage was initially very low and peaked after nearly two days of starvation (Fig. 2. 10B).

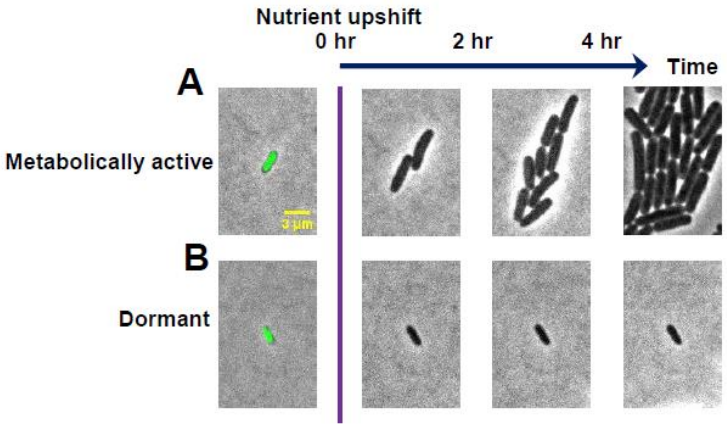

Figure 2. 9. An exemplary image sequence of a dormant cell.

In the main text, we described our observation of metabolically-partially-active, dormant cells. Here, we showed an exemplary image sequence of such a cell from a two-day-starved culture. As a comparison, we also showed a metabolically-active cell that resumed growth immediately after nutrient upshift. The image color code is the same as in Fig. 2. 8.

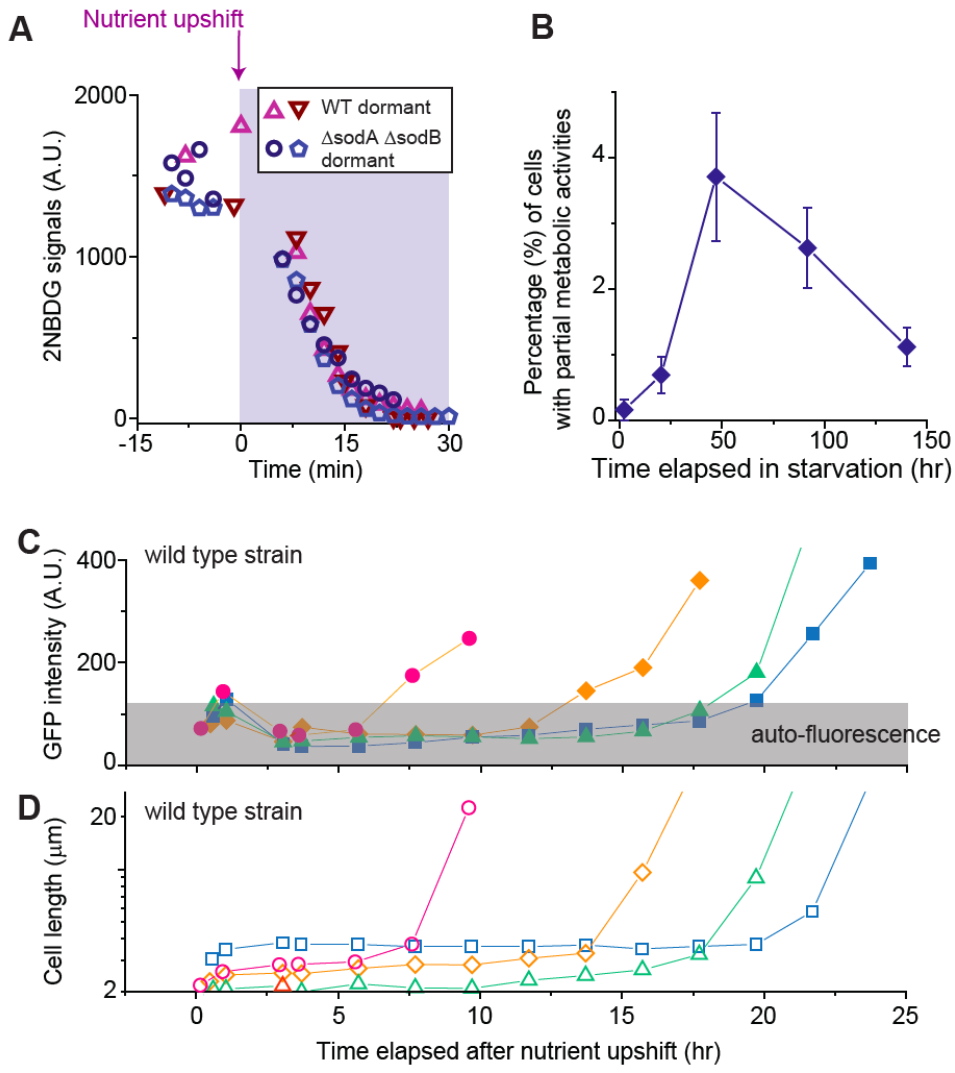

Figure 2. 10. Characterization of metabolically-partially-active, dormant cells

(A, B) We starved cells of glucose for different periods of time and monitored ~1500 cells in two biological replicates. We observed dormant cells exhibiting partial metabolic activities; see text for detail. The number of these cells varied depending on the duration of starvation and was always lower than 5% of a population (Fig. 2. 10B; the error bars indicate one standard deviation from two biological replicates). In all of these cells, 2NBDG signals decreased immediately upon nutrient upshift. In Fig. 2. 10A, we plotted exemplary changes in 2NBDG signals for WT cells starved for three days (triangles) and Δ*sodA*Δ*sodB* cells starved for eight hours (other symbols); the data showed a typical, rapid decrease in 2NBDG signals upon nutrient upshift. **(C, D)** We subjected a three-day-starved culture to nutrient upshift. Dormant cells did not produce fluorescent proteins for several hours or a day; see the initial plateau in the fluorescence intensity (Fig. 2. 10C). Fluorescence intensity increased suddenly at later times (Fig. 2. 10C), indicating the spontaneous recovery of protein anabolism. This recovery was associated with growth resumption (Fig. 2. 10D). Note that we used ampicillin to avoid unrestricted growth of metabolically-active cells (see text). With ampicillin, cells elongate without division until they eventually lyse [143], which is why cells appear unusually long in the plot. Out of ~4500 cells monitored, we observed 24 cells exhibiting such late recoveries. We observed similar fractions in two biological repeats.

We wondered whether these cells were dormant. Dormancy refers to a reversible non-growth state [86], meaning that dormant cells can later revert back to a growth state. Thus, we wished to monitor these cells for longer periods of time. However, the metabolically-active cells that initiated growth early multiplied exponentially and overwhelmed the microscope field of view within a few hours (Fig. 2. 11).

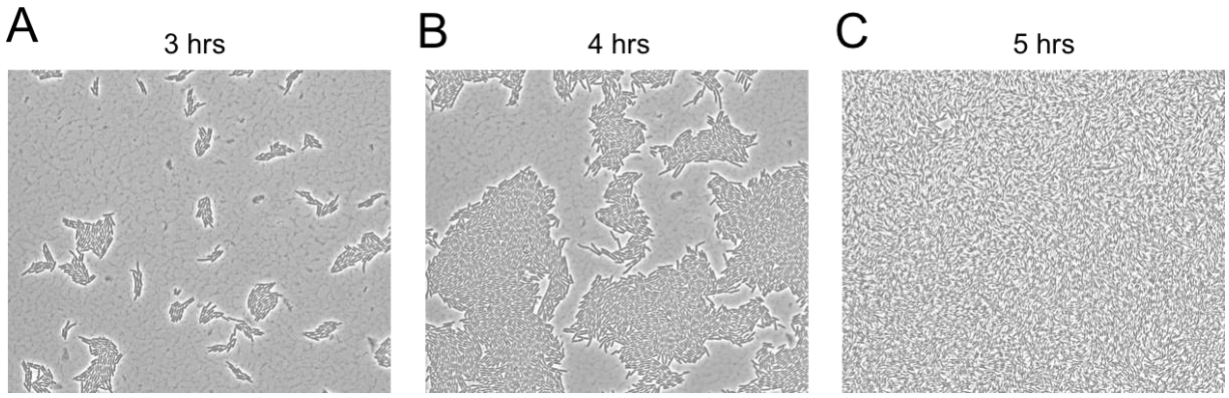

Figure 2. 11. Microscope field of view being overwhelmed by growing cells.

In the main text, we stated that the microscope field of view was overwhelmed by exponentially growing cells within a few hours of plating. Here, we show an example. We plated 47 hour-starved cells on a LB agarose plate. After three to four hours, it was already difficult to track individual cells. Within five hours, the field of view was completely overwhelmed by cells.

Thus, a long-term observation of non-growing cells with partial metabolic activities was challenging. To overcome this issue, we used an antibiotic, ampicillin, which selectively kills growing cells [144]. With ampicillin, growing cells elongate without dividing and eventually lyse [143]. Hence, the unrestricted exponential growth described above can be avoided. Our control experiments with and without ampicillin indicated no significant effects of ampicillin on our findings of metabolic activities (See Methods for detail). A long-term observation of the non-growing cells with partial metabolic activities showed no production of fluorescent proteins in

them for several hours or a day after nutrient upshift; see the initial plateau in Fig. 2. 10C. However, at later times, protein productions suddenly began (Fig. 2. 10C), indicating spontaneous recovery of anabolic activities. This recovery was accompanied by growth resumption (Fig. 2. 10D). Therefore, these metabolically-partially-active cells were dormant cells, and they were capable of reverting to a growth state through metabolic recovery. These data show a unique metabolic state associated with dormancy. Also, they reveal metabolic heterogeneity underlying heterogeneous growth phenotypes.

Taken together, our observations above indicate that a viable population can be divided into a metabolically-active subpopulation and a partially-active subpopulation. We determined the relative size of the latter subpopulation using the percentage of each subpopulation reported in Fig. 2. 3A and Fig. 2. 10B. The fraction of cells with partial metabolic activities was initially negligible but increased with longer periods of starvation (Fig. 2. 13A), revealing a dynamic change in phenotypic composition with starvation.

2.3.3. Oxidative stress induces the emergence of dormant cells with partial metabolic activities.

Starvation induces complex physiological responses in cells [2], and thus, the mechanistic determination of how starvation results in the emergence of a subpopulation with partial metabolic activities is a challenging task. However, the observation that the duration of starvation has significant effects on the size of this subpopulation may guide us to identify innate factors involved in the emergence of this subpopulation. Importantly, the results described above showed that these factors must lead to the loss of anabolic activity, but not substrate uptake and catabolic activities.

Furthermore, this loss must be transient and its recovery lead to growth resumption. We next sought to find a potential factor that satisfies these specific requirements.

Oxidative stress is a universal stress that most aerobic organisms experience to varying degrees. Previous studies have shown that prolonged starvation inflicts oxidative stress to bacterial cells, and the stress leads to failure of cells to form visible colonies on nutrient-rich agar plates after overnight incubation [145-148]. These studies assumed that the failure to form visible colonies is due to viability loss. However, our observation above showed that prolonged starvation leads to the emergence of dormant cells, which can spontaneously resume growth at later times; thus, they are unlikely to form visible colonies after overnight incubation. Based on these results, we wondered whether oxidative stress could cause the emergence of dormant cells through transient inactivation of anabolism, meaning it could be a potential factor that satisfies the specific requirements put forth above. Below, we present the data supporting this argument.

To test the effect of oxidative stress, we generated a strain prone to oxidative stress, and characterized its metabolic activities and growth resumption kinetics. The *sodA* and *sodB* genes in *E. coli* encode superoxide dismutases, enzymes that detoxify superoxide [149-152]. Deletion of these genes disables key defense mechanisms, and renders cells prone to oxidative stress, thereby amplifying the effect of oxidative stress; we refer to this double deletion mutant as the oxidative-stress-prone strain. As discussed above, starvation inflicts oxidative stress to cells [145-148]. In the case of wild-type (WT) cells, as previously described, we had to starve cells for nearly two days to see a noticeable increase in the number of cells with partial metabolic activities (Fig. 2. 10B and Fig. 2. 13A). However, in the oxidative-stress-prone strain, a shorter period of starvation

was expected to be sufficient. Thus, we starved a stress-prone population of carbon for eight hours and then spread them on LB agarose plates. We indeed observed many dormant cells with partial metabolic activities. These cells exhibited strong 2NBDG signals and a rapid decrease in signals upon nutrient upshift (Fig. 2. 10A) but did not produce fluorescent proteins (Fig. 2. 12). Thus, these cells are metabolically partially active. Importantly, these cells began protein production spontaneously at later times (several hours or a day after nutrient upshift), and this production was accompanied by growth recovery (Fig. 2. 12). Therefore, these cells with partial metabolic activities were dormant cells and could revert to a growth state.

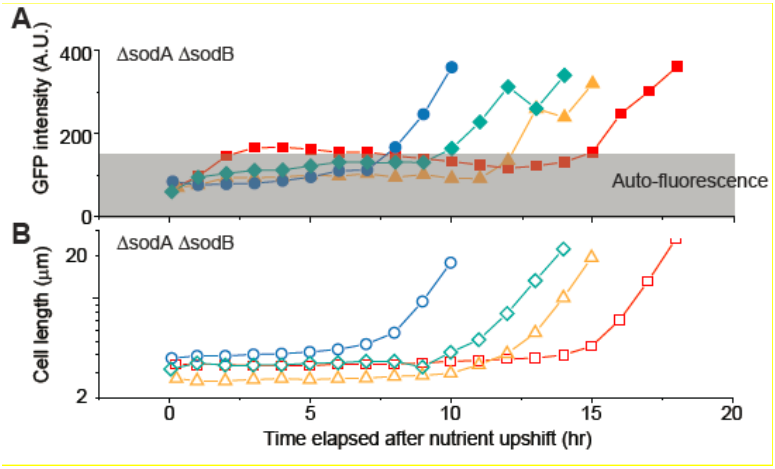

Figure 2. 12. Synthesis of green fluorescent proteins (GFP) in the oxidative-stress-prone cells.

In the main text, we described dormant cells in a WT culture that was starved and subjected to nutrient upshift. They did not grow due to inactive anabolism for an extended period of time. Later, their anabolism was restored (judged from an increase in GFP intensity) and their growth was recovered. See Fig. 2. 10C and Fig. 2. 10D. When we used the oxidative-stress-prone strain (Δ*sodA*Δ*sodB* mutant), we observed a much higher fraction of such cells. See the main text and Fig. 2. 13B for details. The figure here shows four representative cells. They did not produce fluorescent proteins for several hours or a day after nutrient upshift; see the initial plateau in GFP intensity (panel A). At later times, GFP intensity began to increase, i.e., the recovery of anabolism. This recovery was accompanied by growth resumption; see panel B.To demonstrate the abundance of such dormant cells in the stress-prone population, we plotted the distribution of time points at which cells resumed growth, i.e., lag time distribution (blue in Fig. 2. 13B); as a control, we plotted the lag time distribution for the WT population subjected to the same condition (red in Fig. 2. 13B).

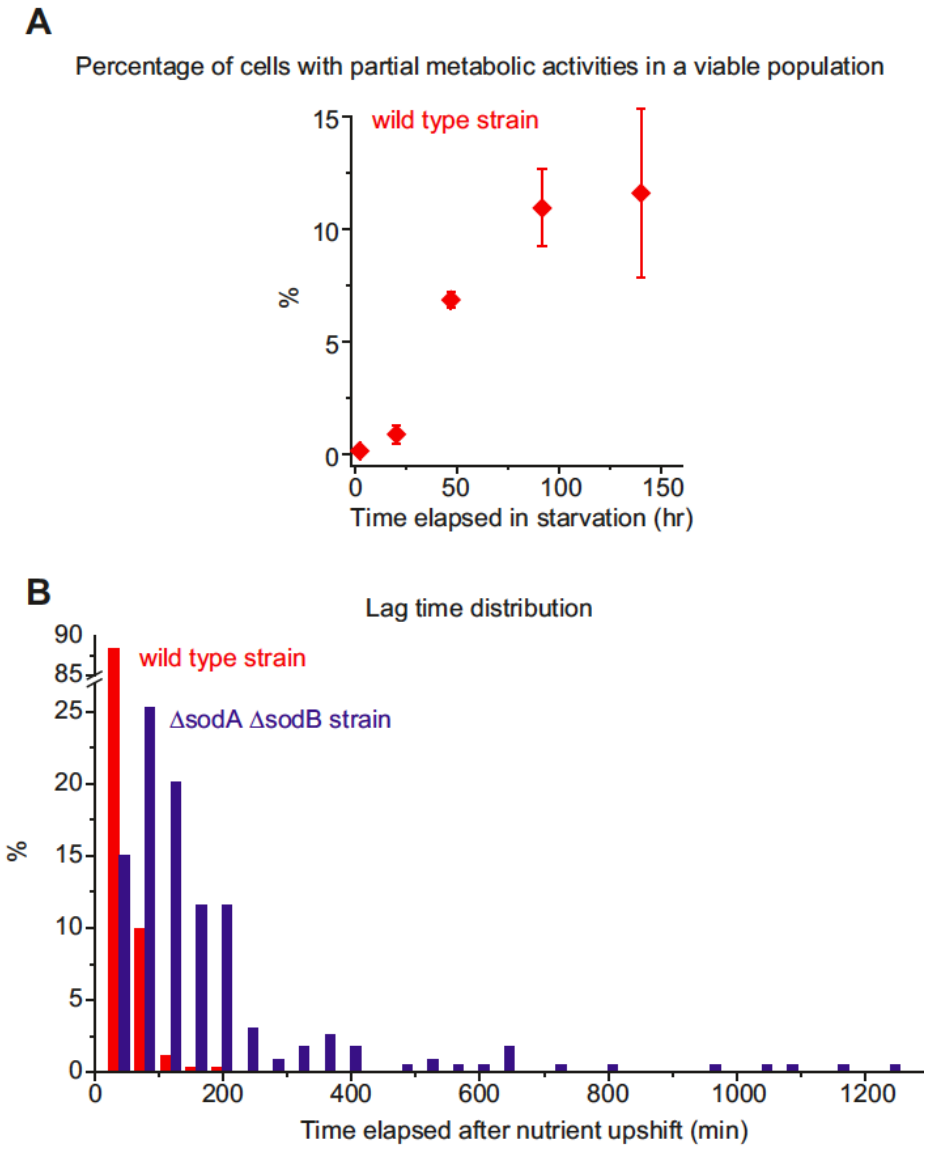

Figure 2. 13. Effects of oxidative stress on the emergence of metabolically-partially-active, dormant cells.

(A) Our observations indicated that a viable population could be divided into a metabolically-active subpopulation and a partially-active subpopulation. When we calculated the relative size of the partially-active subpopulation using the percentage of each subpopulation reported in Fig. 2. 3A and Fig. 2. 10B, we observed that its size was initially negligible, but increased with longer periods of starvation. **(B)** We examined the metabolic activities and growth of oxidative-stress-prone cells (Δ*sodA*Δ*sodB*); see text. We starved these cells and WT cells (as a control) for eight hours, subjected them to nutrient upshift, determined the time points at which cells resumed growth (lag time), and plotted the lag time distribution. ~350 WT cells and ~250 stress-prone cells were analyzed. We performed two biological repeats and these distributions were reproducible. We re-plotted these distributions as scatter plots in a semi-log scale in Fig. 2. 14.

The stress-prone cells exhibited a much wider distribution than WT cells; its tail stretched significantly farther, showing an increase in the fraction of dormant cells (see Fig. 2. 14 for further discussion).

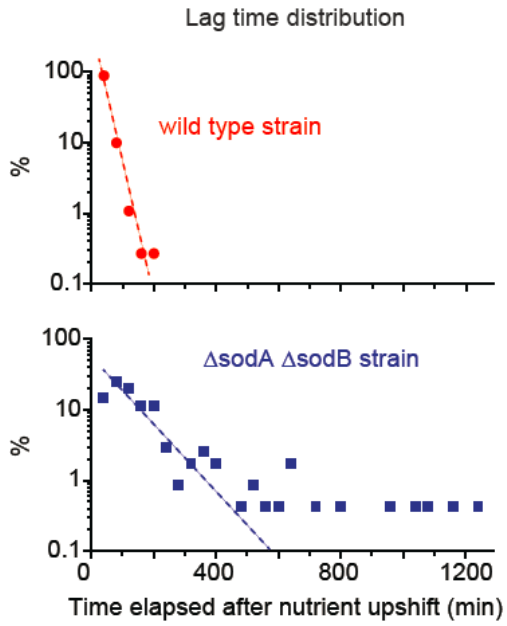

Figure 2. 14. Re-plot of lag time distribution from Fig. 2. 13B.

We re-plotted the lag time distribution of the WT strain and oxidative-stress-prone strain (Fig. 2. 13B) as a scatter plot in a semi-log scale. For the WT strain (upper panel), the distribution exhibits a linear decrease in a semi-log plot (red dashed line), indicating an exponential decay. Below, we briefly demonstrate the meaning of an exponential decay. We consider a system with N_0 constituents which decay with a single kinetic constant, β. Then, the number of constituents in the system, N, decreases in the following manner, . The solution is , meaning that N decays with single exponential kinetics. Thus, a single decay process can account for the exponential decay in the WT distribution. For the stress-prone strain (lower panel), the distribution initially followed a linear line (blue dashed line), but deviated from it after ~500 min, suggesting that its growth resumption is governed by multiple processes.

We quantified this tail by determining what fraction of cells in a population have the lag time greater than 100 min. The fraction was more than 10-fold higher in the stress-prone population (63.6 ±16.2%) compared to the WT population (4.6 ± 4.6 %); the error represents one standard deviation from two biological replicates. Next, we performed another experiment in which we

exogenously induced oxidative stress in WT cells by using H_2O_2. As shown in Fig. 2. 15, the fraction of cells with the lag time greater than 100 min increased dramatically with H_2O_2 treatment, consistent with our finding above for the oxidative-stress-prone strain.

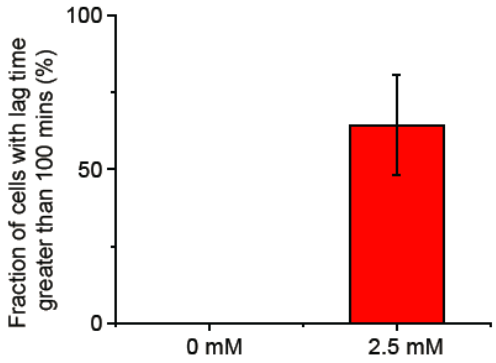

Figure 2. 15. The emergence of dormant cells by H_2O_2 treatment.

In the main text, to show that oxidative stress induced the emergence of dormant cells, we plotted the lag time distribution for the *sodA sodB* double knockout mutant and WT strain (Fig. 2. 13B). We observed a long tail in the distribution for the mutant. We then quantified this tail by determining what fraction of cells had lag time greater than 100 min. Here, to further show the effect of oxidative stress on the emergence of dormant cells, we applied oxidative stress externally using H_2O_2. We starved WT cells briefly (approximately one hour) and added H_2O_2 to the culture at a final concentration of 0 mM (control) or 2.5 mM. Then, after one hour of H_2O_2 treatment, we transferred cells to a LB agarose plate containing no H_2O_2. We monitored the growth of ~500 cells and ~ 200 cells for 0 mM and 2.5 mM H_2O_2, respectively, using a microscope. Then, similarly to what we did above, we determined what fraction of cells had the lag time greater than 100 min. The plot shows that the fraction was zero for 0 mM and increased significantly with 2.5 mM H_2O_2. The error bar represents one standard deviation from two biological replicates.

We further probed the effects of oxidative stress using a conventional colony formation assay. We starved oxidative-stress-prone cells and WT cells for eight hours, plated them, and recorded the time at which individual colonies became visible to the naked eye. Then, we compared their time distributions of the colony formation. The distribution for the WT cells was narrow (Fig. 2. 16, red columns), showing that all WT cells formed visible colonies within ~12 hours after plating. The distribution for the oxidative-stress-prone cells were much wider, with its tail stretching to ~50

hours (Fig. 2. 16, blue columns); this means that some cells formed visible colonies ~50 hours after plating. This long tail in the time distribution agrees with our single-cell-level data above. Collectively, these data reveal that oxidative stress leads to the emergence of dormant cells through transient inactivation of anabolism.

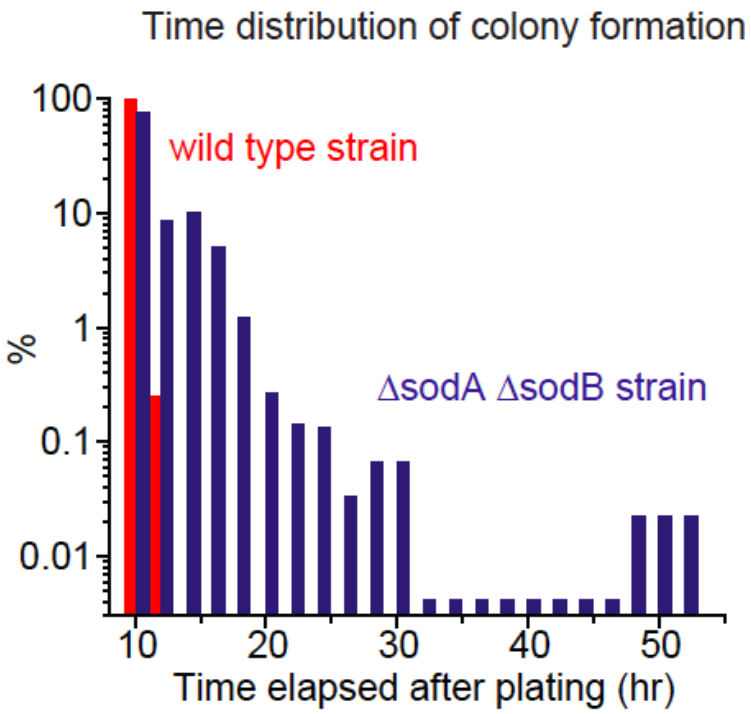

Figure 2. 16. Wide distribution of colony formation time for the oxidative-stress-prone cells.

The wild-type strain and Δ*sodA*Δ*sodB* strain were starved for 8 hours and then plated on LB agar plates. Subsequently, we recorded the time at which visible colonies were newly formed (~500 colonies were examined for each strain). Compared to the wild-type strain, the Δ*sodA*Δ*sodB* strain exhibited a much wider distribution, with its tail stretching to ~50 hours. We observed similar distributions in two biological replicates.

2.4. Discussion.

Population diversification is a critical adaptation mechanism to changing environments [21, 22]. Previous studies of genetic diversity extensively characterized how genetic composition in a

population changes slowly. In this study, we characterized the metabolic heterogeneity and its effect on phenotypic diversity in a clonal population. The results revealed the dynamic changes in phenotypic composition in a clonal population, cellular variations driving such changes (metabolic heterogeneity), and a factor triggering such cellular variations (oxidative stress).

Importantly, our findings provide a fresh metabolic perspective of dormancy. Dormant bacteria are common in nature, having significant ecological consequences [86]. However, our understanding of dormancy remains limited. For example, although it has been generally assumed that dormant cells are metabolically inactive [153], their metabolism has not been characterized. Our study reveals a metabolic state of dormant cells; dormant cells are metabolically partially active, exhibiting active substrate uptake and catabolism but inactive anabolism. This understanding sheds new light on their maintenance of viability. Dormant cells are ecologically important because they can remain viable for long. For example, due to this property, they can contribute to recovery of a microbial population after disturbance [52, 55]. However, bacteria, just to stay viable, must take up and catabolize nutrients. This "maintenance requirement" arises due to the fact that it takes substrates and energy to repair chemical wear and tear of cellular materials, maintain the membrane potential, and fulfill other non-growth-related functions [154, 155]. Previously, with the assumption of inactive metabolism, it was not clear how dormant cells could meet this maintenance requirement. Yet, our findings of active substrate uptake and catabolism in dormant cells suggest how this maintenance requirement could be satisfied. Also, our results showed that oxidative stress induces dormancy. Oxidative stress is a common stress that most aerobic microbes experience in nature, and thus could contribute to the common occurrence of dormancy.

Oxidative stress induces complex cellular responses in cells, and studies have extensively characterized how oxidative stress leads to changes in gene expression [152, 156, 157]. For example, one study showed that oxidative stress increases the expression of the efflux pump AcrAB, and the increased expression leads to extrusion of toxic compounds, resulting in better survival of cells [158]. Another study showed that oxidative stress activates OxyR and phage-shock responses, enhancing bacterial survival in stress conditions [159]. Our findings reveal that oxidative stress also has significant effects on metabolic activities and thereby on phenotypic states of cells.

Our findings raise a concern about the colony formation assay, one of the most frequently performed techniques in microbial research. In this assay, microbial samples are spread on a nutrient-rich agar plate, and then the number of viable colonies formed after overnight incubation is counted to determine the number of viable cells in the original samples. This assay is routinely used to determine microbial soil contamination or the presence of pathogens in drinking water. Studies of microbial dynamics critically rely on this assay as well. Our finding showed how cells with partial metabolic activities are viable but fail to grow in nutrient-rich conditions. In fact, when environmental microbial samples are plated on agar plates containing rich nutrients (e.g., LB), many cells fail to grow to form colonies, a long-standing problem known as “great plate count anomaly” [120, 121]. Our findings provide a fresh metabolic perspective on this problem and also prompt a cautious interpretation of assay results.

Lastly, we want to emphasize that phenotypic diversity can have significant effects on evolutionary dynamics and vice versa. For example, recent studies of experimental evolution showed that

phenotypic diversity may evolve under fluctuating selection [160] and further accelerates evolutionary adaptation to various other environmental challenges [161, 162]. Therefore, our findings would be useful for understanding the evolution of microbes in nutrient-limiting conditions, e.g., emergence of mutants expressing the growth advantage in stationary phase (GASP) during long-term starvation conditions [30, 32].

2.5. Methods.

Strain and Culture

The strains used in this study are derived from *E. coli* K12 strain NCM3722 [163-165]; see Table 2.2 for the strains used. We cultured cells in N-C- minimal media [125], supplemented with 20 mM glucose (the sole carbon source) and 20 mM ammonium chloride (the sole nitrogen source). We starved these cells of carbon by suspending them in the same medium but without glucose (starvation medium). At the times indicated, starved cells were collected and plated on Luria-Bertani (LB) solid medium for CFU assays (see Methods) or for microscope experiments (see below); this exposure to LB represents nutrient upshift. All cell cultures were performed at 37°C. We further described the details of strains and cultures below.

Microscope experiments required immotile strains; thus, NMK52 (NCM3722, Δ*motA*) or its derivatives were used [166]. To make deletion strains, single gene deletion alleles (from the Keio deletion collection [167, 168]) were transferred to our NCM3722 strains using P1 transduction [169]. The Km^r gene was flipped out by transformation of pCP20 [167, 168].

For batch cultures, cells were cultured at 37°C with shaking at 250 rpm in a water bath (New Brunswick Scientific). To monitor their growth, the optical density (OD_{600}) of the culture was measured using a Genesys20 spectrophotometer (Thermo-Fisher) with a standard cuvette (16.100-Q-10/Z8.5, Starna Cells Inc).

Our typical experimental procedure was as follows. Cells were taken from –80°C stocks and first cultured in 5 ml LB medium at OD_{600} of ~0.001 (seed culture). Note that cells enter stationary phase at OD_{600} of 2 or higher. At OD_{600} of ~0.5 (before cells entered stationary phase), we re-suspended cells in 5 ml minimal growth medium at very low densities (typically lower than OD_{600} of ~0.0001) and cultured them overnight (pre-culture). The inoculation with such low densities ensured that cells were growing exponentially the next morning; typically, the OD_{600} of the pre-culture the next morning was 0.2 – 0.5. Then, the pre-culture was diluted in pre-warmed, 5 ml minimal growth medium (experimental culture) to OD_{600} of ~0.01 (20 – 50 times dilution) and allowed to grow exponentially to OD_{600} of ~0.6. Then, cells were re-suspended in 5 ml starvation medium. We emphasize that cells had been kept in exponential growth phase throughout the procedure (for ~25 doublings), until they were suspended in starvation medium. After cells were suspended in starvation medium, 100 µl of the starved culture was collected for microscope experiments (see below) or for CFU assays (see below).

It is a typical practice in the field to use LB solid medium for CFU assays, even when cells were grown and starved in minimal medium. We followed this practice for our CFU assays and also microscope experiments. For one condition (two-day starvation), we repeated the microscope experiments by replacing the LB solid medium with a minimal solid medium containing glucose

(the sole carbon source). Cells elongated slower with the minimal solid medium. When we examined their growth resumption and determined the percentages of viable cells that resumed growth within 100 minutes after nutrient upshift, the results were similar with LB solid and minimal solid media (93.1% with LB medium and 96.0% with minimal medium).

The data in Fig. 2. 13B and Fig. 2. 16 were obtained from experiments that involved the comparison of the WT strain (NMK52) and the Δ*sodA*Δ*sodB* double deletion strain (NMK223 or NMK256). However, the latter cells do not grow in minimal medium [170, 171]. Thus, for these experiments, both WT and deletion strains were cultured in LB medium. Subsequently, cells were washed and re-suspended in the starvation medium.

Table 2. 2. Bacterial strains used in Chapter 2.

Strain	Genotype	Derived from	Comment	Reference
NCM3722	-	-	*E. coli* K-12 wild-type strain	[163, 164]
NMK52	Δ*motA*	NCM3722	*motA* deletion	[166]
NMK141	Δ*motA*, pTet-gfp (intC), pCon-tetR-lacIq (attB)	NMK52	pTet driving the expression of *gfp* at the *intC* locus, pCon driving the expression of *tetR* at the *attB* locus	Stock of Laboratory of Minsu Kim
NMK145	Δ*motA*, pTet-mCherry (ycaD), pCon-tetR-lacIq (attB)	NMK52	pTet driving the expression of mCherry at the *ycaD* locus, pCon driving the expression of *tetR* at the *attB* locus	Stock of Laboratory of Minsu Kim
NMK223	Δ*motA*, Δ*sodA*, Δ*sodB*	NMK52	*motA*, *sodA*, and *sodB* deletion	This study
NMK256	Δ*motA*, Δ*sodA*, Δ*sodB*, pTet-gfp (intC), pCon-tetR-lacIq (attB)	NMK141		This study

Microscope experiments

Our typical procedure for a microscope experiment is as follows (also see Fig. 2. 2 for the graphic illustration of the experimental procedure). At the times indicated, 100 µl of a culture was collected and transferred to a 1.5 ml Eppendorf tube. 2NBDG (Thermo-Fisher) was added into this aliquot. We prepared a 2NBDG stock solution by dissolving it in N-C- medium (stock concentration: 0.5 mM) and added it to the aliquot at a final concentration of 10 µM; this concentration of 2NBDG does not support cell growth (Fig. 2. 5). In some cases (Fig. 2. 8), to visualize dead cells, PI (Thermo-Fisher) was added to the aliquot at a final concentration of 10 µM (its stock solution was prepared by dissolving it in N-C- medium at a concentration of 2 mM). After incubation for 25 min in the dark at 37°C, a 5-8 µl aliquot from this sample was spread onto a pre-warmed 35 mm glass-bottom Petri dish (InVitro Scientific). Then, the dish was moved into a pre-warmed (at 37°C) inverted microscope (Olympus IX83). A pre-warmed (~1.6 cm^2 × 1 mm) LB agarose pad was gently placed on top (i.e., nutrient upshift). The microscope has an automated mechanical XY stage and auto-focus and is controlled by MetaMorph software (Molecular Devices). Furthermore, it is housed in a microscope incubator (InVivo Scientific) which maintains the temperature of samples at 37°C during experiments. An oil immersion 60× objective was used to obtain phase-contrast and fluorescence images of cells. FITC and TRITC filter sets (Olympus) were used to collect fluorescence signals. Images were captured using a Neo 5.5 sCMOS camera (Andor). In some experiments, there were minor variations in the procedure. In some experiments, there were minor variations in the procedure. We described these variations below.

For experiments requiring long-term observations of cells, to selectively kill growing cells, ampicillin (BioBasic) was added to an LB agarose pad at a final concentration of 100 µg/ml. For

experiments involving the expression of GFP from the synthetic promoter P_{tet}, anhydrotetracycline hydrochloride (aTc; Sigma-Aldrich) was added to the pad. The final concentration of aTc was 100 ng/ml; this concentration of aTc had no significant effects on cell growth; see Fig. 2. 17. aTc diffuses into cells rapidly within a couple of seconds [134].

A

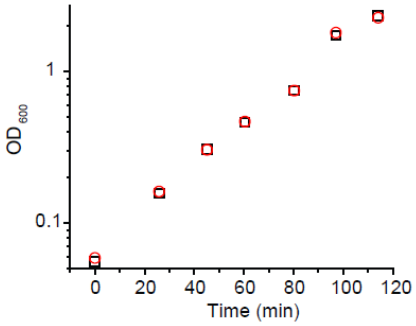

B

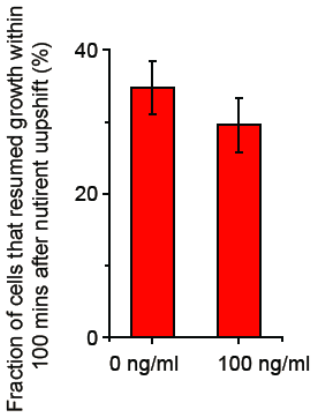

Figure 2. 17. No significant effects of aTc on cell growth.

In our experiments, to induce the expression of fluorescence proteins, we added 100 ng/ml of aTc to growth medium. **(A)** To test the effects of this concentration of aTc on cell growth, we first measured the batch culture growth with 100 ng/ml of aTc and without aTc. We cultured *E. coli* cells in LB medium with aTc (black squares) and without aTc (red circles) and measured their OD_{600} as a function of time. Their growth curves were almost identical (panel A). This experiment was repeated independently four times, and such identical growth curves were reproducible. **(B)** Next, we examined how 100 ng/ml of aTc affects the growth resumption of starved cells upon nutrient upshift, by comparing the fraction of cells that resumed growth

within 100 min. (A different time window may be used for comparison. Our choice of 100 min was motivated by our early observation, which was discussed in the main text, that all metabolically-active cells resumed growth within 100 min after nutrient upshift.) Following the experimental procedure described in the main text, we starved cells of glucose for three days and spread them on LB agarose plates with and without 100 ng/ml of aTc. We monitored ~3000 cells (for each experiment) using time-lapse microscopy and determined which cells resumed growth within 100 min after nutrient upshift; see the Methods for detail. Their percentages were reported in panel B, 34.7 ± 3.7 % without aTc and 29.6 ± 3.8 % with aTc; we performed two biological repeats and the error bars reflect one standard deviation from these biological replicates. As shown in the figure, the error bars overlap. The *t* test shows that the two-tailed *p* value is equal to 0.3060, indicating that the difference in the percentage with and without aTc is not statistically significant. These results, taken together, show negligible effects of 100 ng/ml aTc on cell growth.

To characterize the relative fractions of metabolically active and partially active cells (Fig. 2. 3A and Fig. 2. 10B), we delayed nutrient upshift by placing an additional layer of agarose pad under an LB agarose pad. This additional pad was made by using starvation medium containing 2NBDG. It typically took 10 min for LB to diffuse through the pad and reach cells, which allowed us to assess intracellular 2NBDG signals before nutrient upshift.

To characterize the 2NBDG degradation in cells (Fig. 2. 3C and Fig. 2. 10A), 600 µl of a culture was mixed with 2NBDG at final concentration of 10 µM and loaded onto a glass bottom 35 mm Petri dish (InVitro Scientific). The dish was then put on a microscope stage and incubated for ~45 minutes at 37°C. Then, 1800 µl of pre-warmed LB broth medium was gently added (which defined time zero). During this incubation period and after the addition of LB, intracellular 2NBDG signals of individual cells were measured.

We note that the inducer aTc is light-sensitive. Therefore, our samples containing aTc were kept in the dark most of the time, except for brief periods of imaging. The samples were imaged three times per hour for the first two hours and once per hour later, with an exposure time of 300 ms or less. Therefore, we believe that aTc degradation by light was minimal. This is further supported

by our data. We added aTc to our sample at time zero. The data presented in Fig. 2. 10C and Fig. 2. 12A show that *de novo* synthesis of fluorescent proteins still occurred after ~ 20 hours, meaning that aTc was present and activated the P_{tet} promoter.

Image analysis

Image analysis was performed using MicrobeJ [172], a freely available plug-in for the ImageJ software [98]. This program can automatically segment cell boundaries from phase-contrast microscope images ("*segmentation"*) and measure the cell length ("*shape descriptors"*). Also, it can measure intracellular fluorescence intensities ("*intensity"*). To obtain a lag-time distribution, we ran this program for time-lapse images, obtained cell sizes at different times, and determined the time points at which cell sizes changed. We confirmed these time points by re-examining them manually. In some cases, we simply had to determine how many cells resumed growth within a certain time window (e.g., Fig. 2. 15 and Fig. 2. 17). Then, we placed two images, one at time zero (the first image taken after nutrient upshift) and the other at the end of the time window, side by side. We visually compared the sizes of cells in these two images and determined which cells became larger.

Colony-forming unit (CFU) assay

At the times indicated, we collected 100 µl of starved cultures, diluted it serially (10^3 ~ 10^6-fold dilution depending on the time of starvation), and spread it on an LB agar plate. The dilution factor was determined such that the number of colonies on each plate (100 × 15 mm Petri dish) was between 50 and 250. After plating, the plates were incubated at 37°C overnight. From the number of visible colonies on the LB agar plates the next day, the number of CFU per milliliters (ml) was

determined. To obtain the data presented in Fig. 2. 16, we determined the time points at which visible colonies were formed. We were able to detect colonies reliably when colonies grew to be of a diameter of at least 0.5 mm. Hence, when colonies grew to become the diameter of ~0.7 mm, we marked it as the time of colony formation.

In this study, we characterized the metabolic activities and growth resumption of starved cells subjected to nutrient upshift. To monitor cells for long periods of time, we added ampicillin. Here, to examine if ampicillin has any significant effects on our findings, we compared the metabolic activities and growth resumption of three-day starved cells with and without ampicillin.

In both cases, we observed the same predicted patterns of 2NBDG molecules and fluorescent proteins in metabolically-active cells. With and without ampicillin, these cells exhibited a rapid decrease in 2NBDG signals, and an increase in fluorescence intensity of fluorescent proteins, soon after nutrient upshift. In both cases, these cells resumed growth within 100 min after nutrient upshift. Their percentage in the populations were similar as well, 32.2 (±2.5) % without and 28.4 (±3.8) % with ampicillin. The *t* test shows that the two-tailed *p* value is equal to 0.3589, indicating that the difference in the percentage with and without ampicillin is not statistically significant. Therefore, ampicillin had little effects on metabolic activities of these cells, their growth resumption, and their percentages.

Also, the patterns of 2NBDG molecules and fluorescent proteins in metabolically partially active cells were the same with and without ampicillin, i.e., a rapid decrease in 2NBDG signals, but no increase in fluorescence intensity of fluorescent proteins, after nutrient upshift. None of these cells

resumed growth within 100 min after nutrient upshift. Their percentages in the populations were similar, ~4 %. However, without ampicillin, we could not quantify their percentage accurately nor follow their metabolic activities long enough to make thorough comparisons, because the metabolically-active cells that initiated growth early overwhelmed the microscope field of view soon (which is why we had to use ampicillin). Yet, within our observation time window (nearly three hours), metabolic activities of these cells and their fractions were similar.

Given that ampicillin targets cell wall synthesis and that no significant difference was observed in our control experiments with and without ampicillin, we do not believe ampicillin has significant effects on our findings of metabolic activities.

2.6. Movie Caption.

The supplementary movie is available at The *ISME* Journal's website

We starved *E. coli* cells of glucose for 2.3 hours and added 10 μM of 2NBDG into the culture (10 μM of PI was also added to stain dead cells). After 15 min, the cells exhibited strong 2NBDG signals (Fig. 2. 4). We then spread them on LB agarose plates (nutrient upshift) and monitored them using a time-lapse fluorescence microscope. A time-lapse image sequence is shown here. 2NBDG and PI signals are presented as green and red colors, respectively, using a linear adjustment function (meaning that signal intensity and brightness were linearly mapped); the same adjustment function was used for the whole image sequence. This image sequence shows a rapid change in 2NBDG signals after nutrient upshift. We had to visualize a very large change in 2NBDG signals (~100-fold, Fig. 2. 3C) using one adjustment function. Consequently, small

changes in 2NBDG signals at later time points (e.g., after about ten minutes) are not visually discernable in this sequence.

Chapter 3: Power-law tail in lag time distribution of bacteria: its origin and implication for bacterial persistence in the face of antibiotics

Emrah Şimşek[1] and Minsu Kim[1,2,3]

[1]Department of Physics, Emory University, Atlanta, GA, 30322. U.S.A.

[2]Graduate Division of Biological and Biomedical Sciences, Emory University, Atlanta, GA, 30322. U.S.A.

[3]Emory Antibiotic Resistance Center, Emory University, Atlanta, GA, 30322. U.S.A.

Submitted for publication in a peer-reviewed journal (March 2019)

3.1. Abstract.

Genetically-identical microbial cells respond to stress heterogeneously, and this phenotypic heterogeneity contributes to population survival. Quantitative analysis of phenotypic heterogeneity can reveal dynamic features of stochastic mechanisms that generate heterogeneity. Additionally, it can enable *a priori* prediction of population dynamics, elucidating microbial survival strategies. Here, we quantitatively analyzed the persistence of an *Escherichia coli* population. When a population is confronted with antibiotics, a majority of cells are killed but a subpopulation called persisters survives the treatment. Previous studies have found that persisters survive antibiotic treatment by maintaining a long period of lag phase. When we quantified the lag time distribution of *E. coli* cells in a large dynamic range, we found that normal cells rejuvenated with a lag time

distribution that is well captured by an exponential decay [exp (-*kt*)], agreeing with previous studies. This exponential decay indicates that their rejuvenation is governed by a single rate constant kinetics (i.e., *k* is constant). Interestingly, the lag time distribution of persisters exhibited a long tail captured by a power-law decay. Using a simple quantitative argument, we demonstrated that this power-law decay can be explained by a wide variation of the rate constant *k*. Additionally, by developing a mathematical model based on this biphasic lag time distribution, we quantitatively explained the complex population dynamics of persistence without any *ad hoc* parameters. The quantitative features of persistence demonstrated in our work shed new insights into molecular mechanisms of persistence and advance our knowledge of how a microbial population evades antibiotic treatment.

3.2. Introduction.

Many stochastic systems, although they may consist of completely different microscopic components, can exhibit quantitatively similar fluctuations, which suggests the universality in stochastic processes. For example, a wide variety of seemingly unrelated stochastic processes, e.g., radioactive decay, the number of car accidents at a given site, etc. can be captured by the Poisson dynamics, thus sharing similar features, e.g., exponential time distribution of the events [173, 174]. Importantly, demonstrating such quantitative features can provide a new understanding of dynamic mechanisms that generate system-level fluctuations, enabling *a priori* prediction of fluctuations. Furthermore, demonstrating such quantitative features can reveal connections between seemingly unrelated phenomena that share similar features.

A microbial cell is a stochastic system because biochemical reactions inside of it are inherently stochastic [65, 114, 175-179]. Due to this inherent stochasticity, genetically-identical cells can exhibit a great deal of phenotypic heterogeneity [25, 47-50]. From a clinical perspective, the most important example of phenotypic heterogeneity is a phenomenon known as persistence [180-182]. As first reported by Joseph Bigger [183], when a clonal bacterial population is exposed to a bactericidal drug, a majority of cells die quickly while a minority called persisters survives for long periods of time, resulting in complex population survival dynamics.

To better understand these population dynamics, extensive studies have focused on molecular mechanisms of persistence. While a large number of genes that can alter the levels of persistence have been identified, there is a substantial controversy regarding how these genes are activated and how they contribute to persistence [184-189]. As such, with the current knowledge of molecular mechanisms alone, we cannot predict the population dynamics of persistence, e.g., what percentage of cells in a population is persisters and how their percentage changes over time.

Various theoretical modeling efforts have been made to understand the population dynamics of persistence [104, 190-193]. These models typically contain coupled differential equations with parameters describing the dynamics of antibiotic killing and switching between normal and persister cells. To explain the complexity of population dynamics of persistence, some models introduced additional processes, e.g., two different types of persisters or dependence of switching on substrate/antibiotic concentrations, etc. The parameter values associated with these processes were often determined by fitting the models to population dynamics data. But, the number of free

parameters in some of these models raises concerns about overfitting. More importantly, the quantitative signature governing persistence has rarely been discussed in these studies.

Single-cell-resolution imaging was proven to be a valuable tool for studying persistence. It was shown that when cells in stationary-phase (hence non-dividing) were suspended in a fresh growth-permissive medium, a majority of cells rejuvenate and resume growth immediately, but a small subpopulation maintains the non-dividing state (i.e., lag phase) for an extended period of time [101, 103, 104, 106, 194]. Because a non-dividing state confers cells tolerance to antibiotics, this subpopulation can survive antibiotic treatment, contributing to persistence. Collectively, these studies established that lag phase plays a critical role in persistence.

In this work, we quantitatively characterized a large dynamic range of lag time distribution of *E. coli* cells, demonstrating its intricate quantitative feature. Additionally, we show that this quantitative feature alone can account for the population dynamics of persistence without *ad hoc* parameters. We then discuss the population structure that gives rise to the observed quantitative feature, the connection between this quantitative feature and the current molecular understanding of persistence, and the clinical implication of this quantitative feature.

3.3. Results and Discussion.

3.3.1. Multiphase population dynamics of isogenic bacteria exposed to an antibiotic.

We first characterized the population dynamics of persistence by measuring a time-dependent killing curve of a population exposed to an antibiotic. The stationary phase was shown to play an

important role in persister generation; e.g., maintaining a culture in the exponential phase for an extended period of time eliminates persisters [195]. Thus, to enrich persisters in a culture, most studies kept cells in stationary phase before suspending them in fresh medium containing an antibiotic [101, 104, 106, 196, 197]. In our experiments, we kept cells in stationary phase for three days and suspended them in fresh LB medium containing ampicillin (100 μg/ml); the moment of suspension defines time zero. To measure a time-dependent killing curve, we performed a colony-forming unit (CFU) assay at different times by spreading a small volume of the culture onto an LB agar plate containing no ampicillin. We then incubated the plates overnight, enumerated CFUs, and determined N_{CFU} (the number of CFUs at time t normalized by the number of CFUs at time zero). Agreeing with previous studies, a complex multiphase killing curve was observed (Fig. 3. 1) [100, 104, 198-200]. Importantly, the long tail of the curve indicates persistence.

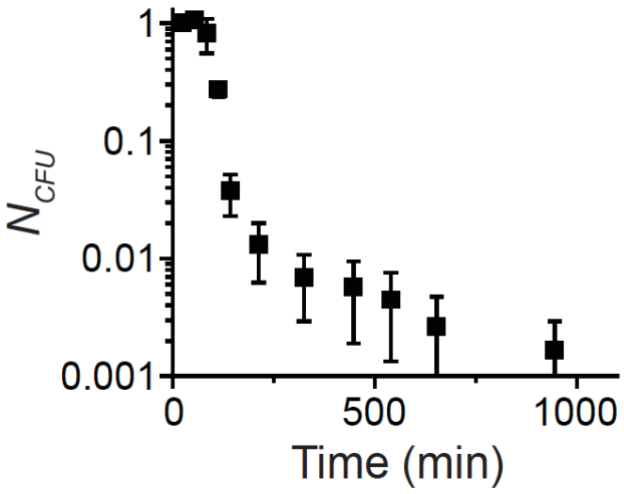

Figure 3. 1. Time-dependent killing curve of a population exposed to ampicillin.

Stationary phase cells were suspended in fresh LB medium containing 100 μg/ml of ampicillin (time zero). A colony-forming unit (CFU) assay was performed at different times. N_{CFU} represents normalized CFU, i.e., the number of CFUs at time t divided by the number of CFUs at time zero. Agreeing with previous studies [100, 104, 198, 199], a complex multiphase killing curve was observed. The long tail of the curve indicates persistence. For each time point t, at least two biological replicates were performed, and their mean (data points) and standard deviation (error bars) were shown. Within each biological replicate, at least four technical replicates were performed, and their average was used for the plot.

3.3.2. Single-cell-level observation of lag time.

Previous studies have shown that a long lag phase of a minority of cells contributes to persistence [101, 103, 104, 106]. Thus, we used single-cell time-lapse microscopy to determine the periods of lag phase (lag time) of individual cells. We prepared a culture as described above and determined how long it takes for cells from a stationary phase culture to rejuvenate and resume growth in fresh LB medium. Fig. 3. 2a shows a rejuvenation probability distribution, which is also called a lag time distribution in the field (these two terms are used interchangeably in this chapter).

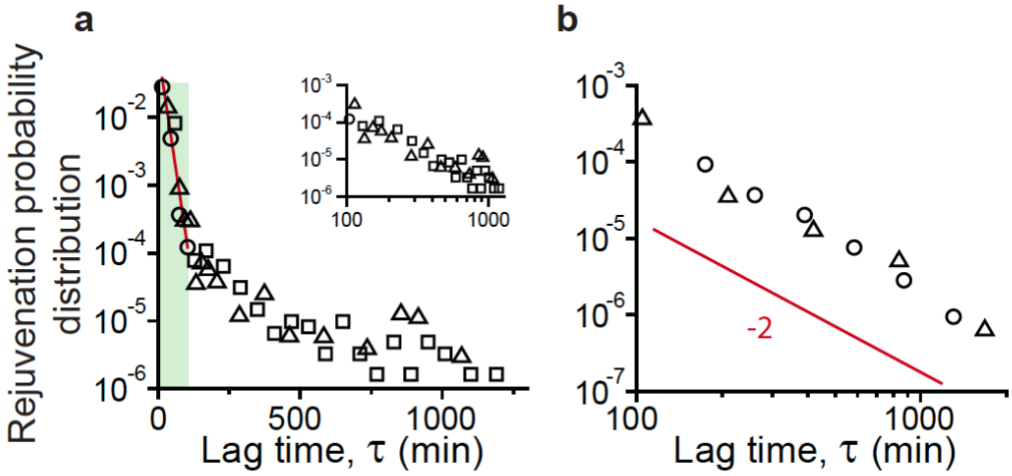

Figure 3. 2. Rejuvenation probability distribution (or lag time distribution).

(a) Using time-lapse microscopy, we determined the time points at which cells from stationary phase rejuvenate and resume growth upon suspension to fresh LB medium (~ 12800 cells were analyzed in three independent experiments). The rejuvenation probability initially decreased rapidly over time (green region), and this initial decrease was well approximated by an exponential decay (linear line). After a rapid decrease of nearly three orders of magnitude, the decrease slows down dramatically, deviating from the exponential decay (to the right of the green shaded region). In the inset, we re-plotted this late regime in a log-log scale. A linear decrease in a log-log scale suggests a power-law decay. (b) In statistical studies, it is common to use logarithmic data binning to visualize a power-law decay of a distribution [201]. The data shown in the inset (Fig. 3. 2a) were replotted after logarithmic binning. The power law exponent is approximately –2 (the red line has a slope of –2). Note that the values of all our raw data as well as processed data (logarithmically binned) are provided in Appendix. This biphasic decay, $f(\tau)$, was mathematically formulated in Eq. 1. The parameter values in Eq. 1 were determined using the experimental data as described in the Methods section (τ_0 = 93 min, k = 0.063 min^{-1} and β = –2.1, A_1= 0.0622 min^{-1} and A_2= 2.42 min$^{1.1}$).

The rejuvenation probability decreased rapidly in the first 100 minutes, and this decrease was well approximated by an exponential decay (linear line in green shaded region in Fig. 3. 2a). This exponential decay agrees with previous observations in other studies; see Fig. 3. 3.

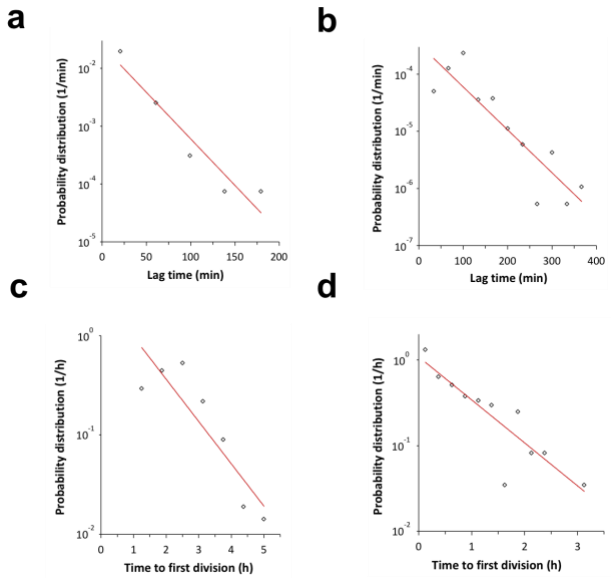

Figure 3. 3. Early, exponential decay of lag time distribution

We observed an exponential decay in the early part of lag time probability distribution (Fig. 3. 2). Previous population dynamic modeling studies often assumed that lag time distribution of bacterial cells exhibits an exponential decay [202, 203]. Other experimental studies investigated two or three orders of magnitude decrease of lag time distribution (the range comparable to that of our early part of distribution where we observed an exponential decay). Here, we re-plotted the data of these experimental studies and fit them with an exponential function, which shows that an exponential decay is a good approximation. (a) In the studies by Şimşek and Kim [204], *E. coli* cells were starved of carbon for eight hours, and then suspended in LB medium. Lag times of individual cells were determined by microscopy at 37 °C. The red straight line in a semi-log scale indicates an exponential decay with R^2 = ~ 0.917. The data were reproduced from Supp. Fig. 13. (b) In the study by Levin-Reisman *et al*. [205], *E. coli* cells were starved and suspended in a complex medium. Lag times of individual cells were determined by microscopy at 32 °C. The red straight line in a semi-log scale indicates an exponential decay with R^2 = ~ 0.802. The data were reproduced from Fig. 1d. (c) In the study by Kutalik *et al*. [206], *Listeria innocua* cells were starved and suspended in complex medium. The time to the first division of individual cells was determined by microscopy at ambient temperature. The red straight line in a semi-log scale indicates an exponential decay with R^2 = ~ 0.802. The data were reproduced from Fig. 4 (upper panel). (d) In the study by Francois *et al*. [207], *Listeria monocytogenes* cells were starved and suspended in complex medium. The time to the first division of individual cells was determined by optical density measurements using microtiter plates at 30 °C. The red straight line in a semi-log scale indicates an exponential decay with R^2 = 0.775. The data were reproduced from Fig. 2 (upper left panel).

What distinguishes our dataset from others' is its large dynamic range. The aforementioned studies of lag time distribution characterized two or three orders of magnitude of decrease in the distribution, thus focusing mostly on rejuvenation of normal cells. Although recent single-cell-level studies directly observed a minority of cells with a long lag phase (i.e., persisters) [100, 101, 103, 104, 106], these studies have not thoroughly quantified the lag time distribution of these cells. In this work, by tracking a large number of cells (~ 12800 cells in three independent experiments), we quantified a large dynamic range of rejuvenation probability. We observed that after the initial exponential decay of rejuvenation probability (by nearly three orders of magnitude), the decrease slows down dramatically, deviating from the exponential decay (to the right of the green shaded region in Fig. 3. 2a). Interestingly, when we re-plotted the data in the second regime in a log-log scale, we observed a linear decrease (Fig. 3. 2a, inset), suggesting a power-law decay. In many statistical studies, it is common to use logarithmic data binning to show a power-law decay of a distribution [201]. When we binned our data logarithmically, we again observed the same linear trend (Fig. 3. 2b); note that the values of all our raw data as well as processed data (logarithmic binned) are provided in Appendix. The power law exponent was found to be approximately –2 (Fig. 3. 2b line). Power law distribution is a widespread feature in many stochastic processes, observed in physics, ecology, earth sciences and social sciences (e.g., self-organized criticality, earthquake, word usage, etc.) [201]. Typically, these empirical distributions exhibit a power-law decay only in the tail; it is rare that distributions follow a power-law decay for all their values. This is the case for the rejuvenation probability observed in our study as well.

Collectively, our single-cell-level data above indicate that the rejuvenation probability, $f(\tau)$, is biphasic and well captured by

$$f(\tau) = \begin{cases} A_1 \cdot \exp(-k \cdot \tau) & \text{for } \tau < \tau_0 \\ A_2 \cdot \tau^{\beta} & \text{for } \tau \geq \tau_0 \end{cases}, \qquad \text{(Eq. 1)}$$

where k, τ_0, and β are respectively the rate constant in the initial exponential decay, the time at which the probability distribution transitions to a power law decay, and the power law exponent. A_1 and A_2 are normalization constants that are related to the proportion of normal and persister cells. The actual values of these parameters were determined from the experimental data as described in the Methods section and provided in the caption for Fig. 3. 2 and Table 3.1.

Parameter	Empirical	Best fit
k	0.0630 min^{-1}	0.105 min^{-1}
β	-2.1	-2
Δ	102 min	100 min
τ_0	93 min	47 min
A_1	0.0622 min^{-1}	0.10211 min^{-1}
A_2	2.42 $min^{1.1}$	1.6219 min

Table 3. 1. Empirically determined and best fit parameters for modeling the time-dependent killing curve

Our mathematical model for describing the time-dependent killing curve is given by Eq. (1-3) in the main text. The parameters of this model presented above were determined empirically (second column) and from the best fit (third column) as described in detail in Methods.

3.3.3. Time delay of ampicillin killing.

Having quantitatively characterized the temporal distribution of rejuvenation probability, we sought to use this distribution to better understand the complex time-dependent killing curve (Fig.

3. 1). Importantly, persisters are different from antibiotic-resistant cells in that once persisters rejuvenate and resume growth, they are killed by antibiotics. Therefore, to understand the time-dependent killing curve, we must know how quickly growing cells are killed by ampicillin. Propidium iodide (PI) staining was previously shown to be an excellent indicator of dead *E. coli* cells [136-139, 204]. We additionally confirmed that PI is a good indicator for cell death by ampicillin; when we incubated cells with ampicillin and PI for 80 min and spread them on an LB agar plate containing no ampicillin, none of the PI stained (PI+) cells grew (see Methods for detail). One issue of PI is the loss of nucleic acids upon lysis by ampicillin. PI stains nucleic acids, but lysis results in the loss of cytoplasmic contents, including nucleic acids [136-139, 204]. Hence, lysed cells are, although they are clearly dead, not stained by PI. On the other hand, we can distinguish lysed cells by their refractivity; when observed via phase-contrast microscopy, a live *E. coli* cell is normally refractile (i.e., it exhibits a dark area with sharp boundaries) whereas lysed cells exhibit poor phase-contrast with diffuse boundaries [204]. Therefore, we tracked PI-staining and lysis to evaluate ampicillin killing. We found that on average it takes 102 min for ampicillin to kill growing cells (see Fig. 3. 4). We denote this time delay of killing by Δ (= 102 min). A similar time delay of ampicillin killing was observed in previous studies [143].

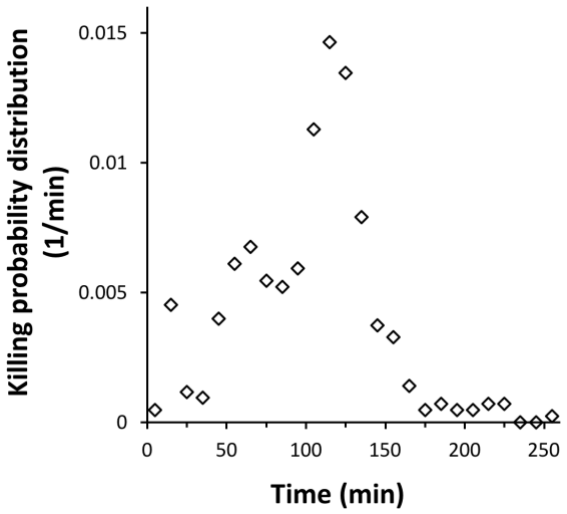

Figure 3. 4. Time delay of ampicillin killing.

As described in the main text, we evaluated the time of ampicillin killing by exposing growing cells to ampicillin (100 μg/ml final concentration) and tracking propidium iodide (PI)-staining or the loss of cell refractivity (whichever comes first). Here, we plotted the distribution of ampicillin killing time, which showed that on average, it takes Δ = 102 min for ampicillin to kill growing cells. The distribution was obtained from two biological repeats. ~ 200 cells were examined within each biological repeat. Average killing time varied by less than 7 % across the two biological repeats when separately analyzed.

3.3.4. Mathematical framework bridging lag time distribution and time-dependent killing curve.

To quantitatively understand the population dynamics of persistence, one could model switching between normal and persister cells using ordinary differential equations. More realistic models can be constructed by including the dependence of switching rates on various factors such as substrate concentration, e.g., see [192]. One potential problem of this approach, however, is overfitting; although a model may fit a curve, fitting itself may not justify the underlying assumption of the model. Here, we take an alternative approach. We believe that our single-cell studies above have identified the central kinetics underlying persistence (i.e., the biphasic decay of rejuvenation probability distribution). If these kinetics govern persistence as we believe, they must be able to account for the time-dependent killing curve without any *ad hoc* parameters.

To do so, we must clarify the relationship between rejuvenation probability and a time-dependent killing curve. As discussed above, a time-dependent killing curve is measured by performing CFU assays at different times, that is, a small volume of a sample was taken from a culture growing in LB with ampicillin and spread on an LB plate (without ampicillin) at time *t*. Thus, the CFU data report the number of viable cells at the time *t*. Given the time delay of ampicillin killing Δ (as shown above), the cells that had rejuvenated and resumed growth any time before $t - \Delta$ would be killed, failing to form colonies. Mathematically put, the fraction of dead cells at time *t* is then equal to $\int_0^{t-\Delta} f(\tau)d\tau$, where $f(\tau)$ is the rejuvenation probability. Conversely, the fraction of viable cells capable of forming colonies on a LB plate when assayed at time *t*, *g*(*t*), is given by

$$g(t) = 1 - \int_0^{t-\Delta} f(\tau)d\tau \qquad \text{(Eq. 2)}$$

Because we already know the function of rejuvenation probability $f(\tau)$ (Eq. 1), we can calculate *g*(*t*). The result was plotted as a black line in Fig. 3. 5. In the same figure, we replotted the empirical time-dependent killing curve (from Fig. 3. 1) as black points, which shows a good agreement. Importantly, our mathematical model highlights three different phases. First, for *t* less than Δ (= 102 min), there would not be enough time for ampicillin to kill cells. Thus, *g*(*t*) is 1 (green region in Fig. 3. 5).

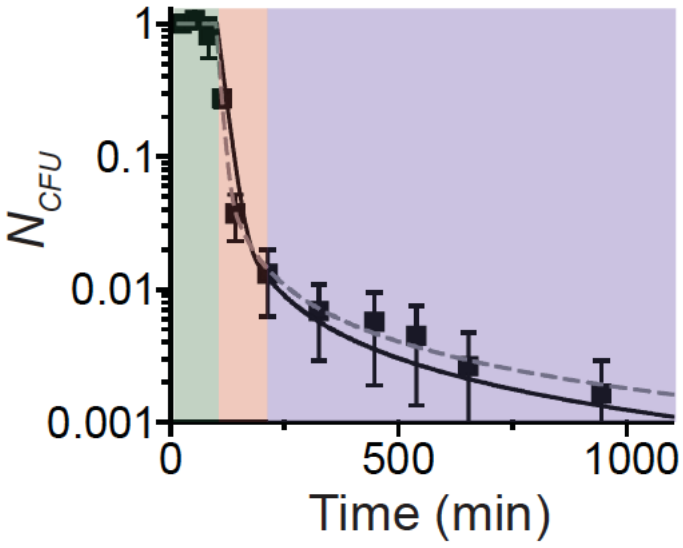

Figure 3. 5. Comparing the model prediction of a time-dependent killing curve with experimental data.

We mathematically related the rejuvenation probability distribution (*f*) and the fraction of viable cells (*g*) in Eq. 2. Using the rejuvenation distribution *f* (which was fully specified in Eq. 1 and Fig. 3. 2 caption), we calculated the fraction of viable cells *g* and plotted the result as a black line. The empirical time-dependent killing curve (from Fig. 3. 1) was replotted as black points, which shows a good agreement. Importantly, our mathematical model highlights three different phases as marked by different shades. See text for details. Here, the parameter values used to compute g were previously obtained using the data plotted in Fig. 3. 2. We then varied these parameter values to find the best fit. The best-fit curve (grey dashed line) looked similar to the original prediction based on empirically determined parameter (black solid line). Also, the best fit parameter values are similar to those determined empirically (see Table 3.1).

A majority of cells rejuvenate and resume growth within the first 105 min (Fig. 3. 2 caption), but these cells are killed by ampicillin after a time delay Δ, leading to a rapid decay of N_{CFU} between Δ (= 102 min) and Δ (= 102) + 105 min (red region in Fig. 3. 5.). The rejuvenation probability exhibits a long tail after 105 min (Fig. 3. 2b), leading to a long stretch of N_{CFU} after Δ (= 102) + 105 min (blue region in Fig. 3. 5). Thus, the rejuvenation probability can account for the complex time-dependent killing curve without *ad hoc* parameters.

Here, all the parameter values in this model were determined empirically from single-cell-level experiments (Fig. 3. 2) and thus would be affected by experimental error. Next, by allowing the parameter values to vary, we searched for the best fit of the model to the killing curve. The best-fit curve (grey dashed line in Fig. 3. 5) agreed with the experimental killing data (black points) marginally better than the original prediction (black solid line), although they are very similar. The parameter values from the fitting are found to be similar to those used originally (determined empirically from single-cell-level data); see Table 3.1.

3.3.5. Quantitative mechanisms for exponential or power-law decays in rejuvenation probability.

An exponential decay distribution is common in natural phenomena (e.g., radioactive decay [174]). An exponential decay indicates first-order kinetics with a single rate constant. To demonstrate this point, we consider non-growing cells rejuvenating and resuming growth at a constant rate of k. Then, the number of non-growing cells at a given time $N(t)$ is governed by

$$\frac{dN(t)}{dt} = -kN(t)\,. \qquad \text{(Eq. 3)}$$

The solution of Eq. 3 is

$$N(t) \propto \exp(-k \cdot t)\,. \qquad \text{(Eq. 4)}$$

The rejuvenation probability we measured in our experiments refers to the number of cells resuming their growth during a given time interval Δt, $\overline{N}(t)$, which is given mathematically by

$$\overline{N}(t) = -\frac{\Delta N(t)}{\Delta t} \propto k \cdot \exp(-k \cdot t)\,. \qquad \text{(Eq. 5)}$$

Eq. 5 indicates that a homogeneous population that resumes growth with a single rejuvenation constant *k* exhibits an exponential decay in rejuvenation probability distribution.

How can we understand the power-law decay in the later part of the distribution (Fig. 3. 2b)? The mathematical derivation shown above (Eq. 3-5) clearly indicates that a homogeneous population with a single rejuvenation constant cannot exhibit a power-law decay. To quantitatively understand a power-law decay, we then consider a heterogeneous population. For the sake of simplicity, we first consider a population consisting of two subpopulations with two different rejuvenation constants k_1 and k_2. In this case, using Eq. 5, we can write that the number of cells resuming their growth at a specific time *t*, $\overline{N}(t)$, is given by

$$\overline{N}(t) \propto k_1 \cdot \exp(-k_1 \cdot t) + k_2 \cdot \exp(-k_2 \cdot t) \ . \qquad \text{(Eq. 6)}$$

Extending this formula, for a large number of such subpopulations, we have

$$\overline{N}(t) \propto \sum_{i=1}^{n} k_i \cdot \exp(-k_i \cdot t) \ , \qquad \text{(Eq. 7)}$$

or

$$\overline{N}(t) \propto \int_0^\infty k \cdot \exp(-t \cdot k) \cdot dk \ . \qquad \text{(Eq. 8)}$$

Since $\int_0^\infty k \cdot \exp(-t \cdot k) \cdot dk = -\frac{d}{dt} \cdot \int_0^\infty \exp(-t \cdot k) \cdot dk$ and $\int_0^\infty \exp(-t \cdot k) \cdot dk = 1/t$, Eq. 8 becomes

$$\overline{N}(t) \propto \frac{1}{t^2} \qquad \text{(Eq. 9)}$$

Thus, for a heterogeneous population in which cells rejuvenate with various rate constants, the rejuvenation probability is expected to exhibit a power-law decay with exponent of –2, as we observed in our experiments (Fig. 3. 2b).

3.3.6. Power-law decay provides a quantitative framework for understanding complex molecular processes underlying persistence.

How can we relate this power-law nature of rejuvenation probability distribution to the current molecular understanding of persistence? Molecular mechanisms of persistence have been extensively characterized [181, 208, 209]. Previous studies of persisters have shown that toxin and antitoxin systems cause persistence [104, 210-213], but increasing evidence supports that there are many other genes that lead to persistence, such as *phoU*, *tolC*, *oxyR*, etc [159, 214-216]. Additionally, various errors in the cell replication cycle or metabolism as well as cells' stress response to such errors lead to the non-dividing state of persisters [217-223]. Collectively, these studies indicate that a myriad of different molecular processes can contribute to generation and rejuvenation of persisters. For example, some cells could enter a non-dividing state because of toxin overproduction and rejuvenate when toxins get degraded (by antitoxins). Some cells could enter a non-dividing state due to glitches in DNA replication and rejuvenate when the glitches are repaired. As such, a persister subpopulation is a diverse collection of various cells whose growth was transiently halted by different mechanisms [224]. Since different persister cells enter and exit a lag phase through different mechanisms, rejuvenation kinetics of persisters are expected to be highly heterogeneous, meaning a wide variation of rejuvenation constants within a persister subpopulation. As our derivation above (Eq. 6-9) shows, such a wide variation of rejuvenation constants would lead to a power-law decay in rejuvenation probability. Therefore, our findings of

a power-law decay in rejuvenation probability distribution agree with previous findings that a myriad of mechanisms generate persisters. More importantly, this quantitative feature provides a coherent framework for a systems-level understanding of these complex molecular mechanisms.

3.3.7. Further implication of a power-law decay.

In statistics and probability, a long tail in a probability distribution indicates a large number of occurrences far from the central part of the distribution. A power-law distribution is a classic example of a long-tailed distribution. This is why a power-law decay in rejuvenation probability distribution leads to a long stretch in the time-dependent killing curve (Fig. 3. 5). In fact, we quantitatively explained this stretch with the power-law distribution without invoking any *ad hoc* parameters (Fig. 3. 5).

From a clinical point of view, this long tail distribution is problematic because it indicates that some persister cells rejuvenate and resume growth after maintaining a very long period of lag phase. Unfortunately, many conventional antibiotics have little efficacy for these cells during lag phase, killing them only once they rejuvenate. Therefore, for infections containing persister cells, an extended antibiotic treatment is required for eradication. This is why for infections by agents with a high number of persisters, e.g., *Mycobacterium tuberculosis*, antibiotic treatment lasts more than six months (still then, the chance of eradication is not 100 %). Therefore, our observation of a power-law decay in rejuvenation probability further highlights the need to develop new antibiotics that can directly target persister cells, supporting current efforts in the field to identify chemicals that kills persister cells [225].

3.4. Methods.

Strain and Cell Culture

We used an *E. coli* K12 NCM3722 *ΔmotA* strain [166]. For batch cultures, cells were cultured at 37 °C with shaking at 250 r.p.m. in a water bath (New Brunswick Scientific). To monitor growth in batch cultures, the optical density (OD_{600}) of the culture was measured using a Genesys20 spectrophotometer (Thermo-Fisher) with a standard cuvette (16.100-Q-10/Z8.5, Starna Cells Inc). Our typical experimental procedure was as follows. Cells were taken from -80 °C stocks and first cultured in an LB medium for 4 - 6 hours (seed culture). Then, they were transferred to N^-C^- minimal medium (pH = 7) [125] supplemented with 40 mM of ammonium chloride and 40 mM of glucose (glucose minimal medium) at very low densities (typically lower than OD_{600} of ~ 0.0001) and cultured overnight (pre-culture). The low densities were used to ensure that the cells were growing exponentially the next morning. These cells were then diluted (20 ~ 50 times) and sub-cultured in pre-warmed fresh glucose minimal medium (experimental culture). The cells grew exponentially for at least four more doublings before they were spun down and re-suspended in the same type of minimal medium without glucose (i.e., starvation medium). On the third day of the starvation, a small volume of the culture was transferred to fresh pre-warmed LB medium containing ampicillin (BioBasic) to measure a time-dependent-killing curve experiments or for the microscope experiments as described below.

Microscopy

All our single-cell-level observations were made using an inverted microscope (Olympus IX83). The microscope had an automated mechanical XY stage and auto-focus, which were controlled by MetaMorph software (Molecular Devices). The microscope is housed in an incubator (InVivo

Scientific) which ensured maintenance of a desired temperature in the experiments (37 °C). Images were captured using a Neo 5.5 sCMOS camera (Andor).

Image analysis

Image analysis was performed using MicrobeJ, a freely available plug-in for the ImageJ software [172]. This plug-in can automatically segment cell boundaries from phase-contrast microscope images ("*segmentation"*) and measure the cell length ("*shape descriptors"*).

Colony forming unit (CFU) assay for experimentally determining time-dependent-killing curve

For Fig. 3. 1, CFU assays were performed to determine a time-dependent killing curve of a bacterial population exposed to ampicillin. On the third day of starvation (67.7 - 70.5 hours), cells were transferred to a fresh pre-warmed rich (LB) medium with 100 µg/ml ampicillin (time zero), and incubated at 37 ℃. At different time points *t*, a fixed volume was spread on LB agar plates (100 × 15 mm Petri dish) containing no ampicillin after appropriate serial dilutions. The plates were then incubated at 37 ℃ overnight. Next morning, we counted visible colonies (which varied between 30 – 300) on the LB agar plates and determined the CFUs per milliliter. For each time point *t*, at least two biological replicates were performed, and their mean (data points) and standard deviation (error bars) were reported in Fig. 3. 1. Within each biological replicate, at least four technical replicates were performed, and their average was used.

Single-cell level observation of lag time

For Fig. 3. 2, on the third day of starvation (70.1 - 73.7 hours), a 5 µl aliquot of cells was spread onto a pre-warmed 35 mm glass-bottom Petri dish (InVitro Scientific). Then, a pre-warmed LB agarose pad with an approximate volume of 2.4 ml containing ampicillin (100 µg/ml final concentration) was gently placed on top of the cells such that the pad covered the entire bottom surface of the dish. The dish was then sealed with parafilm to limit water evaporation and immediately moved to a pre-warmed (37 °C) microscope for time-lapse imaging. An oil immersion 60× objective was used to acquire phase-contrast images of the cells.

The lag time of individual cells (Fig. 3. 2) was measured using a time-lapse microscopy. Cells were imaged at different time points, their size was calculated using MicrobeJ, and the duration for which a cell maintained its size was used to determine its lag time. To visualize a power law, it is common to bin data logarithmically [201]. We logarithmically binned the data shown in Fig. 3. 2a to produce Fig. 3. 2b. Briefly, defining the bottom of the lowest bin and the ratio of the widths of successive bins as x_{min} and a, the k^{th} bin extends from $x_{k-1} = x_{min}\, a^{k-1}$ to $x_k = x_{min}\, a^k$. Importantly, Fig. 3. 2b represents probability distribution, and thus the number of observations made within each bin was normalized by the bin width. For triangles, x_{min} = 70 min and a = 2. For rectangles, x_{min} = 140 min and a = 1.5.

Single-cell level determination of time delay in ampicillin-killing of growing cells

To determine the time delay (Fig. 3. 4), cell culture was first maintained in exponential growth phase for at least nine doublings until it reached OD_{600} = 0.2 - 0.3 in LB broth, and then a 4 µl

aliquot was spread onto a pre-warmed 35 mm glass-bottom Petri dish (InVitro Scientific). Then, a pre-warmed LB agarose pad with an approximate volume of 2.4 ml containing ampicillin (100 µg/ml final concentration) was gently placed on top of the cells such that the pad covered the entire bottom surface of the dish. The dish was then sealed with parafilm to limit water evaporation and immediately moved to a pre-warmed microscope for time-lapse imaging at 37 °C. In this experiment, the LB agarose pad contained also propidium iodide (PI, Thermo-Fisher) at 4 µM of final concentration. An oil immersion 60× objective was used to acquire phase-contrast and red fluorescence images of the cells. Then, the distribution of time at which a cell got stained by PI or lost refractivity in its phase contrast image (i.e., lysed) (whichever comes first) was determined.

We additionally confirmed that PI is a good indicator for cell death by ampicillin; when we incubated cells with ampicillin and PI for 80 min and spread them on an LB agar plate containing no ampicillin, none of the PI stained (PI+) cells grew. A total number of ~25 PI+ ampicillin-affected cells were examined in five biological replicates.

Determination of values of τ_0, k, β, A_1 and A_2

Fig. 3. 2a shows a semi-log plot of lag time probability distribution. Data below 105 min were fitted to a linear function, yielding $k = 0.0630$ min^{-1} ($R^2 \sim 0.907$). Fig. 3. 2b shows a log-log plot. This dataset was fitted to a linear function, yielding $\beta = -2.10$ ($R^2 \sim 0.977$). τ_0, A_1 and A_2 were determined using the following three equations. First, because the lag time probability distribution is continuous, $A_1 e^{-k\tau_0} = A_2 \tau_0^{\beta}$ in Eq .1. Second, its cumulative probability is equal to 1, i.e.

$\int_0^{\tau_0} A_1 e^{-k\tau} d\tau + \int_{\tau_0}^{\infty} A_2 \tau^{\beta} d\tau = 1$. Here, $\int_0^{\tau_0} A_1 e^{-k\tau} d\tau$ is equal to the fraction of normal cells, which we empirically found to be 0.984926 (from the data presented with triangles and squares in Fig. 3. 2a); thus $\int_0^{\tau_0} A_1 e^{-k\tau} d\tau = 0.984926$. Solving these three equations, we obtained τ_0 = 93 min, A_1 = 0.0622 min^{-1} and A_2 = 2.42 $min^{1.1}$.

Determination of these parameters by fitting the time-dependent killing curve

The following ranges for the model parameters were explored using a custom-built MATLAB code; k (1/min) = [0.010, 0.200] with 0.001 increments, β = [-3.00, -1.51] with 0.01 increments, Δ (min) = [60, 200] with increments of one, and τ_0 (min) = [10, 270] with increments of one. For each set of parameters (k, β, Δ, τ_0), $\int_0^{\tau_0} A_1 e^{-k\tau} d\tau + \int_{\tau_0}^{\infty} A_2 \tau^{\beta} d\tau = 1$ and $A_1 e^{-k\tau_0} = A_2 \tau_0^{\beta}$ were solved for A_1 and A_2. Using these values, we then computed the fraction of viable cells, $g_{theo}(t)$, and compared them with experimental values (time-dependent killing data, $g(t)$). Then, the logarithmic least squares formula described below was applied.

$$\sum_{i=1}^{n=11} \left(\log_{10} g(t_i) - \log_{10} g_{theo}(t_i) \right)^2 = S$$

Finally, the set of parameters minimizing the value of S above was determined as the best-fit, whose parameter values are shown in Table 3.1. S values were 3.26×10^{-1} and 3.03×10^{-2} for the empirically determined and the best-fit parameter sets, respectively.

3.5. Appendix.

Below we provide the values for all our data.

Data for generating Fig. 3. 1 : Data points are the arithmetic mean and error bars represent the standard deviation of the values reported below for three biological replicate experiments.

Biological Replicate #1		**Biological Replicate #2**		**Biological Replicate #3**	
Time (min)	N_{CFU}	**Time (min)**	N_{CFU}	**Time (min)**	N_{CFU}
25	1.00×10^{0}	26	1.00×10^{0}	23	1.00×10^{0}
56	1.19×10^{0}	55	9.37×10^{-1}	53	1.07×10^{0}
84	1.13×10^{0}	85	6.62×10^{-1}	83	6.70×10^{-1}
113	3.08×10^{-1}	114	2.83×10^{-1}	112	2.32×10^{-1}
142	5.14×10^{-2}	143	3.77×10^{-2}	143	2.29×10^{-2}
212	2.09×10^{-2}	217	1.06×10^{-2}	213	7.88×10^{-3}
322	1.14×10^{-2}	330	5.03×10^{-3}	325	4.19×10^{-3}
447	8.37×10^{-3}	447	3.01×10^{-3}	N/A	N/A
539	6.66×10^{-3}	541	2.25×10^{-3}	N/A	N/A
650	5.04×10^{-3}	652	1.64×10^{-3}	657	1.23×10^{-3}
943	2.55×10^{-3}	947	7.47×10^{-4}	N/A	N/A

Data for generating Fig. 3. 2 : We provide our raw data charts below.

Data for generating Fig. 3. 2a :

Circles		**Triangles**		**Squares**	
Imaging time point, t_i (min)	**Number of observations, N_i**	**Imaging time point, t_i (min)**	**Number of observations, N_i**	**Imaging time point, t_i (min)**	**Number of observations, N_i**
30	462	69	1372	120	10077
60	81	84	19	140	16
90	6	105	9	200	66
120	2	124	8	260	39
		144	1	320	19
		164	2	380	9
		189	2	440	4
		227	2	500	6
		346	2	560	5
		403	2	620	2
		522	1	680	6
		644	1	740	2
		827	1	800	1
		883	1	860	3
		947	1	920	1
		1188	1	980	3
				1040	2
				1160	2
				1220	1

Data for generating Fig. 3. 2b :

Logarithmic binning rules, as described in Methods, were applied to the data presented above for the triangles and squares in Fig. 3. 2a. As a result, the following data chart was generated.

Triangles		**Squares**	
Logarithmically binned time point (min)	**Number of observations**	**Logarithmically binned time point (min)**	**Number of observations**
70	1372	140	10093
140	36	209	66
280	7	313	39
560	5	468	32
1120	4	700	18
2240	1	1047	10
		1565	5

Here, the data obtained from three independent experiments were presented by three different symbols; circles, triangles and squares. For each one of the independent experiments, we took time-lapse images of bacterial cells at various time points (t_1, t_2, …, t_i, t_{i+1}…) and counted the number of observations for bacterial cells that resumed growth (N_i) between t_i and t_{i-1} (where t_0 = 0). In Fig. 3. 2, lag time, τ, represents the middle points of the bins, (t_i + t_{i-1})/2. Probability distribution $f(\tau)$ represents probability divided by the bin width N_i /(ΣN_i)/(t_i - t_{i-1}).

Chapter 4: Developing visualization tools for studying surface colonization by *Proteus mirabilis* across multiple scales

4.1. Abstract.

In natural ecosystems, surface-association is the dominant lifestyle for bacteria. In laboratories, several bacterial species are known to colonize semi-solid (i.e., agar) surfaces and establish communities known as biofilms. As an isogenic population of *P. mirabilis* bacteria colonizes an agar surface, it adopts a strategy of periodic cycles between range expansions and cell growth/multiplication at the colony edge. Before each round of range expansions, a striking example of non-genetic population diversification is observed; the cells in the outermost region of a colony make a cell fate decision whether to remain normal (immotile) and exploit the available territory or differentiate and activate a flagella-dependent-motility program known as swarming for exploring new territories. Many cellular and environmental factors such as cell density, extracellular signaling, surface hardness, gene regulation, etc., have been reported to influence swarming. However, how these cellular and environmental factors collectively affect cell fate decision remains elusive. Additionally, although a number of theoretical studies recapitulated some of the key features *P. mirabilis* surface colonization at the colony level, how colony scale dynamics are related to cellular scale dynamics is unclear. This gap in knowledge is primarily due to a lack of the tools available for visualization of the phenomenon at the single-cell-level. Here, we first constructed a chromosomal transcriptional fusion of a green fluorescent protein (*gfp*) gene

to the native operon for the master regulator of motility (*flhDC*) as a reporter of the activity of swarmer cell differentiation program. We demonstrated how this construct can unveil unprecedented spatiotemporal features of population diversification within a growing cell population. Furthermore, we developed a Petri dish-based device compatible with dry-objective-optical microscopy. We demonstrated how this device can be used to visualize and link dynamic properties of swarming across a broad range of scales from the single-cell (μm/s) to the colony level (cm/h).

4.2. Introduction.

In natural ecosystems planktonic bacteria are substantially outnumbered by surface-associated bacteria [7-9]. Surface association can provide bacteria with various advantages such as increased population tolerance to antibiotic exposure compared to planktonic populations [19, 226], metabolic cooperation for better utilization of resources, and high mechanical resilience[227]. On the other hand, mainly due to restricted hydration, surface attachment is expected to impede bacterial motility on surfaces like soil [10-12] and hydrogels [13]. This may present a challenge when motility is the only option to escape from potential growth inhibitory factors such as nutrient limitation and toxic compounds. Collectively, understanding the surface colonization strategies by bacteria can help improving our understanding regarding bacterial survival strategies in nature.

When a micro-liter droplet of *Proteus mirabilis* bacteria is placed onto a nutrient agar medium in a standard culture dish (~10 cm in diameter), the bacteria entirely colonize the surface of the medium within timescales of hours, even when the agar concentration in the medium is so high (≤ 3%) such that its surface cannot be colonized by any other bacteria [228]. Therefore, *P. mirabilis*

represents a superior bacterium in the context of surface colonization. On an agar surface colonized by *P. mirabilis*, a concentric-rings (e.g., Bull's eye)-patterned biofilm is observed. This pattern is due to radially symmetric, periodic high and low cell density bands (Fig. 4.1a; brightness in the image is proportional to cell density). As an isogenic population of *P. mirabilis* bacteria colonizes an agar surface, it adopts a strategy of periodic cycles between range expansions and cell growth/multiplication at the colony edge (Fig. 4.1b). Prior to each round of range expansions a striking example of non-genetic population diversification is observed; the cells on the outermost regions make a cell fate decision whether to remain normal (immotile) or to differentiate and activate a flagella-dependent-motility program known as swarming [229-231]. Swarmers cells are highly elongated (typically more than 10-fold), and this elongation is believed to originate from a specific inhibition of cell division without affecting the doubling time of cell mass or DNA [232] as they have the same DNA to length ratio as normal cells [230, 233] (see Fig. 4.1c left panel for diverse cell morphologies). Surface sensing [234], extracellular signaling [235], cell density [236, 237], various amino acids [238], and regulation of expression of some genes [234, 239-241] have been shown to influence the phenomenon of swarming to various degrees (note that swarming and range expansions were used interchangeably in this chapter). However, how these cellular and environmental factors collectively affect population diversification (i.e., cell fate decision) between immotile and motile cells remains elusive.

Motility and chemotaxis genes are under the control of a three-tier hierarchy, at the top of which is the flagellar master regulator *flhDC* [242, 243]. The products of the *flhDC* operon are the FlhD and FlhC proteins which together comprise a hetero-hexameric complex $FlhD_4C_2$ that in turn serves as a transcription factor [244-246]. Expression of the *flhDC* operon was previously shown

to increase prior to swarmer cell differentiation, and its overexpression was reported to induce sooner and faster swarming [239, 247], while *flhDC*-deficient mutants do not swarm [248]. Hence, tracking intracellular *flhDC* promoter activity levels can be used to study the population diversification at the single cell level prior to the onset of swarming. However, currently there exist no tools available for tracking the *flhDC* promoter activity in single cells without significantly influencing the dynamic and spatial features of swarming in *P. mirabilis.* Additionally, although a number of theoretical studies recapitulated some of the key features *P. mirabilis* swarming at the colony level [232, 249-251], how colony scale dynamics are related to cellular scale dynamics is unclear. In order to help addressing these issues, we first constructed a new strain harboring a transcriptional fusion of a green fluorescent protein (*gfp*) gene to the native chromosomal *flhDC* operon to observe the activation of swarmer cell differentiation. We then demonstrate how this strain can help unveiling otherwise inaccessible spatiotemporal features of cell differentiation within a growing cell population. Furthermore, we developed a Petri dish-based device that allows to visualize and link dynamic properties of swarming across a broad range of scales from the single cell (μm/s) to the colony level (cm/h) when combined with an appropriate long working distance objective microscope.

4.3. Representative Results.

4.3.1. Spatiotemporal characterization of *flhDC* promoter activity at the single cell level using a transcriptional fluorescent reporter.

In order to monitor the expression of *flhDC* operon at the single-cell-level as a reporter of the activation of swarmer cell differentiation, we here constructed a *flhDC-gfp* transcriptional fusion

strain (AMK79). This strain had one functional copy of the *flhDC* operon at its native site in the chromosome with a green fluorescent protein (*gfp*) gene fused to it and one non-functional (i.e., truncated) copy of the *flhDC* operon at another location downstream its native site. When observed in conventional swarm assays, population level macroscopic swarming (i.e., range expansion) dynamics of this strain (Fig. 4.1b, green) were comparable to that of its parental wild-type strain (Fig. 4.1b, black).

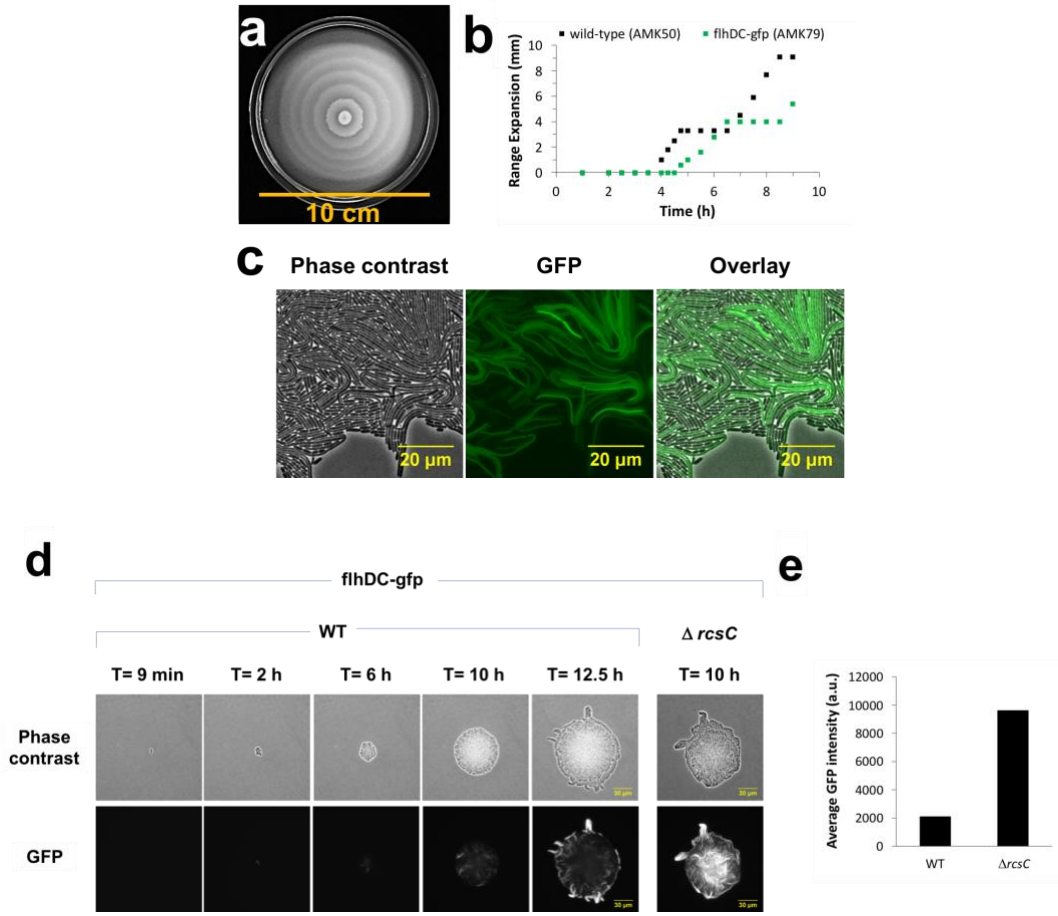

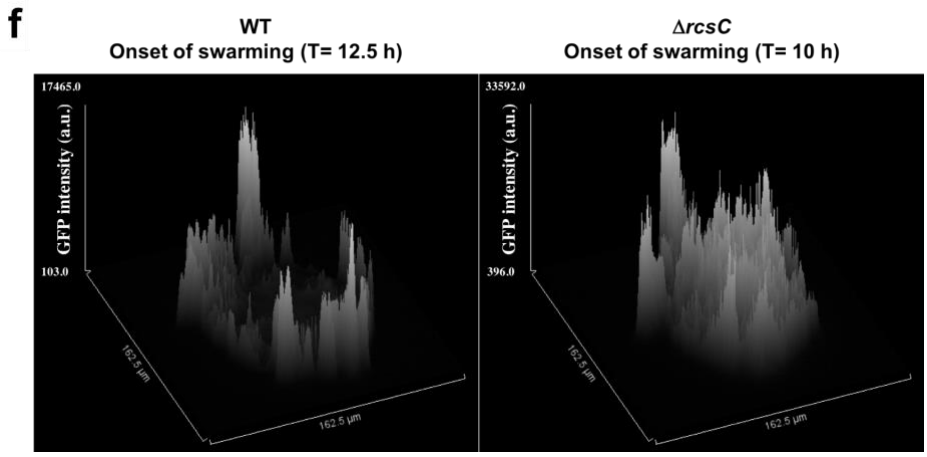

Figure 4. 1. Spatiotemporal characterization of *flhDC* promoter activity at the single cell level using a transcriptional fluorescent reporter.

a. Macroscopic concentric rings-pattern formed on the surface of an LB agar (2%) medium after being colonized by a center inoculated-*P. mirabilis* PM7002 wild-type (AMK50) colony. **b.** Temporal dynamics of range expansions of wild-type (AMK50, black) and *flhDC-gfp* (AMK79, green) bacteria on an LB agar (2%) surface. **c.** Representative phase contrast (left), GFP (middle), and overlay (right) images of a frontal region of an AMK79 colony 30 min after the onset of swarming. **d.** Phase contrast (top) and GFP (bottom) image time series of an AMK79 microcolony growing under nutrient limitation (0.2x LB was initially provided in agarose (1%) medium). *Far right*. Phase contrast (top) and GFP (bottom) images of a *flhDC-gfp* Δ*rcsC* (AMK84) strain at the onset of swarming under the same conditions. A 60x oil immersion objective was used. **e.** Average GFP intensities within the microcolonies of AMK79 (*flhDC-gfp*, T = 12.5 h) and AMK84 (*flhDC-gfp* Δ*rcsC*, T = 10 h) shown in (d). **f.** A surface plot of GFP intensities in the images shown in (d) for AMK79 (*flhDC-gfp* WT, T = 12.5 h) and AMK84 (*flhDC-gfp* Δ*rcsC*, T = 10 h).

As seen in Fig. 4.1c, only highly elongated cells exhibit high intracellular GFP intensity (elongation is one key feature of swarmer cell morphology) at the onset of swarming. In order to spatiotemporally characterize the activation of population diversification we grew (micro)colonies from one (or two) cell(s) and monitored *flhDC-gfp* driven GFP signals at the single cell level (see Fig. 4.1c, *flhDC-gfp* WT for a representative image series). Note that in order to achieve a high spatial resolution, we used a short working distance objective microscope which required covering the cells with a microscope slide. GFP signals appeared seemingly at random positions early on but were later repressed in a central region before the observation of group of cells leaving their

original colony (i.e., onset of swarming). Because such a spatiotemporal regulation of *flhDC* expression has never been reported before, our representative results demonstrate how our approach can be useful to unravel unprecedented spatiotemporal features of population diversification (i.e., differentiation) in preparation to swarming. In order to further demonstrate the use of this construct, we next deleted the *rcsC* gene from this strain yielding a mutant that should not have a functional RcsCDB phosphorelay mechanism (AMK84). RcsCDB phosphorelay is one of the most well-known regulators of the *flhDC* operon; in collaboration with the cofactor RcsA it transcriptionally represses the expression of *flhDC* in *E. coli* [252]. Furthermore, previous population averaged results showed that Rcs phosphorelay downregulates *flhDC* expression [239], while mutations of it exaggerates swarming [253]. Corroborating these previous reports, we observed that our *rcsC*-deletion (Δ*rcsC*) strain began swarming ~2.5 hours earlier, and its population averaged *flhDC* promoter activity was about five times higher than the *flhDC-gfp* WT strain at the onset of swarming (Fig. 4.1e). Moreover, in the absence of RcsC, GFP signals were no longer repressed in the central regions of a colony (compare Fig. 4.1c, *flhDC-gfp* WT at T= 12.5 h and *flhDC-gfp* Δ*rcsC* at T= 10 h). Fig. 4.1f presents surface plots for a quantitative comparison of the GFP signal intensities between these WT and Δ*rcsC* strains at the onset of swarming. GFP signals were generally higher in the Δ*rcsC* mutant. Most strikingly, looking at how the GFP signals change in the direction from the interior to the exterior of a colony, a generally increasing trend is observed for the WT strain, while a typically decreasing trend is seen for the Δ*rcsC* mutant. Overall, we here demonstrated how the *flhDC-gfp* fusion strain we constructed and single-cell approach we took here can unveil intriguing spatiotemporal regulation of swarmer cell differentiation and factors influencing it.

4.3.2. A multiscale analysis of the onset of swarming.

Previously, a number of theoretical studies based on various assumptions recapitulated some of the key macroscopic features of swarming seen in the conventional swarm assays such as concentric-rings pattern formation, and periodic switches between range expansions and cell multiplication, etc. [232, 249-251]. As seen for the last time point in Fig. 4.1c, swarming initiates as protruding groups of swarmer cells. Here we call these protrusions "fingers". These fingers are the first groups of cells crossing the boundary between the colony and the environment surrounding it. Characterization of this fingering phenomenon can help one better understand physicochemical factors governing the initiation of swarming and how they affect the macroscopic features of swarming. However, in conventional population level swarm assays dynamic events on the orders below mm/min cannot be detected. Hence, it is currently unknown if and how microscopic and rapid dynamics such as fingering are related to macroscopic scale dynamics of the phenomenon. Therefore, we next developed a Petri-dish based device which can allow a characterization of the fingering phenomenon while mimicking a conventional swarm assay where cells are attached to only one surface at a time (i.e., without the need for covering the cells with a microscope slide) (Fig. 4.2a; see Methods for detail).

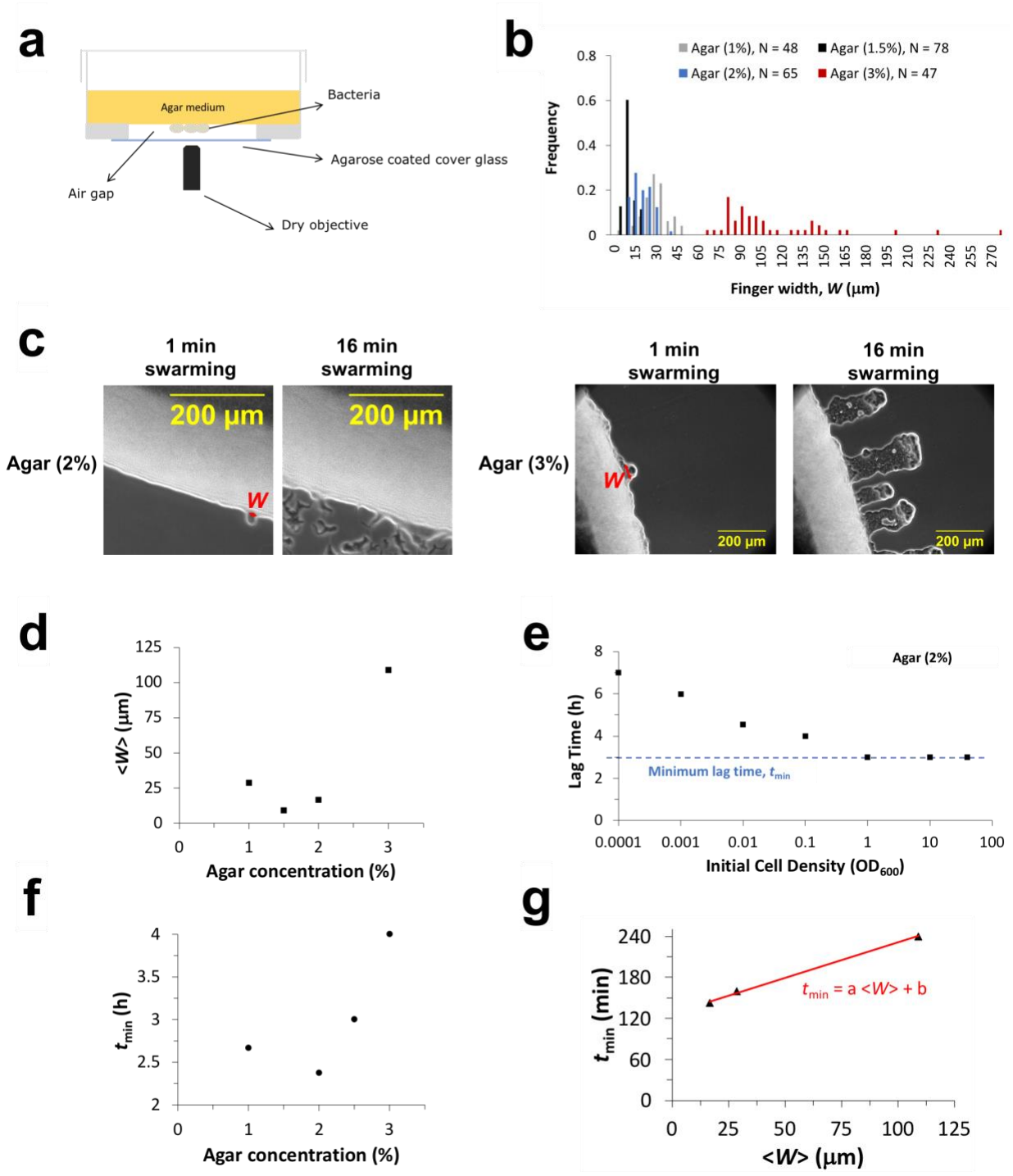

Figure 4. 2. A multiscale analysis of the onset of swarming.

a. Schematic illustration of the Petri dish-based device for visualizing dynamic properties of swarming. Not drawn to scale. **b.** Distributions of finger width at the onset of swarming for agar concentrations of 1% (grey), 1.5% (black), 2% (blue), and 3% (red). **c.** Representative phase contrast microscopic fields of view

of the original colony boundary 1 min and 16 min after the onset of swarming for 2% (left two) and 3% (right two) agar concentrations in LB medium. *W* is the finger width when a finger first leaves its original colony; defined in the direction tangential to the original colony boundary. A 20x dry objective was used. **d.** Mean finger width (<*W*>) was calculated from (b) and plotted as a function of agar concentration. **e.** The lag time prior to the onset of swarming on an LB agar (2%) surface by a *P. mirabilis* PM7002 colony as a function of its initial cell density. Note that lag time has a non-zero constant minimum value denoted as t_{min}. **f.** Minimum lag time (t_{min}) as a function of agar concentration. **g.** Minimum lag time (t_{min}) and mean finger width (<*W*>) were plotted against each other for the agar concentrations tested. The red line is a linear fit defined as $t_{min} = a\langle W\rangle + b$, where a = ~1.04 min/μm and b = ~128 min. R^2 for the fit is 0.9978.

As seen in Fig. 4.2c, swarming again initiated as fingers in this geometry of the assay suggesting that it does so in conventional swarm assays too. In order to demonstrate how our device can be used to investigate such a microscopic and short time scale phenomenon of swarming, we varied the concentration of agar in the medium and measured the width of these fingers at the time they first left their original colony (see Fig. 4.2b for finger width (*W*) distribution). Plotting the mean finger width (<*W*>) as a function of agar concentration revealed a non-monotonic dependence (Fig. 4.2d).

It is known from the conventional swarm assays that, for a given environment, the time to initiate range expansions observed at the population level linearly decreases with logarithmic increases in initial cell density until a non-zero minimum value (t_{min}) beyond which it no longer depends on the initial cell density (Fig. 4.2e) [237]. Determining the value of t_{min} for various agar concentrations yielded a non-monotonic relationship that is similar to the aforementioned relationship between <*W*> and agar concentration (compare Fig. 4.2d and Fig. 4.2f). If finger formation is required by a colony in order to overcome the motility barrier exerted on it by environment, a correlation between W and t_{min} is expected. Indeed, plotting <*W*> and t_{min} against each other yielded a linear correlation (Fig. 4.2g) demonstrating how our device and approach can

reveal simple relationships between microscopically and macroscopically observable features of the initiation of swarming.

4.3.3. *In situ* visualization of the motion of individual swarmer cells.

As illustrated by the fingering phenomenon discussed above, range expansions are performed by groups of cells. Therefore, it is natural to interrogate the interplay between the macroscopic dynamics of range expansions and individual swarmer cell motion. We here demonstrate that our Petri-dish based device developed in this study can also allow studying the motion of individual cells *in situ* as a population of bacteria swarms. We first constructed a high copy number plasmid that constitutively expresses GFP (pES02, see Methods for detail). Then, we labeled only a small fraction (~1%) of a cell population with this plasmid (yielding the strain AMK66) and recorded time-lapse fluorescence microscopy videos of actively expanding layers of cells at near real time resolution. Next, tracking the GFP-labeled cells in these time-lapse videos we characterized their motion. In Fig. 4.3a, we present our representative results obtained from a middle region of an actively expanding layer of cells between 35 min and 37 min after the onset of swarming (Fig. 4.3a). It is common to plot the mean square displacement (MSD) of a particle as a function of time elapsed in motion for comparing its motion with Brownian motion (diffusion) where MSD linearly increases with time. Hence, in order to compare the motion of individual cells tracked with Brownian motion, we plotted the logarithm of the MSDs of these cells as a function of the logarithm of time elapsed (Δt) in Fig. 4.3b.

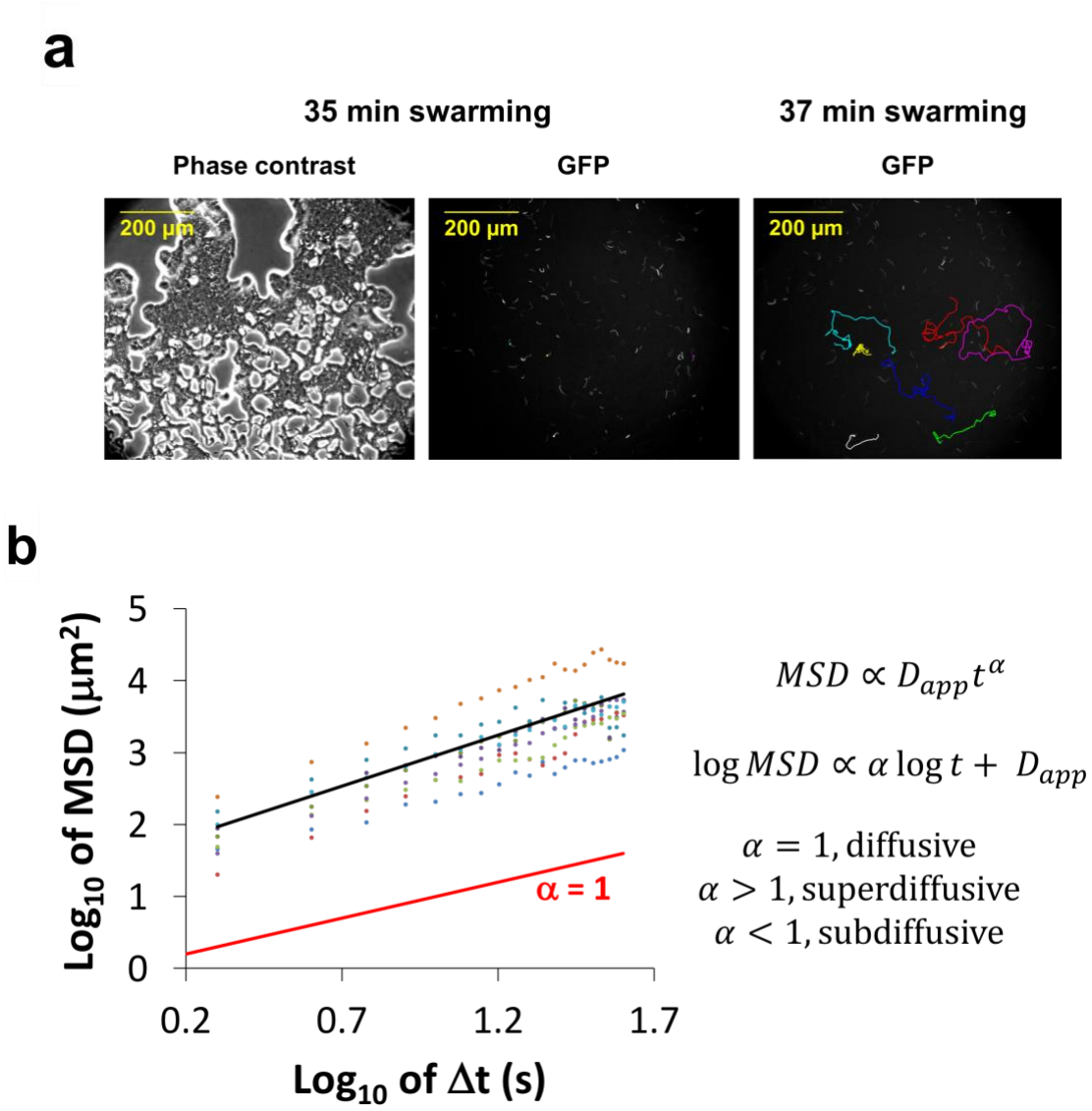

Figure 4. 3. *In situ* visualization of the motion of individual swarmer cells.

a. Phase contrast (left) and GFP (middle) images of a field of view whose center was away from the original boundary and the current leading edge of the colony by ~500 μm and ~700 μm, respectively, 35 min after the onset of swarming. Only ~ 1% of the cells harbored a plasmid enabling a constitutive expression of GFP (AMK66). *Right*. GFP image of the same field of view taken after 2 min. Trajectories of motions of individual GFP-labeled (AMK66) cells were tracked for the 2 min time elapsed and shown as colored lines. A 20x dry objective was used. GFP images were taken every two seconds. One second exposure time was used. **b.** Mean square displacements (MSD) were calculated from the trajectories shown in (a) and their logarithms were plotted against the logarithm of the time lag (Δt). Circles represent the data for ten different cells with ten different colors. The black line is a linear fit to the average motion of the ten cells with a slope (α) of ~1.42 and the y-intersect of ~1.55. Here, the y-intersect refers to an apparent diffusion coefficient (D_{app}). The red line illustrates $\alpha = 1$ which indicates a normal diffusive motion.

4.4. Discussion and Future Directions.

Here, we built two visualization tools for probing connections between microscopic and macroscopic features of swarming in *P. mirabilis* as a striking example of non-genetic phenotypic diversification during bacterial surface colonization.

We first constructed a green fluorescent protein reporter gene fusion to the *flhDC* operon which encodes the master regulator of motility. From this construct, basically, every time the promoter of *flhDC* is activated, mRNA containing both *flhDC* and *gfp* transcripts is made. And, since our *gfp* gene has its own ribosome binding site it will be separately translated. As a result, an increase in the intracellular GFP intensity will be correlated to an increase in the activity of *flhDC* promoter. Furthermore, since *flhDC* is positively autoregulated [240] an increase in this *flhDC* promoter driven-GFP levels can indirectly report on an increase in the levels of the transcription factor proteins encoded by the *flhDC* operon.

Using the *flhDC-gfp* fusion construct and a fluorescence microscope we were able to probe the spatiotemporal features of *flhDC* expression as a reporter of population diversification in a colony growing on a surface (Fig. 4.2c-d). We first showed that the *flhDC* operon promoter activity was at a minimum in a central region of a colony at the onset of swarming. Then, we showed that the deletion of a single gene (*rcsC*) made this central region' s *flhDC* promoter activity higher than nearly everywhere else (Fig. 4.2d and Fig. 4.2f).

Based on the previously published population averaged findings, RcsCDB phosphorelay is a well-known negative regulator of the *flhDC* operon [239, 252]. To our knowledge, our results are the

first to show the spatiotemporal pattern of the negative regulation of *flhDC* expression by RcsC. Our results indicate that in a WT population a central subpopulation suppresses swarmer cell differentiation in an RcsC-mediated manner.

In *E. coli*, based on population averaged results, it was previously shown that growth on an agar medium activates the Rcs phosphorelay in an RcsC dependent manner [254]. Rcs is mostly known in *E. coli* for being responsible for regulating the envelope composition of cells [254, 255]. Yet, physiological cues inducing the activation of Rcs phosphorelay, and its functional role in surface colonization have not been unraveled [256]. In addition to our aforementioned observations, since (*i*) cell growth on an agar surface would eventually lead to a nutrient limitation (unless nutrients are constantly replenished), and (*ii*) central regions of a colony would be where nutrients are the most limited, we hypothesize that Rcs displays a heterogeneous pattern of activity within a growing colony such that its activity is higher where the nutrient levels are lower. Once activated, it then represses *flhDC* expression. This would yield a microenvironment driven population diversification as previously reported for biofilms of other bacterial species [56-59]. The cells suppressing the expression of *flhDC* expression here may activate a long-term starvation survival mode.

However, the nutrient limitation driven-RcsC-mediated repression of *flhDC* expression at the colony interior we argue above cannot be the only mechanism responsible for generating the population heterogeneity observed as some cells do not exhibit any increase in *flhDC* expression in either the WT or Δ*rcsC* strains, even if they are located on frontal regions of a colony at the onset of swarming (Fig. 4.1d). Indeed, the positive feedback-activation of *flhDC* we reported

before [240] could eventually be responsible for this heterogeneity. It is well known that such positive feedback loops can yield a bistable gene expression when promoter activity is highly sensitive to changes in the regulatory protein levels; the cells that have somehow achieved a threshold level of the regulatory protein is quickly driven to a state with high gene expression. Such a hypersensitivity can be achieved via cooperative DNA binding of the regulatory proteins [70, 71], which is indeed the case for FlhD and FlhC proteins that together bind DNA as a hetero-hexameric complex, $FlhD_4C_2$ [244-246]. So, in this perspective, having GFP-OFF cells on the outer region of a colony would indicate that, due to some other regulatory inputs or stochastic factors beyond an RcsC-mediated repression, the threshold level of $FlhD_4C_2$ can only be attained in a fraction of the cells. Indeed, numerous other regulatory proteins have been identified for the *flhDC* operon (see [234] for a comprehensive review). Nonetheless, our ongoing work (data not shown) suggests that the *flhDC*-repressing activity of RcsC may indeed be driven by nutrient limitation. We are currently undertaking further research in order to directly probe a correlation between the spatiotemporal patterns of nutrient and RcsCBD phosphorelay activity levels within a colony growing on an agar surface.

Another tool we developed here is a Petri-dish based device which allows studying microscopic features of swarming while mimicking conventional swarm assay conditions where cells are attached to only one surface at a time (i.e., without the need for covering the colony with a microscope slide) (Fig. 4.2a; see Methods for detail). In order to demonstrate the use of this device for linking microscopic and macroscopic features of swarming, we characterized the dependence of the fingering phenomenon seen at the onset of swarming on agar concentration (Fig. 4.2c). Our preliminary results revealed that the mean finger width ($\langle W \rangle$) is linearly correlated with the

minimum lag time (t_{min}) observed before the onset of swarming (Fig. 4.2g). Fitting a linear function to this correlation yielded two parameters; a positive slope (a) and a positive y-intersect (b) (Fig. 4.2g, the red line and the equation). Here, b represents the value that t_{min} would take in case no finger formation is required for getting out of the original colony. For our preliminary set of data presented, b= ~128 min. Swarmer cell differentiation requires at least two major changes to the cells; hyper elongation (cell growth with no division) and high flagellation. Swarmer cells are typically 10-fold longer than normal cells, and their biomass doubling time is the same as normal cells (~20 min per doubling) [232]. Hence, it would take nearly 60 min in order for a cell to elongate to a typical swarmer cell length. In addition, the available literature suggests that it takes about 20 min for a bacterial cell to generate a typical flagellum [257]. Collectively, b= ~128 min can be explained to a large degree by consideration of only these two apparent changes to the cells before the onset of swarming. On the other hand, the value of a can tell the average time that is required for the formation of a finger of a unit micron. Our preliminary data suggests a = ~ 1 min/μm. Further research is needed to check on the universality of this relationship between mean finger width and minimum lag time to initiate swarming under various environmental parameters such as nutrient and agar concentrations.

As another demonstration of the use of the Petri-dish based device we developed here, in Fig. 4.3 we characterized the motion of individual swarmer cells in an actively expanding layer of cells during swarming. As a result, on a log-log scale, we plotted the mean square displacement (MSD) of the individual cells as a function of the time elapsed (Δt) (Fig. 4.3b). It is well-known for particles undergoing diffusion (Brownian motion) that MSD increases linearly with Δt, and the proportionality between them gives the diffusion coefficient of the particle with a pre-factor

depending on the dimensionality of the space in which the motion takes place [258]. More generally, MSD $\propto \Delta t^{\alpha}$, where $\alpha = 1$ represents diffusion, while $\alpha > 1$ ($\alpha < 1$) indicates a super (sub) diffusive motion. Our representative results here seem to yield $\alpha > 1$. Indeed, a previous study reported that two other species of bacteria perform a similar super diffusive motion during swarming [259]. However, in order to conclude that the motion of swarming *P. mirabilis* is indeed inherently super diffusive in our case, a larger set of data needs to be collected, and a more in-depth analysis of the data is needed. For example, we have not yet performed any proper control experiments and analyses in order to rule out an instrument driven drift as one source of the super diffusive-like trajectories we obtained. Moreover, a more careful consideration is needed for our precision in determining the positions of bacteria at a given time point. For example, a bacterium could move approximately 15 pixels (~ 5 μm) within the one second of illumination exposure time we employed here. In order to improve this precision, reducing the exposure time as much as possible and employing an automated way of tracking the bacteria would definitely be helpful. Eventually, it would be interesting to incorporate the nature of individual cell motion in the models attempting to explain the macroscopic dynamic features of swarming. For example, can knowing the nature of individual cell motion help one understand why *P. mirabilis* adopts a surface colonization strategy which involves periodic cycles between range expansions and cell multiplication?

4.5. Materials and Methods.

4.5.1. Construction of a *P. mirabilis* strain with a single chromosomal copy *flhDC-gfp* transcriptional fusion.

A *gfpmut3b* gene [166] was PCR amplified from the plasmid pES02 using the primers #342 and #343, respectively. These primers contained SmaI and XbaI sites. The resultant *gfpmut3b* gene fragment contained its own 5'-UTR and ribosome binding site but did not include a promoter. A previously constructed pLX7801 plasmid is a variant of the suicide vector pGP704 that contains a transcriptional fusion of the *E. coli lacZ* gene to an incomplete sequence of the *P. mirabilis flhDC* operon where the first three nucleotides are missing in the *flhD* gene open reading frame (denoted as *flhD*') [260]. pLX7801 and the *gfpmut3b* PCR product obtained above were digested by SmaI and XbaI enzymes. This caused excision of the *lacZ* gene from pLX7801. The remaining part of the vector was isolated via a DNA gel electrophoresis and then ligated to the SmaI-XbaI-digested *gfpmut3b* PCR product obtained above using the T4 DNA ligase (New England Bio Labs). *E. coli* CC118 λpir (EMK40) was then transformed via electroporation with the resultant plasmid (pES04) for maintenance yielding the strain EMK63. The existence of a *flhD'C-gfpmut3b* fusion was confirmed in pES04 by DNA sequencing. Via electroporation, *E. coli* Sm10 λpir (EMK39) was then transformed with pES04 isolated from EMK63. This yielded the strain EMK64. Finally, a bacterial conjugation was performed between *P. mirabilis* 7002 WT (AMK50) and EMK64 in order to insert the *flhDC-gfpmut3b* transcriptional fusion at the native site of the *flhDC* operon in the chromosome using a previously described protocol [240]. This yielded the strain AMK79. The integration of the construct into the chromosome of AMK79 was verified by a colony PCR reaction using primers #318 (which targets the promoter region of the *flhDC* operon) and #349 (which targets a middle region in the *gfpmut3b* gene).

4.5.2. A markerless in-frame deletion of the *rcsC* gene in the *P. mirabilis* strain with a single chromosomal copy *flhDC-gfp* transcriptional fusion.

A previously described protocol was used with slight modifications [241]. Briefly, an approximately 1,000 base pair-fragment containing the first two codons of the *rcsC* gene and upstream flanking DNA was generated by PCR (IFD1) using primers #403 and #404. A second fragment of 1,000 base pair-fragment containing the last three codons of the gene and downstream flanking DNA was generated by PCR (IFD2) using primers #405 and #406. Primers #404 and #405 were previously 5' phosphorylated using T4 Polynucleotide Kinase (ThermoFisher). IFD1 and IFD2 were then ligated, and the resultant ligate was PCR amplified using primers #403 and #406. This IFD1 + IFD2 PCR amplicon was then ligated into pBluescript SK(-) (Stratagene) pre-digested with SmaI yielding the plasmid pES07. For maintenance of pES07, *E. coli* DH5α (EMK45) was transformed with it by electroporation yielding the strain EMK72. The IFD1 + IFD2 fragment was then sub-cloned from pES07 to the suicide vector pKNG101 between the ApaI and BamHI sites yielding the plasmid pES08. pKNG101 is a suicide vector harboring streptomycin resistance, used to select for initial pKNG101 integration, and the *sacB* gene, which selects for the loss of pKNG101 in the presence of 10% sucrose [261]. *E. coli* CC118 λpir (EMK40) was then transformed via electroporation with pES08 for maintenance yielding the strain EMK74. Next, via electroporation, *E. coli* Sm10 λpir (EMK39) was transformed with pES08 isolated from EMK74. This yielded the strain EMK75. Finally, a bacterial conjugation was performed between *P. mirabilis* 7002 WT (AMK50) and EMK75 in order to obtain a single copy *flhDC-gfpmut3b* transcriptional fusion at the native site of the *flhDC* operon in the chromosome using a previously described protocol [240]. This yielded the strain AMK84. The in-frame deletion in the *rcsC* gene in the chromosome of AMK84 was verified via a colony PCR reaction using

primers #403 and #406 by observation of an expected decrease (~2800 base pairs) in the length of the product in comparison to the product obtained when a wild-type colony (AMK79) was used as template. Additionally, the absence of an *rcsC* gene in AMK84 was also verified by a colony PCR reaction using primers #422 and #423 which yielded a product of the expected size (2,739 bp) when an AMK79 colony was used as template, but not for AMK84 as the template. Primers #422 and #423 target the 57th bp from the beginning and the 34th bp from the end of the open reading frame of the *rcsC* gene, respectively.

4.5.3. Construction of a plasmid allowing a constitutive high expression of a green fluorescent protein gene.

An *rrnBT*-pTet-*gfpmut3b* fragment was amplified from NMK141 using primers #305 and #307, and then ligated to pBluescript SK(-) (Stratagene) digested with SmaI. *E. coli* DH5α (EMK45) was transformed with the resultant ligate by electroporation. This fragment has an *E. coli* transcription terminator site named *rrnBT* followed by a *tet* promoter and then a *gfpmut3b* gene which has a 5'-UTR region and a ribosome binding site. Hence, in the absence of Tet repressor proteins this construct should constitutively express GFP. pBluescript SK(-) has a *lacZ* gene with a constitutively active promoter. Therefore, when exposed to a blue/white screening, colonies with an intact copy of this plasmid will appear blue. However, its *lacZ* gene overlaps with its multiple cloning site (MCS) which also has the only SmaI site in the plasmid. Therefore, any variant of this plasmid carrying an insert at the SmaI site will have broken *lacZ* gene, and colonies of harboring such variants will appear white in a blue/white screening. Hence, several white colonies were analyzed utilizing restriction reactions for the existence of the plasmid carrying a *rrnBT*-pTet-*gfpmut3b* insert. The plasmid isolated from one such colony was verified by DNA sequencing and

then named pES02. Finally, *P. mirabilis* PM7002 (AMK50) was transformed with pES02 by electroporation yielding the strain AMK66.

4.5.4. Bacterial growth conditions.

The strains and plasmids used in this study are described in Table 4.1. All primers used were described in Table 4.2. All *P. mirabilis* strains were derived from a wild-type PM7002 strain (AMK50) which was originally received as a gift from Philip N. Rather (Emory University). Except where indicated, cell cultures were performed in Luria-Bertani (LB) broth at 37°C with shaking at 200 rpm. For all of our experiments, the night before the experiment cells taken from an 80°C stock in glycerol were grown to saturation. Then, a small volume from this overnight culture was inoculated in fresh antibiotic-free medium for an experimental culture such that its optical density at 600 nm (OD_{600}) would reach to the value of interest after going through at least five doublings. Conventional swarm assays were performed using 100 mm x 15 mm Petri dishes (Fisher Scientific). In all conventional swarm assays, 16 ml medium per 100 mm-dish was used. In all microscopic swarm assays, 2.5 ml medium per 35 mm-dish was used. This ensured approximately the same medium thickness in the dishes of these two different sizes.

Table 4. 1. Strains and plasmids used in Chapter 4.

Strain	Description/Genotype	Derived from	Comment	Reference
***P. mirabilis* strains**				
AMK50	Tc^R	-	PM7002 ATCC wild-type strain	Stock of Laboratory of Minsu Kim
AMK66	Tc^R	AMK50	Constitutive expression of GFP from the plasmid pES02	This study
AMK79	Tc^R *flhDC-gfpmut3b*, Amp^R	AMK50	Transcriptional fusion of the *gfpmut3b* gene the native *flhDC* operon	This study
AMK84	Tc^R *flhDC-gfpmut3b*, Amp^R Δ*rcsC*	AMK79	Transcriptional fusion of the *gfpmut3b* gene the native *flhDC* operon, Markerless Δ*rcsC* in-frame deletion mutation	This study
***E. coli* strains**				
EMK39	*thi thr leu tonA supE recA* RP4-2Tc::Mu Kan^r λ*pir*	-	SM10 λ*pir*	[262]
EMK40	*araD139* Δ*(ara leu)7697* Δ*lacZ74 phoA*Δ*20 galE galK thi rpsE rpoB argE(Am) recA1*	-	CC118 λ*pir*	[263]
EMK45	F- Φ80d*lacZ*ΔM15 Δ(*lacZYA-argF'*)U169 *endA1 recA1 hsdR17(*r_k- m_k-*)deoR thi-1 supE44* λ- *gyrA96 relA1*	-	DH5α	Stock of Laboratory of Minsu Kim
NMK141	Δ*motA*, pTet-gfp (intC), pCon-tetR-lacIq (attB)	-	*E. coli* NCM3722 mutant with pTet driving the expression of *gfpmut3b* at the *intC* locus, pCon driving the expression of *tetR* at the *attB* locus	Stock of Laboratory of Minsu Kim
Plasmids				
pBluescriptII SK(−)	ColE1 replicon *lacZα*; Chl^R	-	-	Stratagene
pKNG101	R6K replicon *mob*$^+$ *sacB*$^+$*R*$^+$; Sm^R	-	-	[261]
pLX7801	Amp^R	-	pGP704 + *flhD'C-lacZ*	[260]
pES02	ColE1 replicon *lacZα*; Chl^R	pBluescriptII SK(−)	pBluescriptII SK(−) + *rrnBT*-pTet-*gfpmut3b*	This study
pES04	Amp^R	pLX7801	pGP704- *flhD'C-gfpmut3b*	This study
pES07	ColE1 replicon *lacZα*; Chl^R	pBluescriptII SK(−)	pBluescriptII SK(−) + *rcsC* in-frame deletion fragment	This study
pES08	R6K replicon *mob*$^+$ *sacB*$^+$*R*$^+$; Sm^R	pKNG101	pKNG101 + Δ*rcsC* (in-frame deletion mutation)	This study

Table 4. 2. Primers used in Chapter 4.

Primer	Sequence (5' → 3')	Purpose
#305	TGCGAGAGTAGGGAACTGC	
#307	CCAAGTCTTTTATTTGTATAGTTCATCCATGCC	*rrnBT*-pTet-*gfpmut3b* amplification from NMK141
#318	TGGGTAGATTCGCTTATTAATTCTCAGC	
#342	ATAGCCCGGGTACTGAGCACATATGCAG	
#343	GCCGTCTAGAGGTTATTTGTATAGTTCATCCATGCC	*flhDC-gfpmut3b* transcriptional fusion
#403	CTCGTGGTCGTCCAATTATC	
#404	TCGCAAATAACCACCCTAA	
#405	GTGGCATAATCCAACGATT	
#406	ATCTCAGAGAGAACTGCGA	
#422	GCACTGGGTATCATGTTGTG	
#423	GCACTGGGTATCATGTTGTG	*rcsC* in-frame deletion

For strain construction, except noted otherwise, the plates were incubated at 37°C. *E. coli* strains were grown on LB with agar (1.5%), and *P. mirabilis* strains were grown on LB with 3.5% agar in order to prevent swarming. Antibiotic selections for *E. coli* were done at the following concentrations: 100 μg/ml ampicillin, 25 μg/ml kanamycin, 25 μg/ml streptomycin, and 25 μg/ml chloramphenicol. Antibiotic selections for *P. mirabilis* were performed at the following concentrations: 300 μg/ml ampicillin, 20 μg/ml kanamycin, 35 μg/ml streptomycin, 200 μg/ml chloramphenicol and 15 μg/ml tetracycline. When appropriate, for blue/white colony screening 5-bromo-4-chloro-3-indolyl-β-D-galactopyranoside (X-Gal), whose reaction with LacZ proteins yields a blue colored product, was used at final concentration of 20 μg/ml.

4.5.5. Strain and plasmid construction.

All PCR amplifications were done using the high-fidelity Phusion DNA polymerase (New England Bio Labs). All ligations were performed using the T4 DNA ligase (New England Bio Labs). All

enzymes used for restriction reactions were purchased from New England Bio Labs. In order to transform the cells with plasmids via electroporation, 8 ml of cells was grown to an OD_{600} of 0.3 to 0.5 in LB broth. The cells were pelleted by centrifugation at 3,500 rpm for 5 min at 4°C before being washed three times with 5 ml of ice-cold 10% glycerol and finally resuspended in 110 µl of ice-cold 10% glycerol per electroporation. Electroporations were performed in 1mm Eppendorf cuvettes with an Eppendorf Eporator electroporator. 900 µl of pre-warmed LB broth was immediately added to the transformed cells. The cells were then incubated at 37°C for one hour shaking at 200 rpm before being plated on LB agar plates containing appropriate selection antibiotics.

4.5.6. Microscope imaging and analysis.

The optical microscope used in this study was an inverted one with an automated mechanical XY stage and auto-focus. This microscope was controlled by the MetaMorph software (Molecular Devices) and housed in a microscope incubator (InVivo Scientific) which maintained the temperature of samples at 37°C during the experiments. As specified in the figure captions, a dry or an oil immersion was used to obtain phase-contrast and fluorescence images of cells. A FITC filter set (Olympus) was used to image green fluorescent protein signals. Images were captured using a Neo 5.5 sCMOS camera (Andor),manually analyzed and prepared for publication using ImageJ [98]. For cell tracking, a freely available plug-in ("*Manual Tracking"*) was used.

For the experiments yielding the data presented in Fig. 4.1d-f, a 3 µl aliquot from an exponentially growing culture of OD_{600}= 0.01 was spread onto a pre-warmed 35 mm glass-bottom Petri dish (InVitro Scientific). A pre-warmed ~2.5 ml pad of 0.2x LB containing agarose (1%) was gently

placed on top such that it would fully cover the bottom surface of the dish. The lid of the dish was closed and sealed with parafilm in order to prevent evaporation of water. The dish was then immediately moved to the microscope pre-warmed to 37°C.

For the experiments yielding the data presented in Fig. 4.2 and Fig. 4.3, experiments were started with a 4 µl aliquot in Petri dish based-devices developed in this study for a microscopic study of open-geometry samples. See below for detail.

4.5.7. Development of a Petri dish based-device for multiscale studies of swarming.

A not-to-scale schematic illustration was given in Fig. 4.2a. A 22 mm x 22 mm cover glass (with a thickness of 0.13 mm – 0.17 mm) was sterilized by ethanol and was coated with a flat agarose (in nanopore water) pad of thickness of 0.16 mm – 0.19 mm on one surface only. The agarose concentration used here was 2.5%. This agarose coated cover glass was stored at 4°C until it was used in an experiment. In the meantime, an 18 mm x 18 mm hole was drilled at the center of the bottom of a 35 mm Petri dish (Greiner). The cut edges of this hole were carefully sanded for leveling them with the both interior and exterior surfaces of the bottom of the dish. For sterilization, the dish was then soaked in pure ethanol for less than a minute and then rinsed thoroughly three times with autoclaved nano-pure water. The day before the experiment, an LB agar medium was solidified in a separate sterile 35-mm Petri dish with an intact bottom and stored at 4°C until 30 min before the experiment. 30 min prior to the experiment, this nutrient agar medium was carefully removed with the help of a spatula and placed into the aforementioned ethanol sterilized dish with a hole at its bottom. The lid of this dish was then closed and sealed with a piece of parafilm. The dish was flipped upside down, and 4 µl of cells was center inoculated on the agar medium through the hole at the bottom of the dish. Once the inoculum fully dried out and the cells settled at room

temperature, the hole in the dish was closed with the agarose coated cover glass described above. The cover glass was immediately and firmly sealed to the dish with the help of a Scotch tape. Finally, the dish was moved to the microscope pre-warmed to 37°C. Note that this design leaves about an ~0.5 mm air gap between the bacteria to be studied and the bottom agarose coated-cover glass. This allows mimicking the regular swarm assay conditions in a set up that is compatible with a long working distance objective microscope. Here coating the interior surface of the bottom cover glass was extremely essential as water condensation would be blocking the view otherwise.

Chapter 5: Summary and Outlook

Population diversification is a widespread adaptation mechanism to unfavorable environments [21, 22]. It is well known that an isogenic population of bacteria can exhibit phenotypic diversification which can in turn have significant effects on ecological dynamics of populations and species [51]. Non-genetic phenotypic diversification plays a critical role in the adaptation of populations through catastrophic environmental changes [52, 53] and promotes sustenance of microbial species [54, 55]. In this dissertation, I have studied the origins and implications of non-genetic phenotypic heterogeneity in bacteria under three prevalent unfavorable environments– nutrient fluctuations, antibiotic exposure, and surface association. My work consisted of experiments, quantitative modeling and development of visualization tools.

In the second chapter, we characterized the metabolic heterogeneity and its effect on phenotypic diversity in a clonal population of starved *E. coli* cells subjected to nutrient upshift. Our results revealed dynamic changes in phenotypic composition. We identified metabolic heterogeneity as a cellular variation driving such changes, and oxidative stress as a potential endogenous factor triggering such cellular variations.

Importantly, our findings provide a fresh metabolic perspective for dormancy. Dormant cells are resilient to a variety of environmental stresses, and hence can contribute to recovery of a microbial population after disturbance [52, 55]. Although it has been generally assumed that dormant cells are metabolically inactive [153], their metabolism has not been experimentally characterized in detail. To our knowledge, this dissertation is the first study characterizing the three major

metabolic activities in single dormant bacteria; substrate uptake, catabolism, and anabolism. Our results identify a metabolic state of dormant cells; dormant cells are metabolically partially active, exhibiting active substrate uptake and catabolism but inactive anabolism.

Furthermore, our results showed that oxidative stress induces dormancy through inactivation of anabolism. Aerobically growing cells constitutively produce reactive oxygen species such as hydrogen peroxide, superoxide anion radical, and highly reactive hydroxyl radicals mostly as a result of respiration through the use of molecular oxygen [264-266]. Hence, oxidative stress is a potential endogenous stress that most aerobic organisms may experience as a by-product of their respiratory activities, and thus could naturally contribute to the emergence of metabolic heterogeneity and dormancy.

The emergence of metabolic heterogeneity and diverse growth responses as a result of nutrient shifts in isogenic cell populations have been reported only in a few recent articles so far. For example, isogenic populations exhibited metabolic diversifications driving the constituent cells into either a growing or a non-growing phenotype following carbon source downshifts in *Lactococcus lactis* [267] and *E. coli* [117] bacteria. As a eukaryotic example, in an isogenic *Saccharomyces cerevisiae* yeast population, dynamic changes in carbon source (glucose) levels led to the emergence of a metabolic heterogeneity and an associated growth arrest in a subpopulation of cells [268]. Together with these, our findings are expected to constitute one of the few pioneering examples in the field.

Cells, just to stay viable, must take up and catabolize nutrients. This "maintenance requirement" arises due to the fact that it takes substrates and energy to repair the chemical wear and tear of cellular materials, maintain the membrane potential, and fulfill other non-growth-related functions [154, 155]. How dormant cells could meet this maintenance requirement was not clear with the previous assumption of inactive metabolism. Now, our findings of active substrate uptake and catabolism in dormant cells illustrate how this maintenance requirement could be satisfied. Importantly, our findings that active substrate uptake and catabolism in dormant bacteria may provide a potential target for antimicrobial treatments. It is generally believed that antimicrobial agents target crucial steps for cell growth. Dormant cells, because of their lack of growth, can persist in the face of these agents as described in chapter three [195, 224]. Antimicrobial agents inhibiting nutrient uptake and catabolic pathways may make it difficult for dormant cells to meet the maintenance requirement and cause the loss of viability, contributing to eradication of bacteria.

It was previously shown by Matthias Heinemann' s group that an isogenic *E. coli* population can form non/slow-growing antibiotic tolerant-persister cells following a nutrient downshift [117]. It is worth noting that, as a follow-up to this, while the corresponding work presented in this dissertation was being independently conducted, the same group later published results supporting our findings and conclusions regarding the emergence of metabolic heterogeneity, diverse growth responses and persistence as result of nutrient shifts: Persister cells generated as a result of nutrient downshifts have a low metabolic activity in general, and their proteomic characterization suggests an enhanced catabolism and lowered anabolism compared to normally growing cells [118]. It is crucial to note that our study extensively differs from this study regarding the research

methodology and more broadly reports on the dynamic changes in the phenotypic composition of a population and factors that can cause those changes.

In the third chapter, we quantitatively studied persistence, which is probably the most clinically relevant example of non-genetic phenotypic heterogeneity conferring a clonal bacterial population chances to evade an antibiotic treatment. Previous studies have found that persisters survive antibiotic treatment by virtue of staying in a non-growth (i.e., dormant) state during long periods of time (i.e., lag phase) [100-104]. While many genes that can alter the levels of persistence have been identified, there has been a substantial controversy regarding how these genes contribute to persistence [184-189]. As such, with the current knowledge of molecular mechanisms alone, we cannot predict the population dynamics of persistence, e.g., what percentage of cells in a population is persisters, and how their percentage changes over time. Here, quantitatively analyzing the lag phase of a previously starved *E. coli* cell population subjected to nutrient upshift, we found that the lag time distribution of persister cells is captured by a power-law decay with an exponent of nearly two.

A myriad of different molecular processes can contribute to generation and rejuvenation of persisters [104, 159, 195, 208-223]. Then, what would be the time distribution of cells exiting from the persistent state? A minimalist's approach would be to consider exiting from persistence as a random and independent (Poisson) event occurring at a constant rate. As we showed in chapter three in detail, the time distribution of a single Poisson event should follow an exponential decay. In the presence of a large number of distinct Poisson events, the event time distribution follows a power law decay with exponent of -2, agreeing very well with what we found experimentally.

Power law distribution is a widespread feature in many stochastic processes, observed in physics, microbiology, ecology, earth sciences and social sciences (e.g., self-organized criticality, earthquake, word usage, etc.) [201, 259, 269]. The most well-known examples of a power-law distribution reported for microbiological phenomena are the time distribution of switches in the rotational direction of bacterial flagellar motors in the presence of large fluctuations in the regulatory protein levels [270-272], typical organism size distributions in marine microbial communities [273], and waiting time distributions between the directional turns of single *Bacillus subtilis* and *Serretia marcescens* bacteria as they engage in a collective surface motion composed of alternating straight runs and turns [259]. In the latter example, the exponent of the power law time distribution was specifically measured as -2.5. Moreover, the distributions of slip displacements and durations in the stick-slip social motility of *Myxococcus xanthus* bacteria were shown to exhibit power-laws with exponents of -2.0 and -2.2, respectively [274]. Interestingly, a recent experimental ecology study also revealed power-law waiting time distributions with exponents ranging between -2 and -1 in the foraging activity of various marine predator animals [269]. Power-law distributions were also reported when fluctuations in many distinct processes such as voltage in a simple resistor, traffic flow, and human heartbeat were plotted against their frequency, and this is more generally known as $1/f$ noise [275, 276]. Overall, power-law distributions are ubiquitously found as a quantitative feature of fluctuations in nature, yet they may be underlain by different mechanisms for different phenomena. Our work here highlights the power of quantitative analysis for revealing some universal features of fluctuations at systems level and conferring a predictive power even without a detailed knowledge regarding the specific underlying mechanisms.

From a clinical point of view, a long tailed (power law decay in this case) probability distribution for exiting from dormancy (i.e., rejuvenation) is problematic, because it indicates that some persister cells can survive a very long period of antibiotic treatment, later rejuvenate and resume growth. Unfortunately, many conventional antibiotics have little efficacy for these cells during non-growth phase, killing them only once they rejuvenate. Indeed, previous analyses have suggested that bacterial populations as small as one or two cells can cause infections in human [277-280]. Also, it has been increasingly acknowledged that chronic diseases are underlain by poor eradication of infections, e.g., such as *Pseudomonas aeruginosa* in chronic cystic fibrosis [281], *Helicobacter pylori* in chronic gastric and duodenal ulcers [282], and *Mycobacterium tuberculosis* in chronic phthisis [283]. Therefore, for infections containing persister cells, a prolonged antibiotic treatment is required for eradication. This is why for infections by agents with a high number of persisters, e.g., *Mycobacterium tuberculosis*, antibiotic treatment lasts more than six months. It is also interesting to note that, it may be possible to draw some parallels between bacterial persistence and the persistence of human immunodeficiency virus (HIV) infections. Once established, HIV infection can be controlled by antiretroviral therapy (ART), which suppresses ongoing virus replication, but cannot be completely cured. This is believed to be due at least partly to formation of non-replicating reservoirs of viruses, against which ART is ineffective, which can later switch to a replicating state and relapse the infection after the drug therapy is stopped [284, 285]. In order to replicate, like any other virus, HIV needs to be in a replicating host cell, and hence HIV can remain latent inside long-living non-replicating cell types such as immune memory cells and neurons [285]. Then, later HIV can switch to a replicating state, promote and spread the infection via several different mechanisms identified such as activation of the host cell or being transferred to an active host cell through cell-to-cell contacts [285]. Hence, similar to bacterial persistence,

there can be multiple ways of entering into and exiting from a non-replicating state for HIV [285]. Therefore, it is curious to see if one would observe a power-law with an exponent close to -2, if the time distribution of HIV switching from a non-replicating state to a replicating state is characterized.

The heterogeneous Poisson events explanation that we offer for the power law-decay-lag time distribution may imply a resourceful survival strategy for a bacterial population. It would increase the chance of survival, without necessarily requiring any investment of resources on the communication between individuals, in uncertain environments by rare but long-awaited transitions to a growth state, instead of hedging all its bets to a single rate constant Poisson kinetics whose arrival time distribution would decay relatively more rapidly. This is indeed in agreement with the well-known "microbial scout hypothesis" and previously reported experimental results in support of it; the microbes that have survived an environmental assault are mostly in a non-growth (dormant) state, and they transition to a growth state at random over a long period of time [120, 286, 287].

Our findings in the second and the third chapters also raise a concern about the colony formation assay: one of the most frequently performed techniques in microbiological research since its invention in late the 1800s by Robert Koch [81]. Studies of microbial dynamics critically rely on this assay. In this assay, microbial samples are spread on a nutrient-rich agar plate, and then the number of colonies formed after overnight incubation is counted to determine the number of viable cells in the original samples. This assay assumes life and reproductive ability equal to each other and is routinely used to determine microbial soil contamination or the presence of pathogens in

drinking water. When environmental microbes are plated on nutrient-rich agar plates, a large number of cells fail to form colonies. This is known as “great plate count anomaly”, and it remains a long-standing puzzle why these cells do not form colonies - are they dead or dormant [121]? In fact, natural environments are scarce in nutrients, and microbes spend most of their lifetime starved in their natural habitats [2]. Previous studies have shown that starvation induces oxidative stress, and cells that accumulated high levels of oxidative stress were shown to not form colonies on nutrient-rich agar plates [145, 148, 288]. These studies assumed that for these cells the inability to form colonies was due to the loss of viability. We showed that non-growing cells with partial metabolic activities (which can be induced by oxidative stress) in chapter two and persister cells in chapter three can have long lag phases (tens of hours) when transferred to a nutrient-rich environment. This invokes a careful assessment of the reliability of the colony formation assay results in order to report the number of viable cells in a sample. Given that the lag time kinetics of bacteria is also an active research topic in various other fields such as food safety industry [289, 290], we believe that our findings can have broader implications.

In the fourth chapter, we developed two visualization tools with the aim of studying the origins and implications of non-genetic population diversification in the context of surface associated-life of bacteria. We chose to use *Proteus mirabilis* as a model organism, because it exhibits a remarkably rich phenomenon as it colonizes an agar surface; highly coordinated spatially and temporally periodic range expansions at the colony level associated with cellular differentiation events [229-231, 236]. Although an extensive literature exists regarding individual factors affecting these differentiation events, how they collectively exert their effects at the systems-level remains an open question. Also, how such cellular level events are related to the colony level

dynamics is unclear. With the hope of addressing these issues, we genetically constructed a reporter of cellular differentiation in cells and a Petri dish-based device allowing visualization of the phenomenon across a wide range of scales from the single cell (μm/s) to the colony level (cm/h). Preliminary experiments we ran using this experimental set-up suggest that nutrient gradient as a colony grows on an agar surface [59] may lead to the population diversification. Specifically, we believe that motility is induced by a mild nutrient limitation but repressed at locations where the nutrients are more severely limited. We are currently undertaking further research in order to thoroughly test this hypothesis.

Lastly, non-genetic phenotypic diversity can have significant effects on evolutionary dynamics and vice versa. For example, recent studies of experimental evolution showed that phenotypic diversity may evolve under fluctuating environments [160] and further accelerates evolutionary adaptation to various other environmental challenges [161, 162]. It would be insightful to test the universal applicability of our findings and ideas by characterizing different bacteria and types of environmental challenges.

References

1. Bar-On, Y.M., R. Phillips, and R. Milo, *The biomass distribution on Earth.* Proceedings of the National Academy of Sciences of the United States of America, 2018. **115**(25): p. 6506-6511.
2. Morita, R.Y., *Bacteria in Oligotrophic Environments: Starvation-survival Lifestyle*. illustrated ed. 1997: Chapman & Hall.
3. Baquero, F., J.-L. Martínez, and R. Cantón, *Antibiotics and antibiotic resistance in water environments.* Current Opinion in Biotechnology, 2008. **19**(3): p. 260-265.
4. Martínez, J.L., *Antibiotics and antibiotic resistance genes in natural environments.* Science, 2008. **321**(5887): p. 365-367.
5. Adler, J., *Chemotaxis in bacteria.* Science, 1966. **153**(3737): p. 708-716.
6. Stocker, R. and J.R. Seymour, *Ecology and Physics of Bacterial Chemotaxis in the Ocean.* 2012. **76**(4): p. 792-812.
7. Fenchel, T., *Microbial Behavior in a Heterogeneous World.* 2002. **296**(5570): p. 1068-1071.
8. Costerton, J.W., G.G. Geesey, and K.J. Cheng, *How bacteria stick.* Scientific American, 1978. **238**(1): p. 86-95.
9. Or, D., et al., *Physical constraints affecting bacterial habitats and activity in unsaturated porous media – a review.* Advances in Water Resources, 2007. **30**(6): p. 1505-1527.
10. Wang, G. and D. Or, *Aqueous films limit bacterial cell motility and colony expansion on partially saturated rough surfaces.* 2010. **12**(5): p. 1363-1373.

11. Tecon, R. and D. Or, *Bacterial flagellar motility on hydrated rough surfaces controlled by aqueous film thickness and connectedness.* Scientific Reports, 2016. **6**: p. 19409.

12. Dechesne, A., et al., *Hydration-controlled bacterial motility and dispersal on surfaces.* 2010. **107**(32): p. 14369-14372.

13. Hennes, M., et al., *Active depinning of bacterial droplets: The collective surfing of Bacillus subtilis.* 2017. **114**(23): p. 5958-5963.

14. Veldkamp, H., *The role of bacteria in energy flow and nutrient cycling*, in *Unifying concepts in ecology*, W.H. van Dobben and R.H. Lowe-McConnell, Editors. 1975, Springer Netherlands: Dordrecht. p. 44-49.

15. Whitman, W.B., D.C. Coleman, and W.J. Wiebe, *Prokaryotes: the unseen majority.* Proceedings of the National Academy of Sciences of the United States of America, 1998. **95**(12): p. 6578-6583.

16. Harmsen, H.J.M. and M.C. de Goffau, *The human gut microbiota.* Advances in Experimental Medicine and Biology, 2016. **902**: p. 95-108.

17. Sender, R., S. Fuchs, and R. Milo, *Revised estimates for the number of human and bacteria cells in the body.* PLoS Biology, 2016. **14**(8): p. e1002533.

18. Rosenberg, E. and I. Zilber-Rosenberg, *Microbes drive evolution of animals and plants: the hologenome concept.* mBio, 2016. **7**(2): p. e01395.

19. Costerton, J.W., P.S. Stewart, and E.P. Greenberg, *Bacterial biofilms: a common cause of persistent infections.* Science, 1999. **284**(5418): p. 1318-1322.

20. Parsonnet, J., *Bacterial infection as a cause of cancer.* Environmental Health Perspectives, 1995. **103 Suppl 8**: p. 263-268.

21. Wolf, D.M., V.V. Vazirani, and A.P. Arkin, *Diversity in times of adversity: probabilistic strategies in microbial survival games.* Journal of Theoretical Biology, 2005. **234**(2): p. 227-253.

22. Cordero, O.X. and M.F. Polz, *Explaining microbial genomic diversity in light of evolutionary ecology.* Nature Reviews. Microbiology, 2014. **12**(4): p. 263-273.

23. Nikolic, N., T. Barner, and M. Ackermann, *Analysis of fluorescent reporters indicates heterogeneity in glucose uptake and utilization in clonal bacterial populations.* BMC Microbiology, 2013. **13**: p. 258.

24. Nikolic, N., et al., *Cell-to-cell variation and specialization in sugar metabolism in clonal bacterial populations.* PLoS Genetics, 2017. **13**(12): p. e1007122.

25. Ackermann, M., *A functional perspective on phenotypic heterogeneity in microorganisms.* Nature Reviews. Microbiology, 2015. **13**(8): p. 497-508.

26. Rosenthal, A.Z., et al., *Metabolic interactions between dynamic bacterial subpopulations.* eLife, 2018. **7**.

27. Lowery, N.V., et al., *Division of Labor, Bet Hedging, and the Evolution of Mixed Biofilm Investment Strategies.* 2017. **8**(4): p. e00672-17.

28. Dragoš, A., et al., *Division of Labor during Biofilm Matrix Production.* Current biology : CB, 2018. **28**(12): p. 1903-1913.e5.

29. Zambrano, M.M., et al., *Microbial competition: Escherichia coli mutants that take over stationary phase cultures.* Science, 1993. **259**(5102): p. 1757-1760.

30. Finkel, S.E., *Long-term survival during stationary phase: evolution and the GASP phenotype.* Nature Reviews. Microbiology, 2006. **4**(2): p. 113-120.

31. Maharjan, R., et al., *Clonal adaptive radiation in a constant environment.* Science, 2006. **313**(5786): p. 514-517.

32. Acinas, S.G., et al., *Phenotypic and genetic diversification of Pseudanabaena spp. (cyanobacteria).* The ISME Journal, 2009. **3**(1): p. 31-46.

33. Mitri, S., E. Clarke, and K.R. Foster, *Resource limitation drives spatial organization in microbial groups.* The ISME Journal, 2016. **10**(6): p. 1471-1482.

34. Krismer, J., et al., *Single-cell mass spectrometry reveals the importance of genetic diversity and plasticity for phenotypic variation in nitrogen-limited Chlamydomonas.* The ISME Journal, 2017. **11**(4): p. 988-998.

35. Lenski, R.E., *Experimental evolution and the dynamics of adaptation and genome evolution in microbial populations.* The ISME Journal, 2017. **11**(10): p. 2181-2194.

36. Rendueles, O. and G.J. Velicer, *Evolution by flight and fight: diverse mechanisms of adaptation by actively motile microbes.* The ISME Journal, 2017. **11**(2): p. 555-568.

37. D'Costa, V.M., et al., *Sampling the antibiotic resistome.* Science, 2006. **311**(5759): p. 374-377.

38. Martinez, J.L. and F. Baquero, *Mutation frequencies and antibiotic resistance.* Antimicrobial Agents and Chemotherapy, 2000. **44**(7): p. 1771-1777.

39. McArthur, J.V., D.A. Kovacic, and M.H. Smith, *Genetic diversity in natural populations of a soil bacterium across a landscape gradient.* Proceedings of the National Academy of Sciences of the United States of America, 1988. **85**(24): p. 9621-9624.

40. Frankel, N.W., et al., *Adaptability of non-genetic diversity in bacterial chemotaxis.* eLife, 2014. **3**.

41. Kim, W., S.B. Levy, and K.R. Foster, *Rapid radiation in bacteria leads to a division of labour.* Nature Communications, 2016. **7**: p. 10508.

42. van Gestel, J., H. Vlamakis, and R. Kolter, *From Cell Differentiation to Cell Collectives: Bacillus subtilis Uses Division of Labor to Migrate.* PLOS Biology, 2015. **13**(4): p. e1002141.

43. Treves, D.S., S. Manning, and J. Adams, *Repeated evolution of an acetate-crossfeeding polymorphism in long-term populations of Escherichia coli.* Molecular Biology and Evolution, 1998. **15**(7): p. 789-797.

44. Lee, H.H., et al., *Bacterial charity work leads to population-wide resistance.* Nature, 2010. **467**: p. 82.

45. Boles, B.R. and P.K. Singh, *Endogenous oxidative stress produces diversity and adaptability in biofilm communities.* 2008. **105**(34): p. 12503-12508.

46. Boles, B.R., M. Thoendel, and P.K. Singh, *Self-generated diversity produces "insurance effects" in biofilm communities.* 2004. **101**(47): p. 16630-16635.

47. Maamar, H., A. Raj, and D. Dubnau, *Noise in gene expression determines cell fate in Bacillus subtilis.* Science, 2007. **317**(5837): p. 526-529.

48. Choi, P.J., et al., *A stochastic single-molecule event triggers phenotype switching of a bacterial cell.* Science, 2008. **322**(5900): p. 442-446.

49. Süel, G.M., et al., *Tunability and noise dependence in differentiation dynamics.* Science, 2007. **315**(5819): p. 1716-1719.

50. Balazsi, G., A. van Oudenaarden, and J.J. Collins, *Cellular decision making and biological noise: from microbes to mammals.* Cell, 2011. **144**(6): p. 910-25.

51. Ackermann, M., *Microbial individuality in the natural environment.* The ISME Journal, 2013. **7**(3): p. 465-467.

52. Kalamees, R. and M. Zobel, *THE ROLE OF THE SEED BANK IN GAP REGENERATION IN A CALCAREOUS GRASSLAND COMMUNITY.* Ecology, 2002.

53. van Boxtel, C., et al., *Taking chances and making mistakes: non-genetic phenotypic heterogeneity and its consequences for surviving in dynamic environments.* Journal of the Royal Society, Interface, 2017. **14**(132).

54. Chesson, P.L. and R.R. Warner, *Environmental Variability Promotes Coexistence in Lottery Competitive Systems.* The American Naturalist, 1981. **117**(6): p. 923-943.

55. Jones, S.E. and J.T. Lennon, *Dormancy contributes to the maintenance of microbial diversity.* Proceedings of the National Academy of Sciences of the United States of America, 2010. **107**(13): p. 5881-5886.

56. Xu, K.D., et al., *Spatial Physiological Heterogeneity inPseudomonas aeruginosa Biofilm Is Determined by Oxygen Availability.* 1998. **64**(10): p. 4035-4039.

57. Borriello, G., et al., *Oxygen Limitation Contributes to Antibiotic Tolerance of Pseudomonas aeruginosa in Biofilms.* 2004. **48**(7): p. 2659-2664.

58. Okabe, S., et al., *Analyses of Spatial Distributions of Sulfate-Reducing Bacteria and Their Activity in Aerobic Wastewater Biofilms.* 1999. **65**(11): p. 5107-5116.

59. Stewart, P.S. and M.J. Franklin, *Physiological heterogeneity in biofilms.* Nature Reviews Microbiology, 2008. **6**: p. 199.

60. Guptasarma, P., *Does replication-induced transcription regulate synthesis of the myriad low copy number proteins of Escherichia coli?* 1995. **17**(11): p. 987-997.

61. McAdams, H. and A. Arkin, *McAdams HH, Arkin A. It's a noisy business! Genetic regulation at the nanomolar scale. Trends Genet 15: 65-69*. Vol. 15. 1999. 65-9.

62. Becskei, A., B.B. Kaufmann, and A. van Oudenaarden, *Contributions of low molecule number and chromosomal positioning to stochastic gene expression.* Nature Genetics, 2005. **37**: p. 937.

63. Golding, I., et al., *Real-time kinetics of gene activity in individual bacteria.* Cell, 2005. **123**(6): p. 1025-1036.

64. Paulsson, J., *Models of stochastic gene expression.* Physics of life reviews, 2005. **2**(2): p. 157-175.

65. Elowitz, M.B., et al., *Stochastic gene expression in a single cell.* Science, 2002. **297**(5584): p. 1183-1186.

66. McAdams, H.H. and A. Arkin, *Stochastic mechanisms in gene expression.* 1997. **94**(3): p. 814-819.

67. Chung, J.D., et al., *Gene expression in single cells of Bacillus subtilis: evidence that a threshold mechanism controls the initiation of sporulation.* Journal of Bacteriology, 1994. **176**(7): p. 1977-1984.

68. Thattai, M. and A. van Oudenaarden, *Stochastic Gene Expression in Fluctuating Environments.* 2004. **167**(1): p. 523-530.

69. Kaern, M., et al., *Stochasticity in gene expression: from theories to phenotypes.* Nature Reviews. Genetics, 2005. **6**(6): p. 451-464.

70. Dubnau, D. and R. Losick, *Bistability in bacteria.* Molecular Microbiology, 2006. **61**(3): p. 564-572.

71. Mitrophanov, A.Y. and E.A. Groisman, *Positive feedback in cellular control systems.* Bioessays: News and Reviews in Molecular, Cellular and Developmental Biology, 2008. **30**(6): p. 542-555.

72. Norman, T.M., et al., *Stochastic switching of cell fate in microbes.* Annual Review of Microbiology, 2015. **69**: p. 381-403.

73. Hasty, J., et al., *Noise-based switches and amplifiers for gene expression.* Proceedings of the National Academy of Sciences of the United States of America, 2000. **97**(5): p. 2075-2080.

74. Acar, M., J.T. Mettetal, and A. van Oudenaarden, *Stochastic switching as a survival strategy in fluctuating environments.* Nature Genetics, 2008. **40**: p. 471.

75. Huh, D. and J. Paulsson, *Non-genetic heterogeneity from stochastic partitioning at cell division.* Nature Genetics, 2011. **43**(2): p. 95-100.

76. Huh, D. and J. Paulsson, *Random partitioning of molecules at cell division.* Proceedings of the National Academy of Sciences of the United States of America, 2011. **108**(36): p. 15004-15009.

77. Bergmiller, T., et al., *Biased partitioning of the multidrug efflux pump AcrAB-TolC underlies long-lived phenotypic heterogeneity.* Science, 2017. **356**(6335): p. 311-315.

78. Barrett, T.C., W.W.K. Mok, and M.P. Brynildsen, *Biased inheritance protects older bacteria from harm.* 2017. **356**(6335): p. 247-248.

79. Huang, K.C., *Applications of imaging for bacterial systems biology.* Current Opinion in Microbiology, 2015. **27**: p. 114-120.

80. Taheri-Araghi, S., et al., *Single-Cell Physiology.* Annual review of biophysics, 2015. **44**: p. 123-142.

81. Koch, R., *Die Aetiologie der Tuberculose.* Berliner Klinische Wochenschrift, 1882. **15**.

82. Wouters, J.A., et al., *Cold shock proteins and low-temperature response of Streptococcus thermophilus CNRZ302.* Applied and Environmental Microbiology, 1999. **65**(10): p. 4436-4442.

83. Sleight, S.C., N.S. Wigginton, and R.E. Lenski, *Increased susceptibility to repeated freeze-thaw cycles in Escherichia coli following long-term evolution in a benign environment.* BMC Evolutionary Biology, 2006. **6**: p. 104.

84. Phaiboun, A., et al., *Survival kinetics of starving bacteria is biphasic and density-dependent.* PLoS Computational Biology, 2015. **11**(4): p. e1004198.

85. Wiuff, C., et al., *Phenotypic tolerance: antibiotic enrichment of noninherited resistance in bacterial populations.* Antimicrobial Agents and Chemotherapy, 2005. **49**(4): p. 1483-1494.

86. Lennon, J.T. and S.E. Jones, *Microbial seed banks: the ecological and evolutionary implications of dormancy.* Nature Reviews. Microbiology, 2011. **9**(2): p. 119-130.

87. Loferer-Krössbacher, M., J. Klima, and R. Psenner, *Determination of bacterial cell dry mass by transmission electron microscopy and densitometric image analysis.* Applied and environmental microbiology, 1998. **64**(2): p. 688-694.

88. Liu, P.Y., et al., *Real-time Measurement of Single Bacterium's Refractive Index Using Optofluidic Immersion Refractometry.* Procedia Engineering, 2014. **87**: p. 356-359.

89. Zernike, F., *How I Discovered Phase Contrast.* Science, 1955. **121**(3141): p. 345-349.

90. Rodriguez, G.G., et al., *Use of a fluorescent redox probe for direct visualization of actively respiring bacteria.* 1992. **58**(6): p. 1801-1808.

91. Yoshioka, K., et al., *A novel fluorescent derivative of glucose applicable to the assessment of glucose uptake activity of Escherichia coli.* Biochimica et Biophysica Acta (BBA) - General Subjects, 1996. **1289**(1): p. 5-9.

92. Zhang, J., et al., *Creating new fluorescent probes for cell biology.* Nature Reviews Molecular Cell Biology, 2002. **3**: p. 906.

93. Albano, C.R., et al., *Quantitative measurement of green fluorescent protein expression.* 1996. **10**(12): p. 953-958.

94. Neidhardt, F., Ingraham, J. and Schaechter, M. , *Physiology of the bacterial cell: A molecular approach*. 1 ed. 1990, Sunderland (Mass.): Sinauer.: Sinauer Associates, Incorporated.

95. de Jong, H. and J. Geiselmann. *Fluorescent Reporter Genes and the Analysis of Bacterial Regulatory Networks*. 2015. Cham: Springer International Publishing.

96. Lutz, R. and H. Bujard, *Independent and tight regulation of transcriptional units in Escherichia coli via the LacR/O, the TetR/O and AraC/I1-I2 regulatory elements.* Nucleic Acids Research, 1997. **25**(6): p. 1203-1210.

97. Shaner, N.C., G.H. Patterson, and M.W. Davidson, *Advances in fluorescent protein technology.* 2007. **120**(24): p. 4247-4260.

98. Schneider, C.A., W.S. Rasband, and K.W. Eliceiri, *NIH Image to ImageJ: 25 years of image analysis.* Nature Methods, 2012. **9**(7): p. 671-675.

99. Jong, H.d., *Modeling and Simulation of Genetic Regulatory Systems: A Literature Review.* 2002. **9**(1): p. 67-103.

100. Jõers, A., N. Kaldalu, and T. Tenson, *The frequency of persisters in Escherichia coli reflects the kinetics of awakening from dormancy.* Journal of Bacteriology, 2010. **192**(13): p. 3379-3384.

101. Shah, D., et al., *Persisters: a distinct physiological state of E. coli.* BMC Microbiology, 2006. **6**: p. 53.

102. Kim, J.-S. and T.K. Wood, *Persistent Persister Misperceptions.* Frontiers in microbiology, 2016. **7**: p. 2134.

103. Roostalu, J., et al., *Cell division in Escherichia coli cultures monitored at single cell resolution.* BMC Microbiology, 2008. **8**: p. 68.

104. Balaban, N.Q., et al., *Bacterial persistence as a phenotypic switch.* Science, 2004. **305**(5690): p. 1622-1625.

105. Guantes, R., et al., *Transcription factor levels enable metabolic diversification of single cells of environmental bacteria.* The ISME Journal, 2016. **10**(5): p. 1122-1133.

106. Jõers, A. and T. Tenson, *Growth resumption from stationary phase reveals memory in Escherichia coli cultures.* Scientific reports, 2016. **6**: p. 24055.

107. Kuchina, A., et al., *Temporal competition between differentiation programs determines cell fate choice.* Molecular Systems Biology, 2011. **7**: p. 557.

108. Sheik, A.R., et al., *In situ phenotypic heterogeneity among single cells of the filamentous bacterium Candidatus Microthrix parvicella.* The ISME Journal, 2016. **10**(5): p. 1274-1279.

109. Bartumeus, F., et al., *Foraging success under uncertainty: search tradeoffs and optimal space use.* Ecology Letters, 2016. **19**(11): p. 1299-1313.

110. Venturelli, O.S., et al., *Population diversification in a yeast metabolic program promotes anticipation of environmental shifts.* PLoS Biology, 2015. **13**(1): p. e1002042.

111. Belete, M.K. and G. Balázsi, *Optimality and adaptation of phenotypically switching cells in fluctuating environments.* Physical Review. E, Statistical, Nonlinear, and Soft Matter Physics, 2015. **92**(6): p. 062716.

112. De Martino, M., et al., *Single-Cell Analysis of the Dps Response to Oxidative Stress.* Journal of Bacteriology, 2016. **198**(11): p. 1662-1674.

113. Silander, O.K., et al., *A genome-wide analysis of promoter-mediated phenotypic noise in Escherichia coli.* PLoS Genetics, 2012. **8**(1): p. e1002443.

114. Taniguchi, Y., et al., *Quantifying E. coli proteome and transcriptome with single-molecule sensitivity in single cells.* Science, 2010. **329**(5991): p. 533-538.

115. Labhsetwar, P., et al., *Heterogeneity in protein expression induces metabolic variability in a modeled Escherichia coli population.* Proceedings of the National Academy of Sciences of the United States of America, 2013. **110**(34): p. 14006-14011.

116. Kiviet, D.J., et al., *Stochasticity of metabolism and growth at the single-cell level.* Nature, 2014. **514**(7522): p. 376-379.

117. Kotte, O., et al., *Phenotypic bistability in Escherichia coli's central carbon metabolism.* Molecular Systems Biology, 2014. **10**: p. 736.

118. Radzikowski, J.L., et al., *Bacterial persistence is an active σS stress response to metabolic flux limitation.* Molecular Systems Biology, 2016. **12**(9): p. 882.

119. Schreiber, F., et al., *Phenotypic heterogeneity driven by nutrient limitation promotes growth in fluctuating environments.* Nature microbiology, 2016. **1**(6): p. 16055.

120. Epstein, S.S., *Microbial awakenings.* Nature, 2009. **457**(7233): p. 1083.

121. Staley, J.T. and A. Konopka, *Measurement of in situ activities of nonphotosynthetic microorganisms in aquatic and terrestrial habitats.* Annual Review of Microbiology, 1985. **39**: p. 321-346.

122. Bogosian, G. and E.V. Bourneuf, *A matter of bacterial life and death.* EMBO Reports, 2001. **2**(9): p. 770-774.

123. Li, L., et al., *The importance of the viable but non-culturable state in human bacterial pathogens.* Frontiers in microbiology, 2014. **5**: p. 258.

124. Nyström, T., *Nonculturable bacteria: programmed survival forms or cells at death's door?* Bioessays: News and Reviews in Molecular, Cellular and Developmental Biology, 2003. **25**(3): p. 204-211.

125. Csonka, L.N., et al., *The accumulation of glutamate is necessary for optimal growth of Salmonella typhimurium in media of high osmolality but not induction of the proU operon.* Journal of Bacteriology, 1994. **176**(20): p. 6324-6333.

126. Blainey, P., M. Krzywinski, and N. Altman, *Points of significance: replication.* Nature Methods, 2014. **11**(9): p. 879-880.

127. Yoshioka, K., et al., *Intracellular fate of 2-NBDG, a fluorescent probe for glucose uptake activity, in Escherichia coli cells.* Bioscience, Biotechnology, and Biochemistry, 1996. **60**(11): p. 1899-1901.

128. Natarajan, A. and F. Srienc, *Dynamics of glucose uptake by single Escherichia coli cells.* Metabolic Engineering, 1999. **1**(4): p. 320-333.

129. Tao, J., et al., *Transport of a Fluorescent Analogue of Glucose (2-NBDG) versus Radiolabeled Sugars by Rumen Bacteria and Escherichia coli.* Biochemistry, 2016. **55**(18): p. 2578-2589.

130. Wang, P., et al., *Robust growth of Escherichia coli.* Current Biology, 2010. **20**(12): p. 1099-1103.

131. Jahreis, K., et al., *Ins and outs of glucose transport systems in eubacteria.* FEMS Microbiology Reviews, 2008. **32**(6): p. 891-907.

132. Houser, J.R., et al., *Controlled Measurement and Comparative Analysis of Cellular Components in E. coli Reveals Broad Regulatory Changes in Response to Glucose Starvation.* PLoS Computational Biology, 2015. **11**(8): p. e1004400.

133. Preiss, J., *Bacterial glycogen synthesis and its regulation.* Annual Review of Microbiology, 1984. **38**: p. 419-458.

134. Iyer, S., B.R. Park, and M. Kim, *Absolute quantitative measurement of transcriptional kinetic parameters in vivo.* Nucleic Acids Research, 2016. **44**(18): p. e142.

135. Gefen, O., et al., *Direct observation of single stationary-phase bacteria reveals a surprisingly long period of constant protein production activity.* Proceedings of the National Academy of Sciences of the United States of America, 2014. **111**(1): p. 556-561.

136. López-Amorós, R., J. Comas, and J. Vives-Rego, *Flow cytometric assessment of Escherichia coli and Salmonella typhimurium starvation-survival in seawater using rhodamine 123, propidium iodide, and oxonol.* Applied and Environmental Microbiology, 1995. **61**(7): p. 2521-2526.

137. Comas, J. and J. Vives-Rego, *Assessment of the effects of gramicidin, formaldehyde, and surfactants on Escherichia coli by flow cytometry using nucleic acid and membrane potential dyes.* Cytometry, 1997. **29**(1): p. 58-64.

138. Boulos, L., et al., *LIVE/DEAD BacLight : application of a new rapid staining method for direct enumeration of viable and total bacteria in drinking water.* Journal of Microbiological Methods, 1999. **37**(1): p. 77-86.

139. Sträuber, H. and S. Müller, *Viability states of bacteria--specific mechanisms of selected probes.* Cytometry. Part A: the Journal of the International Society for Analytical Cytology, 2010. **77**(7): p. 623-634.

140. Waring, M.J., *Complex formation between ethidium bromide and nucleic acids.* Journal of Molecular Biology, 1965. **13**(1): p. 269-282.

141. Suzuki, T., et al., *DNA staining for fluorescence and laser confocal microscopy.* The Journal of Histochemistry and Cytochemistry, 1997. **45**(1): p. 49-53.

142. Banerjee, A., et al., *The DNA intercalators ethidium bromide and propidium iodide also bind to core histones.* FEBS open bio, 2014. **4**: p. 251-259.

143. Yao, Z., D. Kahne, and R. Kishony, *Distinct single-cell morphological dynamics under beta-lactam antibiotics.* Molecular Cell, 2012. **48**(5): p. 705-712.

144. Tuomanen, E., et al., *The rate of killing of Escherichia coli by beta-lactam antibiotics is strictly proportional to the rate of bacterial growth.* Journal of general microbiology, 1986. **132**(5): p. 1297-1304.

145. Dukan, S. and T. Nyström, *Bacterial senescence: stasis results in increased and differential oxidation of cytoplasmic proteins leading to developmental induction of the heat shock regulon.* Genes & Development, 1998. **12**(21): p. 3431-3441.

146. Gonidakis, S., S.E. Finkel, and V.D. Longo, *Genome-wide screen identifies Escherichia coli TCA-cycle-related mutants with extended chronological lifespan dependent on*

acetate metabolism and the hypoxia-inducible transcription factor ArcA. Aging Cell, 2010. **9**(5): p. 868-881.

147. Kram, K.E. and S.E. Finkel, *Culture volume and vessel affect long-term survival, mutation frequency, and oxidative stress of Escherichia coli.* Applied and Environmental Microbiology, 2014. **80**(5): p. 1732-1738.

148. Ballesteros, M., et al., *Bacterial senescence: protein oxidation in non-proliferating cells is dictated by the accuracy of the ribosomes.* The EMBO Journal, 2001. **20**(18): p. 5280-5289.

149. Hassan, H.M. and I. Fridovich, *Enzymatic defenses against the toxicity of oxygen and of streptonigrin in Escherichia coli.* Journal of Bacteriology, 1977. **129**(3): p. 1574-1583.

150. Imlay, J.A., *The molecular mechanisms and physiological consequences of oxidative stress: lessons from a model bacterium.* Nature Reviews. Microbiology, 2013. **11**(7): p. 443-454.

151. Keele, B.B., J.M. McCord, and I. Fridovich, *Superoxide dismutase from escherichia coli B. A new manganese-containing enzyme.* The Journal of Biological Chemistry, 1970. **245**(22): p. 6176-6181.

152. Yost, F.J. and I. Fridovich, *An iron-containing superoxide dismutase from Escherichia coli.* The Journal of Biological Chemistry, 1973. **248**(14): p. 4905-4908.

153. Ayrapetyan, M., T.C. Williams, and J.D. Oliver, *Bridging the gap between viable but non-culturable and antibiotic persistent bacteria.* Trends in Microbiology, 2015. **23**(1): p. 7-13.

154. Tempest, D.W. and O.M. Neijssel, *The status of YATP and maintenance energy as biologically interpretable phenomena.* Annual Review of Microbiology, 1984. **38**: p. 459-486.

155. van Bodegom, P., *Microbial maintenance: a critical review on its quantification.* Microbial Ecology, 2007. **53**(4): p. 513-523.

156. Chiang, S.M. and H.E. Schellhorn, *Regulators of oxidative stress response genes in Escherichia coli and their functional conservation in bacteria.* Archives of Biochemistry and Biophysics, 2012. **525**(2): p. 161-169.

157. Demple, B., *Regulation of bacterial oxidative stress genes.* Annual Review of Genetics, 1991. **25**: p. 315-337.

158. Wu, Y., et al., *Role of oxidative stress in persister tolerance.* Antimicrobial Agents and Chemotherapy, 2012. **56**(9): p. 4922-4926.

159. Vega, N.M., et al., *Signaling-mediated bacterial persister formation.* Nature Chemical Biology, 2012. **8**(5): p. 431-433.

160. Beaumont, H.J.E., et al., *Experimental evolution of bet hedging.* Nature, 2009. **462**(7269): p. 90-93.

161. Bódi, Z., et al., *Phenotypic heterogeneity promotes adaptive evolution.* PLoS Biology, 2017. **15**(5): p. e2000644.

162. González, C., et al., *Stress-response balance drives the evolution of a network module and its host genome.* Molecular Systems Biology, 2015. **11**(8): p. 827.

163. Brown, S.D. and S. Jun, *Complete Genome Sequence of Escherichia coli NCM3722.* Genome announcements, 2015. **3**(4).

164. Lyons, E., et al., *Using genomic sequencing for classical genetics in E. coli K12.* Plos One, 2011. **6**(2): p. e16717.

165. Soupene, E., et al., *Physiological studies of Escherichia coli strain MG1655: growth defects and apparent cross-regulation of gene expression.* Journal of Bacteriology, 2003. **185**(18): p. 5611-5626.

166. Kim, M., et al., *Need-based activation of ammonium uptake in Escherichia coli.* Molecular Systems Biology, 2012. **8**: p. 616.

167. Datsenko, K.A. and B.L. Wanner, *One-step inactivation of chromosomal genes in Escherichia coli K-12 using PCR products.* Proceedings of the National Academy of Sciences of the United States of America, 2000. **97**(12): p. 6640-6645.

168. Baba, T., et al., *Construction of Escherichia coli K-12 in-frame, single-gene knockout mutants: the Keio collection.* Molecular Systems Biology, 2006. **2**: p. 2006.0008.

169. Thomason, L.C., N. Costantino, and D.L. Court, *E. coli genome manipulation by P1 transduction.* Current Protocols in Molecular Biology, 2007. **Chapter 1**: p. Unit 1.17.

170. Brown, O.R., et al., *Dihydroxy-acid dehydratase, a [4Fe-4S] cluster-containing enzyme in Escherichia coli: effects of intracellular superoxide dismutase on its inactivation by oxidant stress.* Archives of Biochemistry and Biophysics, 1995. **319**(1): p. 10-22.

171. Benov, L. and I. Fridovich, *Why superoxide imposes an aromatic amino acid auxotrophy on Escherichia coli. The transketolase connection.* The Journal of Biological Chemistry, 1999. **274**(7): p. 4202-4206.

172. Ducret, A., E.M. Quardokus, and Y.V. Brun, *MicrobeJ, a tool for high throughput bacterial cell detection and quantitative analysis.* Nature microbiology, 2016. **1**(7): p. 16077.

173. Nicholson, A. and Y.-D. Wong, *Are accidents poisson distributed? A statistical test.* Accident Analysis & Prevention, 1993. **25**(1): p. 91-97.

174. Huestis, S.P., *Understanding the Origin and Meaning of the Radioactive Decay Equation* Journal of Geoscience Education,, 2002. **50**: p. 524-527.

175. Thattai, M. and A. van Oudenaarden, *Intrinsic noise in gene regulatory networks.* 2001. **98**(15): p. 8614-8619.

176. Jones, D.L., R.C. Brewster, and R. Phillips, *Promoter architecture dictates cell-to-cell variability in gene expression.* Science, 2014. **346**(6216): p. 1533-1536.

177. Sigal, A., et al., *Variability and memory of protein levels in human cells.* Nature, 2006. **444**(7119): p. 643-646.

178. Sepúlveda, L.A., et al., *Measurement of gene regulation in individual cells reveals rapid switching between promoter states.* Science, 2016. **351**(6278): p. 1218-1222.

179. Austin, D.W., et al., *Gene network shaping of inherent noise spectra.* Nature, 2006. **439**(7076): p. 608-611.

180. Brauner, A., et al., *An Experimental Framework for Quantifying Bacterial Tolerance.* Biophysical Journal, 2017. **112**(12): p. 2664-2671.

181. Lewis, K., *Persister Cells,* in *Annual Review of Microbiology, Vol 64, 2010*, S. Gottesman and C.S. Harwood, Editors. 2010, Annual Reviews: Palo Alto. p. 357-372.

182. Gerdes, K. and E. Maisonneuve, *Bacterial persistence and toxin-antitoxin loci.* Annu Rev Microbiol, 2012. **66**: p. 103-23.

183. Bigger, J., *TREATMENT OF STAPHYLOCOCCAL INFECTIONS WITH PENICILLIN BY INTERMITTENT STERILISATION.* The Lancet, 1944. **244**(6320): p. 497-500.

184. Shan, Y., et al., *Genetic Basis of Persister Tolerance to Aminoglycosides in Escherichia coli.* mBio, 2015. **6**(2).

185. Osbourne, D.O., et al., *Polyphosphate, cyclic AMP, guanosine tetraphosphate, and c-di-GMP reduce in vitro Lon activity.* Bioengineered, 2014. **5**(4): p. 264-268.

186. Ramisetty, B.C.M., et al., *What Is the Link between Stringent Response, Endoribonuclease Encoding Type II Toxin–Antitoxin Systems and Persistence?* Frontiers in Microbiology, 2016. **7**(1882).

187. Kim, J.-S. and T.K. Wood, *Tolerant, Growing Cells from Nutrient Shifts Are Not Persister Cells.* mBio, 2017. **8**(2): p. e00354-17.

188. Harms, A., et al., *Prophages and Growth Dynamics Confound Experimental Results with Antibiotic-Tolerant Persister Cells.* mBio, 2017. **8**(6): p. e01964-17.

189. Orman, M.A. and M.P. Brynildsen, *Dormancy is not necessary or sufficient for bacterial persistence.* Antimicrobial Agents and Chemotherapy, 2013. **57**(7): p. 3230-3239.

190. Patra, P. and S. Klumpp, *Population dynamics of bacterial persistence.* Plos One, 2013. **8**(5): p. e62814.

191. Levin, B.R. and K.I. Udekwu, *Population dynamics of antibiotic treatment: a mathematical model and hypotheses for time-kill and continuous-culture experiments.* Antimicrobial Agents and Chemotherapy, 2010. **54**(8): p. 3414-3426.

192. Carvalho, G., et al., *Relating switching rates between normal and persister cells to substrate and antibiotic concentrations: a mathematical modelling approach supported by experiments.* Microbial biotechnology, 2017. **10**(6): p. 1616-1627.

193. Allen, R.J. and B. Waclaw, *Bacterial growth: a statistical physicist's guide.* Reports on Progress in Physics, 2018. **82**(1): p. 016601.

194. Vulin, C., et al., *Prolonged bacterial lag time results in small colony variants that represent a sub-population of persisters.* Nature Communications, 2018. **9**(1): p. 4074.

195. Lewis, K., *Persister Cells.* 2010. **64**(1): p. 357-372.

196. Luidalepp, H., et al., *Age of inoculum strongly influences persister frequency and can mask effects of mutations implicated in altered persistence.* Journal of Bacteriology, 2011. **193**(14): p. 3598-3605.

197. Orman, M.A. and M.P. Brynildsen, *Inhibition of stationary phase respiration impairs persister formation in E. coli.* Nature Communications, 2015. **6**: p. 7983.

198. Carret, G., J.P. Flandrois, and J.R. Lobry, *Biphasic kinetics of bacterial killing by quinolones.* The Journal of Antimicrobial Chemotherapy, 1991. **27**(3): p. 319-327.

199. Keren, I., et al., *Persister cells and tolerance to antimicrobials.* FEMS Microbiology Letters, 2004. **230**(1): p. 13-18.

200. Allen, R. and B. Waclaw, *Antibiotic resistance: a physicist's view.* Physical Biology, 2016. **13**(4): p. 045001.

201. Newman, M.E.J., *Power laws, Pareto distributions and Zipf's law.* Contemporary physics, 2005. **46**(5): p. 323-351.

202. Baranyi, J., *Stochastic modelling of bacterial lag phase.* International Journal of Food Microbiology, 2002. **73**(2-3): p. 203-206.

203. Baranyi, J. and C. Pin, *Estimating bacterial growth parameters by means of detection times.* Applied and Environmental Microbiology, 1999. **65**(2): p. 732-736.

204. Şimşek, E. and M. Kim, *The emergence of metabolic heterogeneity and diverse growth responses in isogenic bacterial cells.* The ISME Journal, 2018. **12**(5): p. 1199-1209.

205. Levin-Reisman, I., et al., *Automated imaging with ScanLag reveals previously undetectable bacterial growth phenotypes.* Nature Methods, 2010. **7**(9): p. 737-739.

206. Kutalik, Z., et al., *Stochastic modelling of individual cell growth using flow chamber microscopy images.* International Journal of Food Microbiology, 2005. **105**(2): p. 177-190.

207. Francois, K., et al., *Modelling the individual cell lag phase: effect of temperature and pH on the individual cell lag distribution of Listeria monocytogenes.* International Journal of Food Microbiology, 2005. **100**(1-3): p. 41-53.

208. Maisonneuve, E. and K. Gerdes, *Molecular Mechanisms Underlying Bacterial Persisters.* Cell, 2014. **157**(3): p. 539-548.

209. Trastoy, R., et al., *Mechanisms of Bacterial Tolerance and Persistence in the Gastrointestinal and Respiratory Environments.* Clinical Microbiology Reviews, 2018. **31**(4): p. e00023-18.

210. Moyed, H.S. and K.P. Bertrand, *hipA, a newly recognized gene of Escherichia coli K-12 that affects frequency of persistence after inhibition of murein synthesis.* 1983. **155**(2): p. 768-775.

211. Dörr, T., M. Vulić, and K. Lewis, *Ciprofloxacin causes persister formation by inducing the TisB toxin in Escherichia coli.* PLoS Biology, 2010. **8**(2): p. e1000317.

212. Vázquez-Laslop, N., H. Lee, and A.A. Neyfakh, *Increased persistence in Escherichia coli caused by controlled expression of toxins or other unrelated proteins.* Journal of Bacteriology, 2006. **188**(10): p. 3494-3497.

213. Kim, Y. and T.K. Wood, *Toxins Hha and CspD and small RNA regulator Hfq are involved in persister cell formation through MqsR in Escherichia coli.* Biochemical and Biophysical Research Communications, 2010. **391**(1): p. 209-213.

214. Pu, Y., et al., *Enhanced efflux activity facilitates drug tolerance in dormant bacterial cells.* Molecular Cell, 2016. **62**(2): p. 284-294.

215. Li, Y. and Y. Zhang, *PhoU Is a Persistence Switch Involved in Persister Formation and Tolerance to Multiple Antibiotics and Stresses in Escherichia coli.* Antimicrobial Agents and Chemotherapy, 2007. **51**(6): p. 2092-2099.

216. Wu, N., et al., *Ranking of persister genes in the same Escherichia coli genetic background demonstrates varying importance of individual persister genes in tolerance to different antibiotics.* Frontiers in Microbiology, 2015. **6**(1003).

217. Dörr, T., K. Lewis, and M. Vuli, *SOS Response Induces Persistence to Fluoroquinolones in <italic>Escherichia coli</italic>.* PLoS Genet, 2009. **5**(12): p. e1000760.

218. Debbia, E.A., et al., *Antibiotic Persistence: The Role of Spontaneous DNA Repair Response.* 2001. **7**(4): p. 335-342.

219. Hansen, S., K. Lewis, and M. Vulić, *Role of global regulators and nucleotide metabolism in antibiotic tolerance in Escherichia coli.* Antimicrobial Agents and Chemotherapy, 2008. **52**(8): p. 2718-2726.

220. Miller, C., et al., *SOS response induction by beta-lactams and bacterial defense against antibiotic lethality.* Science, 2004. **305**(5690): p. 1629-1631.

221. Johnson, P.J. and B.R. Levin, *Pharmacodynamics, population dynamics, and the evolution of persistence in Staphylococcus aureus.* PLoS Genet, 2013. **9**(1): p. e1003123.

222. Ray, J.C.J., et al., *Cellular Growth Arrest and Persistence from Enzyme Saturation.* PLOS Computational Biology, 2016. **12**(3): p. e1004825.

223. Amato, S.M., et al., *The role of metabolism in bacterial persistence.* Frontiers in Microbiology, 2014. **5**.

224. Allison, K.R., M.P. Brynildsen, and J.J. Collins, *Heterogeneous bacterial persisters and engineering approaches to eliminate them.* Current Opinion in Microbiology, 2011. **14**(5): p. 593-598.

225. Defraine, V., M. Fauvart, and J. Michiels, *Fighting bacterial persistence: Current and emerging anti-persister strategies and therapeutics.* Drug Resistance Updates, 2018. **38**: p. 12-26.

226. Butler, M.T., Q. Wang, and R.M. Harshey, *Cell density and mobility protect swarming bacteria against antibiotics.* Proceedings of the National Academy of Sciences of the United States of America, 2010. **107**(8): p. 3776-3781.

227. Dang, H. and C.R. Lovell, *Microbial surface colonization and biofilm development in marine environments.* Microbiology and Molecular Biology Reviews, 2016. **80**(1): p. 91-138.

228. Kearns, D.B., *A field guide to bacterial swarming motility.* Nature Reviews. Microbiology, 2010. **8**(9): p. 634-644.

229. Rather, P.N., *Swarmer cell differentiation in Proteus mirabilis.* Environmental Microbiology, 2005. **7**(8): p. 1065-1073.

230. Klieneberger-Nobel, E., *Morphological appearances of various stages in B. proteus and coli.* The Journal of hygiene, 1947. **45**(4): p. 410-412.

231. Hoeniger, J.F.M., *Cellular changes accompanying the swarming of proteus mirabilis: i. observations of living cultures.* Canadian Journal of Microbiology, 1964. **10**(1): p. 1-9.

232. Czirók, A., M. Matsushita, and T. Vicsek, *Theory of periodic swarming of bacteria: application to Proteus mirabilis.* Physical Review. E, Statistical, Nonlinear, and Soft Matter Physics, 2001. **63**(3 Pt 1): p. 031915.

233. Hoeniger, J.F.M., *CELLULAR CHANGES ACCOMPANYING THE SWARMING OF PROTEUS MIRABILIS: II. OBSERVATIONS OF STAINED ORGANISMS.* Canadian Journal of Microbiology, 1966. **12**(1): p. 113-123.

234. Morgenstein, R.M., B. Szostek, and P.N. Rather, *Regulation of gene expression during swarmer cell differentiation in Proteus mirabilis.* FEMS Microbiology Reviews, 2010. **34**(5): p. 753-763.

235. Sturgill, G. and P.N. Rather, *Evidence that putrescine acts as an extracellular signal required for swarming in Proteus mirabilis.* Molecular Microbiology, 2004. **51**(2): p. 437-446.

236. Rauprich, O., et al., *Periodic phenomena in Proteus mirabilis swarm colony development.* Journal of Bacteriology, 1996. **178**(22): p. 6525-6538.

237. Itoh, H., et al., *Periodic Pattern Formation of Bacterial Colonies.* Journal of the Physical Society of Japan, 1999. **68**(4): p. 1436-1443.

238. Armbruster, C.E., S.A. Hodges, and H.L.T. Mobley, *Initiation of swarming motility by Proteus mirabilis occurs in response to specific cues present in urine and requires excess L-glutamine.* Journal of Bacteriology, 2013. **195**(6): p. 1305-1319.

239. Clemmer, K.M. and P.N. Rather, *Regulation of flhDC expression in Proteus mirabilis.* Research in Microbiology, 2007. **158**(3): p. 295-302.

240. Howery, K.E., et al., *Positive autoregulation of the flhDC operon in Proteus mirabilis.* Research in Microbiology, 2018. **169**: p. 199-204.

241. Howery, K.E., et al., *Regulation of the Min Cell Division Inhibition Complex by the Rcs Phosphorelay in Proteus mirabilis.* Journal of Bacteriology, 2015. **197**(15): p. 2499-2507.

242. Chilcott, G.S. and K.T. Hughes, *Coupling of Flagellar Gene Expression to Flagellar Assembly in Salmonella enterica Serovar Typhimurium andEscherichia coli*. 2000. **64**(4): p. 694-708.

243. Zhao, K., M. Liu, and R.R. Burgess, *Adaptation in bacterial flagellar and motility systems: from regulon members to 'foraging'-like behavior in E. coli.* Nucleic Acids Research, 2007. **35**(13): p. 4441-4452.

244. Claret, L. and C. Hughes, *Interaction of the Atypical Prokaryotic Transcription Activator FlhD2C2 with Early Promoters of the Flagellar Gene Hierarchy.* Journal of Molecular Biology, 2002. **321**(2): p. 185-199.

245. Claret, L. and C. Hughes, *Functions of the subunits in the FlhD2C2 transcriptional master regulator of bacterial flagellum biogenesis and swarming11Edited by I. B. Holland.* Journal of Molecular Biology, 2000. **303**(4): p. 467-478.

246. Liu, X. and P. Matsumura, *The FlhD/FlhC complex, a transcriptional activator of the Escherichia coli flagellar class II operons.* 1994. **176**(23): p. 7345-7351.

247. Furness, R.B., et al., *Negative feedback from a Proteus class II flagellum export defect to the flhDC master operon controlling cell division and flagellum assembly.* 1997. **179**(17): p. 5585-5588.

248. Belas, R. and R. Suvanasuthi, *The Ability of Proteus mirabilis To Sense Surfaces and Regulate Virulence Gene Expression Involves FliL, a Flagellar Basal Body Protein.* 2005. **187**(19): p. 6789-6803.

249. Esipov, S.E. and J.A. Shapiro, *Kinetic model of Proteus mirabilis swarm colony development.* Journal of Mathematical Biology, 1998. **36**(3): p. 249-268.

250. Ayati, B.P., *A comparison of the dynamics of the structured cell population in virtual and experimental Proteus mirabilis swarm colonies.* Applied Numerical Mathematics, 2009. **59**(3-4): p. 487-494.

251. Ayati, B.P., *A structured-population model of Proteus mirabilis swarm-colony development.* Journal of Mathematical Biology, 2006. **52**(1): p. 93-114.

252. Francez-Charlot, A., et al., *RcsCDB His-Asp phosphorelay system negatively regulates the flhDC operon in Escherichia coli.* Molecular Microbiology, 2003. **49**(3): p. 823-832.

253. Belas, R., R. Schneider, and M. Melch, *Characterization of Proteus mirabilis precocious swarming mutants: identification of rsbA, encoding a regulator of swarming behavior.* Journal of Bacteriology, 1998. **180**(23): p. 6126-6139.

254. Ferrières, L. and D.J. Clarke, *The RcsC sensor kinase is required for normal biofilm formation in Escherichia coli K-12 and controls the expression of a regulon in response to growth on a solid surface.* Molecular Microbiology, 2003. **50**(5): p. 1665-1682.

255. Kimkes, T.E.P. and M. Heinemann, *Reassessing the role of the Escherichia coli CpxAR system in sensing surface contact.* Plos One, 2018. **13**(11): p. e0207181.

256. Majdalani, N. and S. Gottesman, *THE RCS PHOSPHORELAY: A Complex Signal Transduction System.* 2005. **59**(1): p. 379-405.

257. Hughes, K.T., *Flagellum Length Control: How Long Is Long Enough?* Current Biology, 2017. **27**(11): p. R413-R415.

258. Berg, H.C., *Random Walks In Biology*. 1983: Princeton University Press.

259. Ariel, G., et al., *Swarming bacteria migrate by Lévy Walk.* Nature Communications, 2015. **6**: p. 8396.

260. Li, X., et al., *Repression of bacterial motility by a novel fimbrial gene product.* 2001. **20**(17): p. 4854-4862.

261. Kaniga, K., I. Delor, and G.R. Cornelis, *A wide-host-range suicide vector for improving reverse genetics in Gram-negative bacteria: inactivation of the blaA gene of Yersinia enterocolitica.* Gene, 1991. **109**(1): p. 137-141.

262. de Lorenzo, V., et al., *Mini-Tn5 transposon derivatives for insertion mutagenesis, promoter probing, and chromosomal insertion of cloned DNA in gram-negative eubacteria.* Journal of Bacteriology, 1990. **172**(11): p. 6568-6572.

263. Manoil, C. and J. Beckwith, *TnphoA: a transposon probe for protein export signals.* Proc Natl Acad Sci U S A, 1985. **82**(23): p. 8129-33.

264. González-Flecha, B. and B. Demple, *Metabolic Sources of Hydrogen Peroxide in Aerobically Growing Escherichia coli.* 1995. **270**(23): p. 13681-13687.

265. Imlay, J.A. and I. Fridovich, *Assay of metabolic superoxide production in Escherichia coli.* 1991. **266**(11): p. 6957-65.

266. Cabiscol, E., J. Tamarit, and J. Ros, *Oxidative stress in bacteria and protein damage by reactive oxygen species.* Int Microbiol, 2000. **3**(1): p. 3-8.

267. Solopova, A., et al., *Bet-hedging during bacterial diauxic shift.* 2014. **111**(20): p. 7427-7432.

268. van Heerden, J.H., et al., *Lost in Transition: Start-Up of Glycolysis Yields Subpopulations of Nongrowing Cells.* 2014. **343**(6174): p. 1245114.

269. Wearmouth, V.J., et al., *Scaling laws of ambush predator 'waiting' behaviour are tuned to a common ecology.* Proceedings. Biological Sciences / the Royal Society, 2014. **281**(1782): p. 20132997.

270. Tu, Y. and G. Grinstein, *How White Noise Generates Power-Law Switching in Bacterial Flagellar Motors.* Physical Review Letters, 2005. **94**(20): p. 208101.

271. Park, H., et al., *Noise Underlies Switching Behavior of the Bacterial Flagellum.* Biophysical Journal, 2011. **101**(10): p. 2336-2340.

272. Korobkova, E., et al., *From molecular noise to behavioural variability in a single bacterium.* Nature, 2004. **428**(6982): p. 574-578.

273. Rinaldo, A., et al., *Cross–scale ecological dynamics and microbial size spectra in marine ecosystems.* 2002. **269**(1504): p. 2051-2059.

274. Gibiansky, M.L., et al., *Earthquake-like dynamics in Myxococcus xanthus social motility.* 2013. **110**(6): p. 2330-2335.

275. Dutta, P. and P.M. Horn, *Low-frequency fluctuations in solids: $\frac{1}{f}$ noise.* Reviews of Modern Physics, 1981. **53**(3): p. 497-516.

276. Hausdorff, J.M. and C.K. Peng, *Multiscaled randomness: A possible source of 1/f noise in biology.* Physical Review E, 1996. **54**(2): p. 2154-2157.

277. Jones, R.M., et al., *The Infectious Dose ofCoxiella Burnetii (Q Fever).* Applied Biosafety, 2006. **11**(1): p. 32-41.

278. Jones, R.M., et al., *The Infectious Dose ofFrancisella Tularensis (Tularemia).* Applied Biosafety, 2005. **10**(4): p. 227-239.

279. DuPont, H.L., et al., *Inoculum Size in Shigellosis and Implications for Expected Mode of Transmission.* The Journal of Infectious Diseases, 1989. **159**(6): p. 1126-1128.

280. Hara-Kudo, Y. and K. Takatori, *Contamination level and ingestion dose of foodborne pathogens associated with infections.* Epidemiology and Infection, 2011. **139**(10): p. 1505-1510.

281. Drenkard, E. and F.M. Ausubel, *Pseudomonas biofilm formation and antibiotic resistance are linked to phenotypic variation.* Nature, 2002. **416**(6882): p. 740-743.

282. Graham, D.Y., et al., *Effect of treatment of Helicobacter pylori infection on the long-term recurrence of gastric or duodenal ulcer. A randomized, controlled study.* Annals of Internal Medicine, 1992. **116**(9): p. 705-708.

283. Gomez, J.E. and J.D. McKinney, *M. tuberculosis persistence, latency, and drug tolerance.* Tuberculosis, 2004. **84**(1-2): p. 29-44.

284. Sigal, A., et al., *Cell-to-cell spread of HIV permits ongoing replication despite antiretroviral therapy.* Nature, 2011. **477**: p. 95.

285. Sigal, A. and D. Baltimore, *As Good As It Gets? The Problem of HIV Persistence despite Antiretroviral Drugs.* Cell Host & Microbe, 2012. **12**(2): p. 132-138.

286. Buerger, S., et al., *Microbial scout hypothesis, stochastic exit from dormancy, and the nature of slow growers.* Applied and Environmental Microbiology, 2012. **78**(9): p. 3221-3228.

287. Sturm, A. and J. Dworkin, *Phenotypic Diversity as a Mechanism to Exit Cellular Dormancy.* Current Biology, 2015. **25**(17): p. 2272-2277.

288. Fredriksson, Å., et al., *Defense against Protein Carbonylation by DnaK/DnaJ and Proteases of the Heat Shock Regulon.* 2005. **187**(12): p. 4207-4213.

289. Murray, K., et al., *Challenges in the microbiological food safety of fresh produce: Limitations of post-harvest washing and the need for alternative interventions.* Food Quality and Safety, 2017. **1**(4): p. 289-301.

290. Ordax, M., et al., *Survival of Erwinia amylovora in mature apple fruit calyces through the viable but nonculturable (VBNC) state.* Journal of Applied Microbiology, 2009. **107**(1): p. 106-116.